Diss. ETH No. 27066

Biomechanical compatibility of electrospun scaffolds for intervertebral disc repair

A thesis submitted to attain the degree of
DOCTOR OF SCIENCES of ETH ZURICH
(Dr. sc. ETH Zurich)
presented by

Dmitriy Alexeev

MSc, ETH Zurich

born on 10.02.1990
citizen of Latvia
accepted on the recommendation of

Prof. Dr. Stephen J. Ferguson

Dr. habil. Sibylle Grad

Dr. Alexander E. Ehret

2020

Acknowledgements

The work performed in the last 5 years and presented in this thesis could not have been possible without support and major contribution from the following people.

Firstly, I would like to express my sincere gratitude to Prof. Stephen J. Ferguson for giving me the opportunity to work in his group on this project, and his continued support throughout the project. I very much appreciated the balance he achieved with allowing me to make my own choices while providing advice and support at crucial points.

Furthermore, I would also like to express my gratitude to my colleagues and friends at the Eth Zurich and AO Foundation, who supported me both professionally and as friends throughout this project. I would like to thank:

- Prof. Edoardo Mazza and Alexander Ehret for invaluable scientific discussion and guidance during the project.
- Sybylle Grad and Zhen Li at AO Foundation for their guidance and willingness to help. As well as Shangbin Cui for his invaluable help, and Mauro Bluvol and Nora Goudsouzian for their technical support.
- Peter Schwilch for his technical support in the implementation of my experimental setups. The scientific centre for optical and electron microscopy (ScopeM) and especially Karsten Kunze, Joachim Hehl and Justine Kusch for their guidance and support in SEM imaging and microscopy.
- And the students, that helped me immensely with many aspects of the project, namely: Adam Korczak, Andrew Angehrn, Aurelia Bucciarelli, Kathrin Huebscher, Melanie Tschopp, Patrick Sequiera, Pascal Moor and Rea Fonjallaz.
- Alexander Ehret and Sibylle Grad for serving on the examination committee.

Finally, yet importantly, I would like to thank the Swiss National Science Foundation, ETH Zurich and AO Foundation for funding the research presented in this thesis.

Summary

Intervertebral disc (IVD) herniation is major cause of lower back pain, which in turn is one of the most frequent health conditions in the world and carries a large financial cost to the national healthcare systems and individuals as well quality of life burden. The role of the IVD in the spinal column is primarily mechanical. It provides flexibility and load bearing capabilities in the spine. It consists of circumferential stiff outer layers known as annulus fibrosus (AF) which together with the endplates positioned in the caudal-cranial direction contain the inner soft hydrogel known as nucleus pulposus (NP). The injury to the IVD can occur through mechanical damage in an extreme event or long-term exposure, or degenerative pathways due to systemic conditions. In the event of the mainly mechanical failure of the IVD the organ loses its integrity through the rupture of the endplates or the AF. This is usually followed by the bulging of the NP, which can lead to a degenerative cascade and nerve impingement. Both conditions are associated with significant pain symptoms. Current treatment options are either resort to symptom management and natural regenerative processes, or intrusive surgical procedures that have poor long-term outcomes, with many cases of re-herniation and further degeneration of the damage area. Therefore, a need for a biocompatible repair strategy for the rupture of the AF exists, to provide an alternative which would have good long-term outcomes by accelerating natural regenerative processes and decreasing re-herniation probability in the short term.

Electrospun poly(ε-caprolactone) (PCL) is widely used to provide critical mechanical support in tissue engineering and regenerative medicine applications and is FDA approved for clinical in vivo use. This work investigates the feasibility of using electrospun PCL in combination with biocompatible adhesive to provide mechanical

support at the AF injury site and serve as a template for the natural repair processes and proposes a possible design for such repair tested on an ex vivo model.

In the first part of this thesis, mechanical and material characterization of the electrospun PCL membranes was performed. While there is a large body of literature on electrospinning various polymers including PCL, and characterization of their mechanical and material properties. Several gaps in the available knowledge were identified specifically in the scope of biomedical applications that require cyclic loading and large strains. In the first study, a new method for performing mechanical tests on single electrospun PCL fibres was developed and applied to assess the mechanical behaviour of single fibres in conditions relevant for the application. Single fibres with a wide range of diameters from 0.4 to 6.0 µm were electrospun. Cyclic mechanical tests were used to establish a bimodal linear relationship between fibre diameter and Young’s modulus with a sharp increase in modulus below 0.9 µm. In addition, it was found that polycaprolactone exhibits a significant viscoelastic response, the range of which can be improved through preconditioning. These findings were important to establish the feasibility of using PCL as the underlying material for the electrospun membranes and define its limitations and potential. In the second study, the membranes produced from fibres characterized in the first study were exposed to in vitro conditions at 37 °C in DMEM or dry for up to 6 months. The mechanical properties and changes in the material were investigated at several timepoints. The mechanical testing was once again designed with application in mind, with strains up to 150 % and multiple loading cycles. This study allowed to test the change in tensile modulus, resilience and the elastically recoverable range of the electrospun membranes after exposure to in vitro conditions. Furthermore, the resilience and elastically recoverable range were contextualized with respect to the strain environment found in the native outer layers of AF based on the finite element model and the available literature. The modulus of the tested membranes was at the lower range of the values found in literature, while the elastically recoverable strain after preconditioning for all membrane types lies within the desired strain range for this application.

In the second phase of the project, based on the promising results from the assessment of electrospun PCL membranes, the full repair strategy was defined and tested on a synthetic in vitro model and exe vivo model based on bovine tail IVDs. Initially to attempt to overcome the limitations of the ex vivo model such as cost and labour-intensive preparation procedures, a synthetic model based on defining synthetic analogues for the AF and NP was attempted. While some aspects of the mechanical behaviour of the native IVD could be approximated, the model was not deemed significantly similar to be of scientific value. However, surface strain measurements performed on the scaffolds subjected to strains similar to those found in vivo using the synthetic in vitro model showed promising resilience results and provided additional selection criteria based on the membrane geometry and stiffness. In the final stage of the project the mechanical response of the commonly used annulus fibrosus puncture injury model of the IVD and a newly proposed AF failure at the endplate junction on ex vivo bovine IVDs. Biocompatibility and mechanics of PCL scaffold and fibrin-genipin (FibGen) adhesive was tested on the delamination model. The study allowed to identify a trend in the difference between the intact and delaminated state, while no such trend was present for the puncture model. The main goals of the repair strategy to create a tight seal on the damage area and restore mechanical properties, while showing little cytotoxicity, were achieved.

In conclusion, the development of biocompatible repair strategy for the IVD herniation is fundamental to achieving consistent and positive long-term treatment outcomes. There is a clear gap in the current medical approaches that there is significant motivation to fill. This is evidenced by the large volume of possible solutions that are being proposed and investigated in literature. This thesis provides a look into the feasibility of using electrospun PCL membranes for this application. While this material comes with its limitations, its biocompatibility and overall mechanical competence are promising. The complete repair strategy proposed in this work utilising FibGen hydrogel glue in combination with PCL membrane showed particularly good mechanical restoration results on the ex vivo model. With further optimization and development of the application process for surgical procedures the author believes that the relative simplicity, low cost and robustness of the approach will provide a valuable basis for in vivo applications.

Résumé

L'hernie discale intervertébrale (IVD) est une cause majeure de lombalgie, qui est à son tour l'un des problèmes de santé les plus fréquents dans le monde et entraîne un coût financier important pour les systèmes de santé nationaux et les individus, ainsi qu'un fardeau pour la qualité de vie. Le rôle des DIV dans la colonne vertébrale est essentiellement mécanique. Il offre une flexibilité et des capacités de charge dans la colonne vertébrale. Il se compose de couches externes rigides circonférentielles connues sous le nom d'anneau fibreux (AF) qui, avec les plaques terminales positionnées dans la direction caudale-crânienne, contiennent l'hydrogel souple interne connu sous le nom de noyau pulpeux (NP). La lésion du IVD peut être due à un dommage mécanique lors d'un événement extrême ou d'une exposition à long terme, ou à des voies dégénératives dues à des conditions systémiques. En cas de défaillance principalement mécanique du IVD Cette rupture est généralement suivie d'un bombement de la NP, qui peut entraîner une cascade dégénérative et un conflit nerveux. Ces deux conditions sont associées à des symptômes de douleur importants. Les options de traitement actuelles sont soit le recours à la gestion des symptômes et aux processus naturels de régénération, soit une intervention chirurgicale intrusive qui a de mauvais résultats à long terme, avec de nombreux cas de ré-herniation et de dégénérescence supplémentaire de la zone endommagée. Il est donc nécessaire de mettre en place une stratégie de réparation biocompatible pour la rupture de la AF, afin d'offrir une alternative qui aurait de bons résultats à long terme en accélérant les processus de régénération naturelle et en diminuant la probabilité de ré-herniation à court terme.

Le poly(ε-caprolactone) électrofilé (PCL) est largement utilisé pour fournir un support mécanique critique dans les applications d'ingénierie tissulaire et de médecine

régénérative et est approuvé par la FDA pour une utilisation clinique in vivo. Ce travail étudie la faisabilité de l'utilisation du PCL électrofilé en combinaison avec un adhésif biocompatible pour fournir un support mécanique sur le site de la lésion de la AF et servir de modèle pour les processus naturels de réparation, et propose une conception possible pour une telle réparation testée sur un modèle ex vivo.

Dans la première partie de cette thèse, une caractérisation mécanique et matérielle des membranes PCL électrofilées a été réalisée. Bien qu'il existe un grand nombre d'ouvrages sur l'électrofiltration de divers polymères, dont les PCL, et la caractérisation de leurs propriétés mécaniques et matérielles. Plusieurs lacunes dans les connaissances disponibles ont été identifiées, en particulier dans le domaine des applications biomédicales qui nécessitent une charge cyclique et des contraintes importantes. Dans la première étude, une nouvelle méthode pour effectuer des tests mécaniques sur des fibres PCL électrofilées simples a été développée et appliquée pour évaluer le comportement mécanique des fibres simples dans des conditions pertinentes pour l'application. Des fibres simples avec une large gamme de diamètres de 0,4 à 6,0 µm ont été filées par électrolyse. Des tests mécaniques cycliques ont été utilisés pour établir une relation linéaire bimodale entre le diamètre de la fibre et le module de Young avec une forte augmentation du module en dessous de 0,9 µm. En outre, il a été constaté que le polycaprolactone présente une réponse viscoélastique significative, dont la plage peut être améliorée par un préconditionnement. Ces résultats ont été importants pour établir la faisabilité de l'utilisation du PCL comme matériau sous-jacent des membranes électrofilées et pour définir ses limites et son potentiel. Dans la deuxième étude, les membranes produites à partir des fibres caractérisées dans la première étude ont été exposées à des conditions in vitro à 37 °C dans du DMEM ou à sec pendant une période allant jusqu'à 6 mois. Les propriétés mécaniques et les changements dans le matériau ont été étudiés à plusieurs moments.

Les essais mécaniques ont de nouveau été conçus en fonction de l'application, avec des contraintes allant jusqu'à 150 % et des cycles de charge multiples. Cette étude a permis de tester la modification du module de traction, de la résilience et de la plage de récupération élastique des membranes électrofilées après exposition à des conditions in vitro. De plus, la résilience et la plage de récupération élastique ont été mises en contexte par rapport à l'environnement de déformation des couches externes natives de l'AF, sur la base du modèle d'éléments finis et de la littérature disponible. Le module des membranes testées se situait dans la plage inférieure des valeurs trouvées dans la littérature, tandis que la déformation élastiquement récupérable après préconditionnement pour tous les types de membranes se situe dans la plage de déformation souhaitée pour cette application.

Dans la deuxième phase du projet, sur la base des résultats prometteurs de l'évaluation des membranes PCL électrofilées, la stratégie de réparation complète a été définie et testée sur un modèle synthétique in vitro et un modèle exe vivo basé sur des IVD de queue de bovins. Au départ, pour tenter de surmonter les limites du modèle ex vivo telles que le coût et les procédures de préparation à forte intensité de main-d'œuvre, un modèle synthétique basé sur la définition d'analogues synthétiques pour la AF et la NP a été tenté. Bien que certains aspects du comportement mécanique des IVD indigènes aient pu être approximés, le modèle n'a pas été jugé significativement similaire pour avoir une valeur scientifique. Cependant, les mesures de déformation de surface effectuées sur les échafaudages soumis à des déformations similaires à celles trouvées in vivo en utilisant le modèle synthétique in vitro ont montré des résultats prometteurs en matière de résilience et ont fourni des critères de sélection supplémentaires basés sur la géométrie et la rigidité de la membrane. Dans la phase finale du projet, la réponse mécanique du modèle de lésion par perforation de l'anneau fibreux communément utilisé pour les IVD et une nouvelle proposition de défaillance de la AF à la jonction des plaques terminales sur les IVD bovins ex vivo. La biocompatibilité et la mécanique de l'échafaudage PCL et de l'adhésif fibrinogénipin (FibGen) ont été testées sur le modèle de délamination. L'étude a permis d'identifier une tendance dans la différence entre l'état intact et l'état délaminé, alors qu'aucune tendance de ce type n'était présente pour le modèle de ponction. Les principaux objectifs de la stratégie de réparation visant à créer un joint étanche sur la zone endommagée et à restaurer les propriétés mécaniques, tout en présentant une cytotoxicité minimale, ont été atteints.

En conclusion, le développement d'une stratégie de réparation biocompatible pour la hernie IVD est fondamental pour obtenir des résultats de traitement cohérents et positifs à long terme. Il existe une lacune évidente dans les approches médicales actuelles qu'il est très motivant de combler. Cela est démontré par le grand nombre de solutions possibles qui sont proposées et étudiées dans la littérature. Cette thèse examine la faisabilité de l'utilisation de membranes PCL électrofilées pour cette application. Bien que ce matériau présente des limites, sa biocompatibilité et sa compétence mécanique globale sont prometteuses. La stratégie de réparation complète proposée dans ce travail, utilisant la colle hydrogel FibGen en combinaison avec la membrane PCL, a montré des résultats de restauration mécanique particulièrement bons sur le modèle ex vivo. Avec une optimisation et un développement supplémentaire du processus d'application pour les procédures chirurgicales, les auteurs pensent que la simplicité relative, le faible coût et la robustesse de l'approche fourniront une base précieuse pour les applications in vivo.

Table of Contents

Chapter 1: Introduction

1.1: Thesis motivation

Lower back pain (LBP) is a major burden on health care systems across the world[1,2]. Medical, social and productivity costs of LBP cumulatively contribute to the immense importance of the issue. Additionally, LBP was thought to be prevalent in adults and elderly, however recent studies suggest that the disorder affects all ages with similar frequency[3]. The causes of LBP are varied and unfortunately, there is no consensus on a clear definition, which specific conditions are attributed to LBP. As a subgroup of the overall acute lower back pain can be self-limiting or lead to a chronic condition. In particular, most frequently people report strenuous physical activity involving significant rotations and bending of the spine as well as static posture and vibrations[4]. This behaviour can often lead to injury to the intervertebral disc (IVD). In fact, herniation of the IVD is one of the leading causes of LBP. IVD herniation is characterized as a localized displacement of disc material beyond the limits of the IVD space[5]. The protrusion can occur in two directions: circumferentially and along the spinal axes[6]. This thesis focuses on the circumferential failure as though its necessarily outward protrusion it allows for novel minimally invasive repair strategies. Circumferential protrusion by definition is associated with mechanical failure of the annulus fibrosus (AF), which is the fibrous outer layer of the IVD. Fissures and tears in this outer layer as a result of mechanical damage or degenerative processes leads to expulsion of the inner IVD material, which in turn can cause severe pain by impinging on the spinal nerve, inflammatory processes and tissue and nerve ingrowth into the damaged area[7–9]. IVD is an avascular organ with poor cellularization in the outer layers[10], where much of tissue restoration is required. Therefore, the intrinsic ability of the IVDs to restore morphology and recover function post herniation is very limited. This highlights a need for an effective treatment strategy to restore the mechanical function of the AF and contain the expulsion of IVD material.

Clinically available solutions suffer from intrusive surgical procedures that aim to replace the damaged IVD and do not provide a regenerative approach. Even then, the available implants are unable to replicate native mechanical properties of the IVDs and as the result lead to further degeneration after extended post implantation periods. Consequently, there is a need for a regenerative approach, especially in younger population who are especially affected by limited mobility, further degeneration and repeated surgical procedures.

A synthetic construct as a regenerative approach to hernia repair is fitting considering the characteristics of the tissue. Such a construct would have to fulfil broad biocompatibility criteria such as lack of toxicity, biodegradability and effective functionality. The approach proposed in this thesis utilizes a patch like composite consisting of an electrospun matrix and adhesive. The objective of the patch is to be applied on the outer layers of the herniated IVD and provide mechanical support and a tight seal on the damaged area, with the goal of restoring original biomechanical properties of the organ.

To be able to provide an effective design, individual components and native tissue properties need to be thoroughly characterized.

The aim of the presented thesis is characterization of the possibilities and performance of electrospun membranes in the scope of tissue engineering and regenerative medicine and specifically IVD herniation repair. Furthermore, assessment of the feasibility and performance of the application of the electrospun scaffold in conjunction with a biocompatible glue as repair strategy for an IVD hernia. To achieve these objectives, firstly the mechanical competence and performance of the electrospun membranes made of poly(ε-caprolactone) (PCL) was investigated to allow intelligent design of the scaffolds for the use as a repair. Following the general mechanical characterization, a variety of specific methods for applying the scaffolds on the injury and well the biomechanics of the injury were investigated in a series of mini studies. Finally, an optimized repair strategy was successfully applied to an ex vivo IVD herniation model.

1.2: Investigation of electrospun scaffold production and properties for in vivo applications

While electrospinning is well established method for manufacturing scaffolds for tissue engineering and regenerative medicine, much of the previous work focuses on the biocompatibility of the materials. The investigation into the mechanical loading conditions, mechanical properties, and mechanical resilience of the scaffolds required for a successful biomedical implant is somewhat limited. Especially because the mechanical response differs widely between different polymers and electrospinning setups used. PCL polymer was chosen early in the project as a base material, because of pre-existing experience with the polymer, and because its biocompatible properties are well documented and established clinically. Therefore, the first part of the project was designed to analyse the competence of electrospun networks in the context of tissue engineering and regenerative medicine application, where both microscopic and macroscopic properties were investigated. To investigate the microscopic properties the electrospun PCL fibres, a new testing method was designed to tests fibres to strains similar to those found in vivo in well controlled environment and high precision. The macroscopic properties were also investigated on scaffolds suitable for tissue engineering in a long-term study that assessed the both the mechanical response of the scaffolds in biomechanically relevant loading conditions and the evolution of the mechanics when exposed to in vitro environment.

1.3: In vitro validation of the IVD hernia repair strategy and repair strategy optimization

Once a basic understanding of the design criteria and the electrospinning process was achieved, the repair strategy needed to be optimized and the injury mechanics and morphology investigated. An in vitro model was created based on synthetic materials. High performance silicone was used as an AF analogue and gelatine gel was used for NP. Using this model, the performance of various injury types and repair strategies was investigated. In addition, to optimize the repair application procedure and understand the design space, a testing basic testing setup for an ex vivo IVD model was designed and implemented. The application process and repair strategy were optimized.

1.4: Ex vivo validation of the IVD hernia repair strategy

In the final stage the experience obtained in the previous stages was applied to defining the final a repair strategy and testing its performance on an ex vivo IVD model.

1.5: Thesis outline

This thesis is structured in seven chapters.

Chapter 1 Provides the thesis motivation, the specific aims as well as the thesis outline.

Chapter 2 Provides the thesis background and clinical relevance. Basic information on electrospinning in the scope of regenerative medicine and tissue engineering with a focus on poly(ε-caprolactone) is summarized. The anatomy of the IVD with a focus on mechanical properties of the constituting elements as well biomechanical environment, IVD herniation and pathology of the injury is described. In addition, and overview of current state of the art repair strategies for herniated IVDs is provided.

Chapter 3 An investigation into at the mechanical performance of electrospun PCL fibres at a microscopic level. The new method was designed for testing these fibres to reliably establish mechanical properties on the microscopic scale. Fibres with a wide range of diameters relevant for biomechanical applications were produced and tested. The new testing procedure allowed to test the samples at high strains and a cyclic manner, both key parameters for biomedical environments. The relationship between fibre diameter and mechanical properties was established.

Chapter 4 A characterization of mechanical response of electrospun PCL membranes over an extended period, while exposed to in vitro like environment. The electrospun membranes made of fibres developed in Chapter 3 underwent a biomechanically relevant testing procedure after exposure to cell culture medium at 37°C after a period of up to 6 months. The complex mechanical response of the membranes was described and contextualized in the scope of the IVD repair.

Chapter 5 In this chapter the in vitro model used to optimise the repair procedure and strategy in an efficient and low-cost manner is described. In addition, the preliminary work done on a bovine IVD ex vivo model to identify strategies and further optimise the repair procedure are summarized.

Chapter 6 This chapter addresses the intended application of the repair strategy including the electrospun PCL scaffold and biodegradable FibGen glue on the ex vivo bovine IVD model. The repair as well as two different injury models undergo long term biomechanical and biological evaluation in a bioreactor. The outcomes were evaluated to inform the feasibility of the procedure for in vivo applications and the mechanical efficacy of the repair. The results showed a promising restoration of the mechanical properties as well as biocompatibility.

Chapter 7 This chapter summarizes and discusses the overall result of the studies described in the previous chapters. It provides an overall conclusion of the findings presented in this thesis. It points out the limitations of the work as well as its contribution to the research field and potential future directions.

Chapter 2: Background

2.1: Anatomy of spine and intervertebral disc

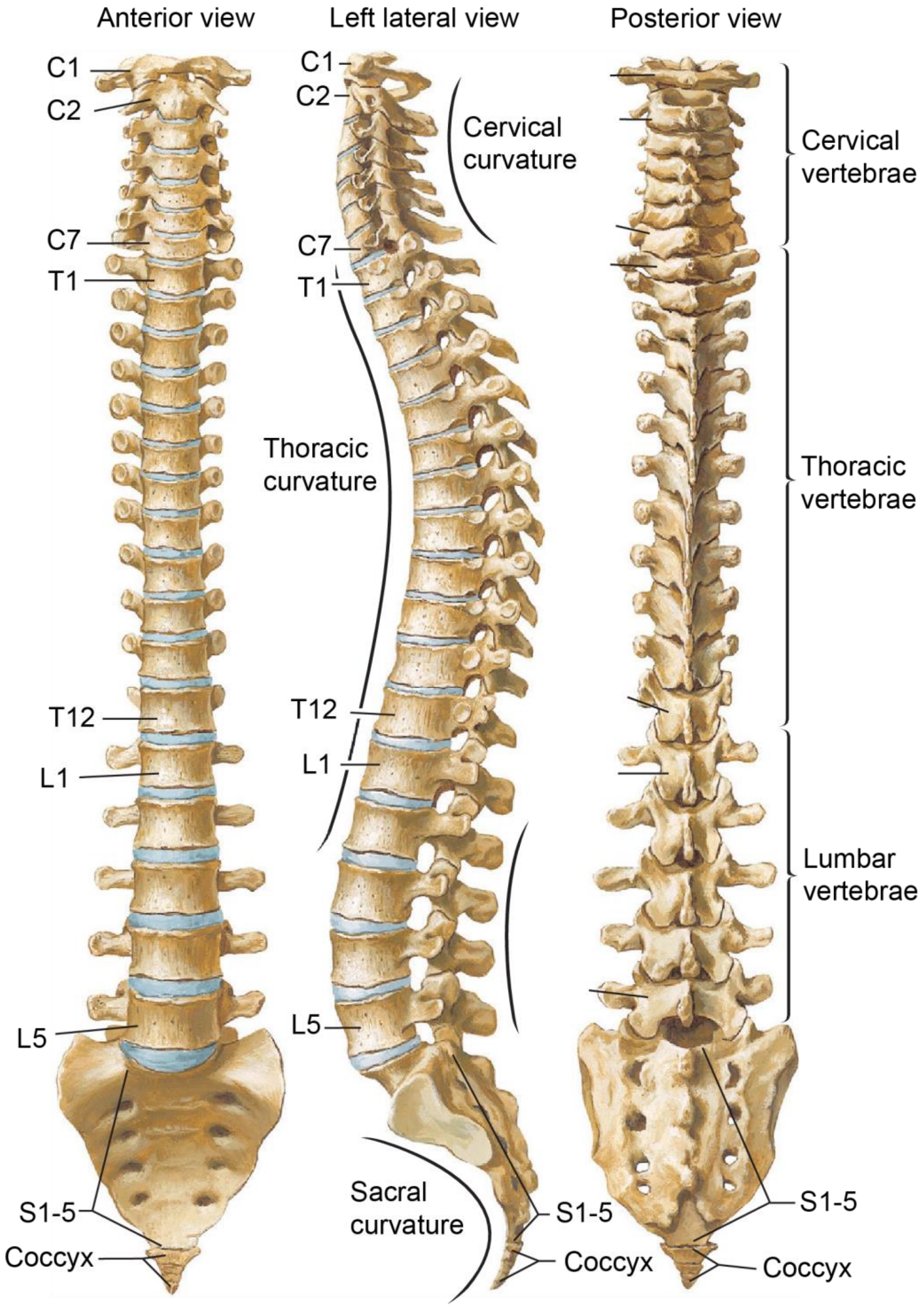

Figure 2-1: The vertebral column consists of alternating bony vertebra and fibrocartilaginous intervertebral discs. There are 33 vertebrae. All vertebrae are similar but different.

Netter illustration used with permission of Elsevier Inc. All rights reserved. www.netterimages.com

To clearly understand the disease and disorders of the spine a basic understanding of spine anatomy is crucial.

2.1.1: Vertebral column

In brief, human vertebral column is formed from 7 cervical, 12 thoracic, 5 lumbar, and 5 fused sacral vertebrae, along with 5 coccygeal bones depicted in Figure 2-1. The cervical, thoracic, and lumbar vertebrae are similar in structure except for the first (atlas) and second (axis) cervical vertebrae. Each “standard” vertebra is composed of a body, two pedicles, two lamina, four articular facets, and a spinous process. In the posterior of the column a channel through the vertebra and vertebra foramen is occupied by the spinal nerve, blood vessels and other nerve bundles that reach outside the spine to the surrounding organs. The vertebral column achieves its mobility through cartilaginous tissues between the vertebra known as intervertebral disc, as well as from the facet joint that provides minor compressive support but is mainly used to stabilise the spine in torsion and flexion.

The mechanical requirements on the spinal column of upright walking humans are extremely stringent. The column must possess the required stiffness and strength to support the trunk and the extremities of the human body, protect the spinal cord and other nerve bundles that are weave thought he column, and provide resilient anchorage for the muscles. These requirements are in contrast with the need for a flexible vertebral column, that would allow for the range of movement associated with normal functioning of a human being. In an engineering sense, designing such as structure puts these two requirements in opposition and compromise, which means that there is very little room for excess strength in any of the design criteria. This consideration explains why mechanical injuries to the spine are so common in human population. In addition, compromising significantly in one of the design criteria such as flexibility or stiffness leads to a degenerative cascade in the spinal column and even surrounding organs, as well as quality of life. This means that when addressing the damage to the spinal column or any degenerative process the treatment has to aim to restore all of the original mechanical and biological properties if the benefits of the treatment are to be sustained in the long term.

2.1.2: Intervertebral disc

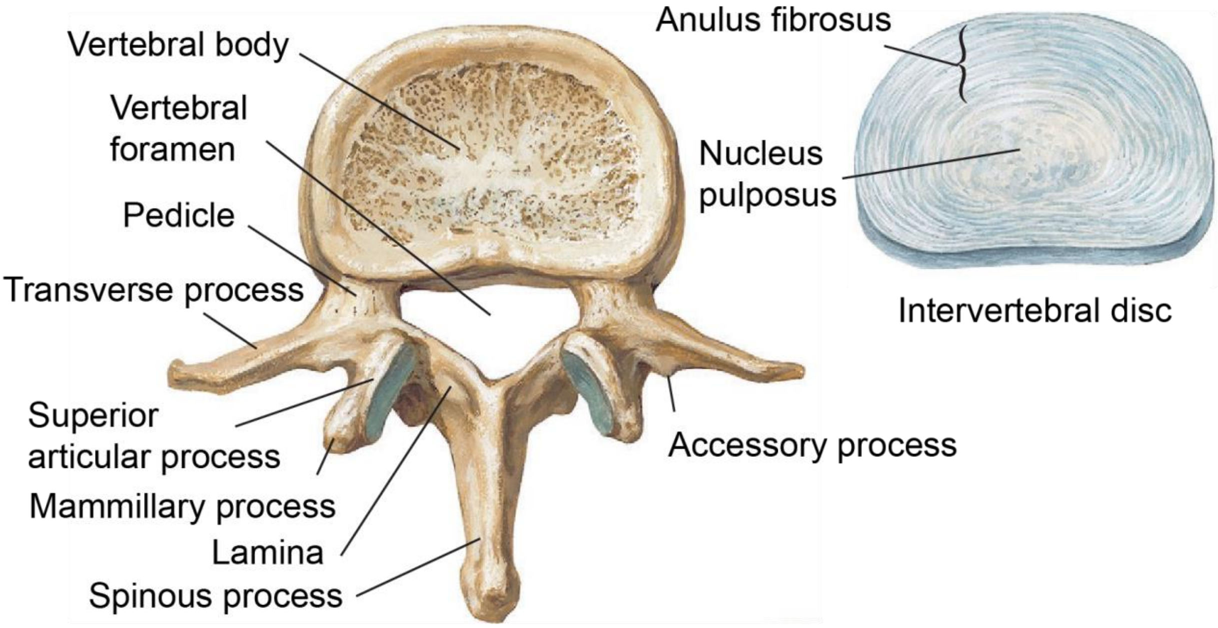

Figure 2-2: Between the adjacent vertebra the fibrocartilaginous vertebral discs are situated. The intervertebral disc consists of fibrous outer layer (annulus fibrosus) and inner gel like nucleus pulposus.

Netter illustration used with permission of Elsevier Inc. All rights reserved. www.netterimages.com

The intervertebral disc (IVD) is the main load bearing joint in the vertebral column positioned between the vertebral and consisting of fibrocartilage shown in Figure 2-2. The flexibility of the IVD allows for bending and rotation in the spine [11,12], as well as shock absorption and load distribution [13]. Each motion segment is comprised of two bony and rigid vertebra and a flexible, relatively compliant IVD. The IVD itself consists of inner hydrogel like core known as nucleus pulposus (NP) the outer fibrous layers encircling the NP called annulus fibrosus (AF). The cylindrical tissue structure of the NP and AF is capped with two cartilaginous endplates (EPs) that rest on the bony vertebra. The outer layers of AF are connected directly to the vertebra around the endplates.

The NP has a high-water content compared the other tissues in the motion segment. The ECM consists of primarily proteoglycans and a smaller proportion of the collagen II fibres, as well as other non-loadbearing proteins [14]. The primary role of proteoglycans is to bind the water in the NP and create hydrostatic pressure in the tissue. The collagen II fibres provide tensile cohesiveness to the tissue and a connection to the surrounding tissues [15–17]. Mechanically the purpose of the NP is to provide a largely incompressible volume within the IVD, which is contained by the AF. The incompressibility of NP is however time dependant, and the water can be squeezed at prolonged high loads. The resistance of NP to the squeezing out of water is dependent on the integrity of the organ, and biochemical composition of the ECM which affects permeability and hydrostatic pressure of the tissue.

The AF is the load bearing tissue in the IVD that works in tension unlike the NP. Therefore, unlike the NP is mainly consists of collagen I fibres that are strong in tension. AF water content is much lower than the NP and it contains much more collagen and less proteoglycans [14,15,18–20]. Additionally collagen II is present and plays a role in binding ECM components [21,22]. The specific arrangement of the collagen fibres in the AF tissue allows for high resilience and strength in the specific loading conditions that the tissue undergoes during daily activity. The collagen fibres are arranged into concentric lamellae from 0.05 to 0.5 mm thick[22–24]. The orientation of the fibres in the lamellae alternates in smaller bundle at 25° to 45° in the transverse plane [23–27]. Between the lamellae there is a more disorganised layer with high elastin content that provides resilience to the tissue and allows inter lamellar shear stresses to be accommodated [10,20,28–32]. The organisation of the lamellae as well as the ratio of collagen to proteoglycan decreases from the surface of the AF towards the NP and the water content increases [33], thus providing a gradual change to the NP and a strong interface with well distributed stresses.

2.2: Intervertebral disc herniation (IDH) and degenerative disc disease (DDD)

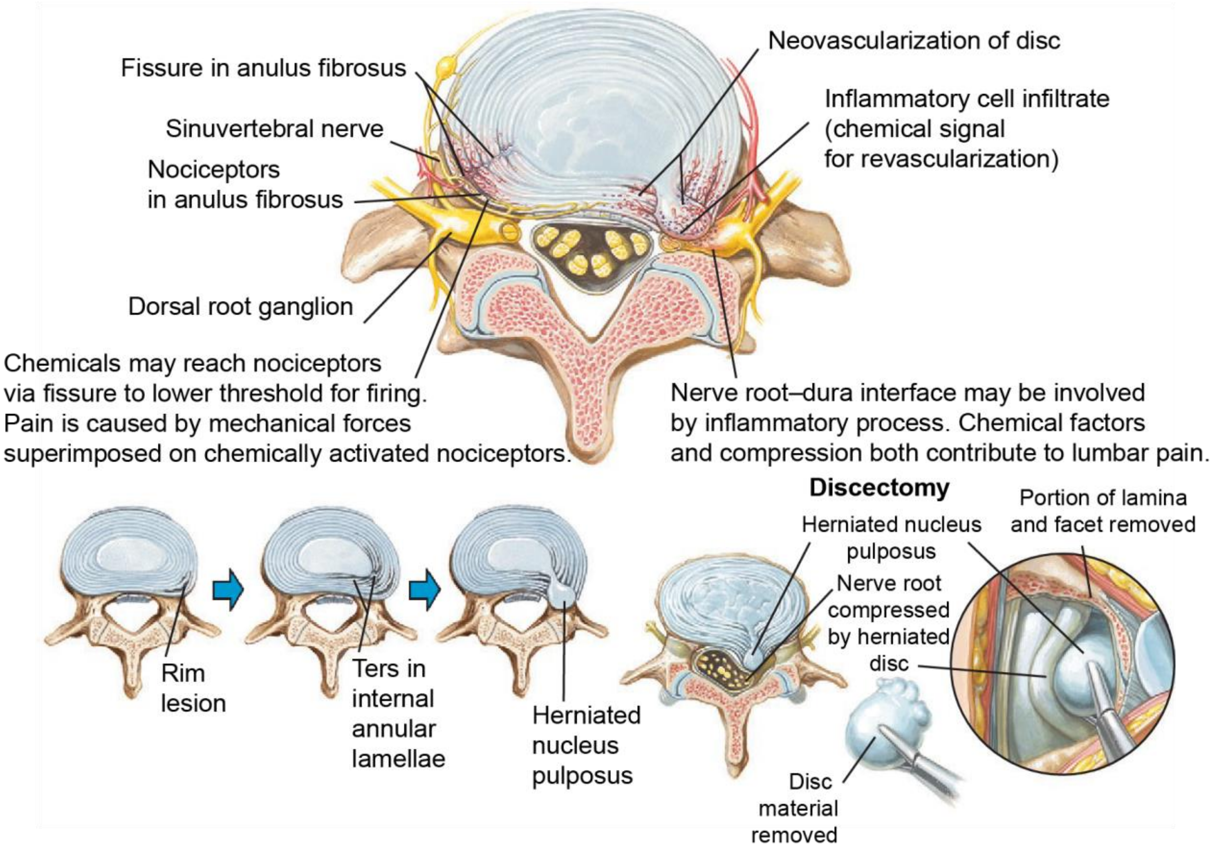

Figure 2-3: An example of intervertebral lumbar disc herniation. The pain associated with herniation is due to the inflammatory processes, nerve compression and cytokine release into nucleus pulposus and surrounding tissue.

Netter illustration used with permission of Elsevier Inc. All rights reserved. www.netterimages.com

2.2.1: Clinical relevance

Approximately 20 to 80 % of the people suffer from back pain, of which 7 to 8 % develop chromic pain symptoms[34]. The leading cause of back pain is compression and inflammation of the nerves in the cervical or lumbosacral region. The compression of the nerve can occur due to IVD herniation as a result of IVD degeneration[13,35,36]. There are many risk factors associated with IVD degeneration such as lifestyle, employment conditions, genetics and ageing [37–40]. The financial and social impact of IVD degeneration through the induction of back pain symptoms and limited mobility, which in turn lead to reduced quality of life, are significant.

2.2.2: Pathology

The intervertebral disc is primarily a load bearing organ in the body. Therefore, the pathology of the disc is often defined in terms of its mechanical competence. The end stage mechanical failure of the IVD is known as intervertebral disc herniation (IDH) shown in Figure 2-3. In case of IDH the NP is no longer contained by the EP or AF, therefore the basic loop of building pressure in the NP during compression which is balanced by the tension in the AF is disturbed leading to the collapse of the IVD in short period. The result of the collapse can be severe reduction in mobility, pain, and degeneration of the surrounding tissues. The causes for IDH are either mechanical damage to the IVD due to extreme loads, degenerative pathology that leads to degradation of the IVD tissue which then fail or both.

Overloading of the IVD either due to continued occupational hazards and lifestyle or an accident can lead to rupture of the AF and herniation[41,42]. This type of injury is particularly relevant for young individuals. The group that leads a sedentary lifestyle is particularly at risk as static loading has a higher injury chance then dynamic overloading [43].

The degeneration of the disc tissue is most commonly the consequence of aging, where the changes in the tissue begin to occur starting approximately in the 2nd decade of life [44]. The changes that occur with age originate in the NP and are associated with the reduction of water content of the NP though decrease in the collagen II fraction and increase in collagen I fraction[14,45–51]. As collagen II is responsible for binding ECM components such as proteoglycans, and those in turn are required for water binding properties of the NP. The changes in systaltic pressure led to alterations in the viscoelastic response of the NP and how the pressure builds when compressive loads are applied. Additional changes, such as increase of collagen I content and overall degradation of the ECM also contribute to an altered mechanical response of the NP and inner AF[52,53]. Due to these changes additional loads are transferred to the AF as well as the facet joint. In the AF this leads to deterioration and development of fissures. Coalescence of the fissures eventually leads to the failure of the AF. Additional stresses are also transferred to the vertebra, which can lead to microfractures.

2.3: Clinical indication and treatment of intervertebral disc herniation

Available treatments can be subdivided firstly into non-surgical approaches and surgical intervention. The non-surgical approaches include pain management strategies through drugs and lifestyle modification plans such as physiotherapy and occupational changes. The surgical treatments vary in their invasiveness and the degree to which the native function of the IVD is reduced.

There is no consensus whether invasive surgical techniques are more effective than non-invasive methods.

2.3.1: Conservative treatment

Conservative treatment of IVD herniation consists of symptom management in the form of painkillers and anti-inflammatory agents as well as immobilization for up to 2 weeks with further support in severe cases. These measures are applied in the hope that the injury will repair itself when the inflammation subsides. Steroidal anti-inflammatory injections at the damaged site are also sometimes used. In healthy adolescents, where the return to normal function is very important, the success of conservative treatment is between 25 to 50 %[54,55]. Some researchers have observed no significant differences between surgical and conservative treatment after a 6 year follow up[55], however the consensus is that the surgical outcomes in young, otherwise healthy patients are better than just conservative treatments[54,56–60]. None the less, conservative treatments are often prescribed first, in case improvement is observed as surgical treatments carry secondary risks associated with invasive surgical procedures.

2.3.2: Surgical treatment

Spinal fusion surgery is a well-established surgical technique for treatment of IVD herniation in severe cases where long term symptoms are observed, and conservative treatment does not produce results. The spina fusion procedure aims to eliminate motion in the spinal segment, therefore eliminating motion induced pain symptoms and restoring original morphology. The mechanical characteristics of the segment are lost completely, which leads to increased load on the surrounding segments and degeneration in the long-term[61–63]. While this approach is technologically simple and utilizes well established methodology, a more biomechanically sound methodology has been developed where some of the mechanical properties of the spinal segment are preserved through arthroplasty. While the reduction in pain symptoms are similar[64], the long-term outlook is significantly improved[65,66]. An alternative to arthroplasty is posterior stabilization with a dynamic segment. While the pain symptoms are once again reduced by relieving the pressure on the IV[67] the degeneration of surrounding motion segments is still present[68–70].

Minimal invasive approaches for the above procedures have become more popular in recent years, while they significantly improve on the recovery time, hospital bills and soft tissue trauma, they also require more training and overall higher degree of skill[71]. However, the advantages seem to outweigh the drawbacks as these approaches have been gaining in popularity in the recent years[72].

Overall, there is a need for a repair technique that restores mechanical properties of the intervertebral disc in the long term, preferably in a biocompatible manner and manages the pain symptoms in the short and long term effectively. While some techniques like arthroplasty come close, they are inherently permanently introducing synthetic load bearing structures into the body, which carry long term risks to the patient. A more wholesome approach would be to promote repair in the disc through biological and regenerative medicine strategies.

2.3.3: Clinical Trials and Future Directions

The hallmark of regenerative medicine as currently understood is to introduce a treatment for injured organ that would allow the natural repair processes to proceed at an accelerated pace and manage short term symptoms to restore normal human function. The IVD presents a particularly difficult challenge for this approach. Firstly, the innate regenerative properties of the disc are severely limited by low cell numbers in a human disc which further diminish with age[73] and degeneration. Additionally, the tissue is poorly vascularized[74,75], therefore even if the cell populations can be increased, the survival of these populations in an environment designed for much smaller population is challenging. Secondly, as discussed previously, the IVD plays a crucial role as mechanical support for all normal human daily activities. Therefore, managing symptoms in an injured disc requires restoration of the mechanical function. All these considerations make the design of such a strategy exceedingly difficult. Currently, there are no clinically approved methods that fulfil these criteria. However, to approach an ideal solution two strategies are employed: designing a repair that is biocompatible, resorbable, restores disc mechanical properties and can be applied through minimally invasive surgery and stimulating the innate regenerative properties of the IVD through cell therapy.

Before stimulation of the in vivo repair mechanisms can be considered, the procedure for the initial intervention and application of the synthetic repair needs to be considered. The work described in this thesis focusses on developing a strategy which will fulfil the requirements for the synthetic repair, that is to provide a biologically and mechanically compatible repair that can be applied in a practical manner, while keeping the necessity for the viability and stimulation of the natural repair processes in mind.

2.3.4: Electrospinning for annulus fibrosus repair

The structure and morphology of the AF leads to a highly specific set of mechanical properties that the tissue possesses. Of note are anisotropic behaviour, where the stiffness in the circumferential direction is much higher than in the radial direction[76]. Furthermore, AF shows hyperelastic response during tensile loading[76–79].

There are suture[80] or anchor[81] repair methods that are currently used clinically. However these approaches are surgically complex and can introduce additional damage to the AF and surrounding tissues, increasing re-herniation risk[82].

Replicating the mechanics of the AF is crucial to restoration of the native function of the IVD. The most biofidelic approach would replicate the fibrous structure of the AF. This would allow to reproduce the anisotropy through the fibre orientation and enhance hyperelasticity through network reorientation[83]. The method of processing polymers into membranes made up of thin fibres known as electrospinning lends itself well to the task. The ability to tune fibre properties and network morphology as well as process a large variety of polymers and polymer blends allows to produce highly customizable networks suited to the application. Many studies have attempted to recreate AF behaviour with electrospinning. Several studies demonstrated that the angle ply structure made up of electrospun poly(ε-caprolactone) similar to that found in AF can replicate the mechanical characteristics of the AF[84–86]. In addition to pure biomechanics, several studies have been conducted to enhance the electrospun scaffolds with bioactive compounds to stimulate cellular activity and potentially accelerate tissue remodelling at the damage site. Favourable cell activity and gene expression on electrospun scaffold was reported: PECUU scaffolds[87], PCL scaffolds[88], PTMC scaffolds coated with PU membrane[89], PL and PCL scaffolds[90]. Vadal et al. loaded scaffold with TGF-β1, and observed enhanced ECM deposition in vitro[91].

2.3.5: Biomedical applications of electrospun scaffolds

While many types of cells can be cultured directly in medium, for proper differentiation and in particular to allow them to perform their function efficiently, ECM like environment is crucial[92–97]. Electrospun tissue engineering scaffold can function as templates for the growth of the tissue ex vivo, while also providing biomechanical cues. Or it can be implanted in vivo as temporary measure to provide mechanical support to restore normal functioning at the injury site and provide a scaffold for cells to conduct repairs. In addition, as the mechanical characteristics and surface chemistry on both macro and micro scale require optimizations, as the requirements vary between target tissues and applications. These scaffolds also need to be biocompatible, which means non-toxic resorbable and functional. Hence, the flexibility of electrospinning method to both produce a variety of polymers[98,99], morphologies and be functionalized with a variety of bioactive compounds is of utmost importance. Additionally, the flexibility of the geometry and motion of the collector broadens the available macrostructures and introduces the possibility to produce scaffolds with preferentially aligned fibres for biomechanically demanding applications.

The diameter of the electrospun fibres lies in the range of 100 nm to 10 µm[100,101]. While it is possible to spin thicker fibres, there are methods that are better suited and are more efficient at producing them. This size range lies comfortably within the ECMs scale. In addition, unlike other methods such as phase separation or self-assembly electrospun networks without additional manipulation produce scaffold with large surface area and open porosity. These factors allow for cell infiltration and proliferation within the scaffold, by providing ample surface for attachment[102,103] and rapid liquid diffusion within the network for normal metabolic activity. These three aspects mean that electrospinning is naturally similar to the extra cellular matrix (ECM) in which cells exist and interact [97,104,105].

Commonly addressed applications deal with mechanically dynamic organs and tissues, as these constructs require significant mechanical support both in tissue engineering applications and in vivo in regenerative medicine.

In cartilage and bone tissue engineering and regenerative medicine scaffolds have shown to support differentiation and metabolic activity of MSCs and Marrow cell[106–108]. The scaffolds in combination with an appropriate bioreactor were able to induce collagen I deposition and mineralization on the scaffold from mesenchymal stem cells (MSCs). Similarly, the cell seeded scaffolds have been implanted in vivo in non-union fractures and allowed accelerated fracture healing[109,110]. For Ligament tissue engineering, where the non-isotropic mechanical properties are required as well as relatively high stiffness, aligned electrospun fibres are often used to mimic the natural tissue with bundles of aligned collagen fibres. For example, scaffolds are used for blood vessel tissue engineering as well as a component in stents, because the network and material properties combined can accommodate large dynamic strains without breaking[111]. Rotating drums are used to produce aligned fibres which are then seeded with fibroblasts[112]. As skin dressing, once again the elasticity of the network as well its porosity is crucial here. In addition, the scaffolds are often loaded with compounds that promote regeneration and reduce inflammation at the injury site.

2.4: Electrospinning

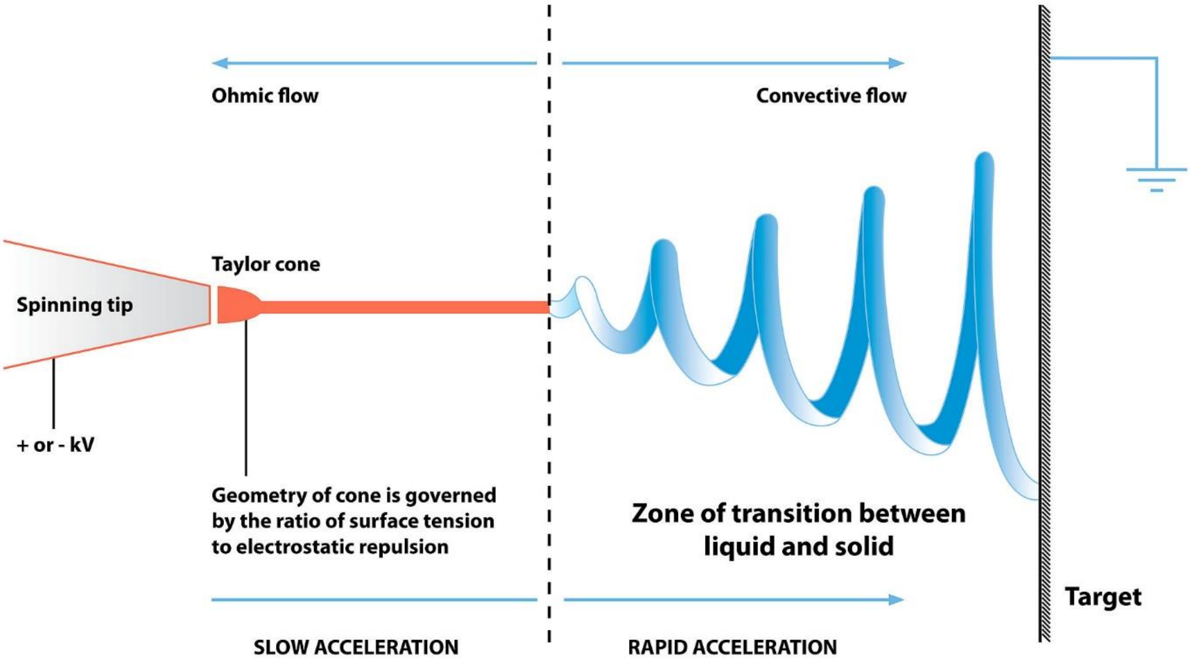

Figure 2-4: Diagram showing fibre formation by electrospinning.

Diagram by Joanna Gatford at The New Zealand Institute for Plant and Food Research Ltd

Several techniques are available in literature for production of nanomaterials such as self-assembly, solvent casting, phase separation, and electrospinning techniques[113–115]. Electrospinning has becoming increasing popular in the recent years. Electrospinning has several advantages over other techniques as it allows to produce membranes with a large surface area to volume ratio and reliably open porosity[116]. In addition to the functional advantages of the electrospun scaffolds, the manufacturing process is relatively robust, utilises equipment widely available in labs and is versatile. This has led to many publications that describe electrospinning techniques for various polymers, desired morphologies and environments further driving the popularity of electrospinning as method to produce nanofibers. The need for nano-porous scaffolds with open porosity and high surface area exists in many fields, most frequently those dealing with filtering, catalysis and bioengineering[117–119]. While filtering is mostly concerned with porosity and catalysis with surface area, bioengineering requires both specific porosity and fibre diameter as well as a specific materials and material properties to satisfy mechanical and biological requirements of the application. Apparent suitability of electrospinning for biomedical applications is illustrated by the large number of publications produced yearly on the subject. The large material selection offered by electrospinning mans that many biocompatible and biodegradable of both synthetic and natural origin can be processed in this manner. Scaffolds produced using these polymers allow to fulfil not only the basic biocompatibility requirements but can also promote effective cell proliferation with good attachment and proliferation. Furthermore, the ability to incorporate drugs and bioactive molecules into the biodegradable polymers, introduced yet another layer of functionality to the electrospun scaffolds. To effectively manufacture these scaffolds with the specific requirements for the biomedical applications or otherwise a thorough understanding the manufacturing conditions associated with electrospinning is required. While many papers show empirical evidence of spinnability of a wide range of polymers and resulting scaffolds, theoretical understanding of the method remains limited.

2.4.1: Electrospinning process

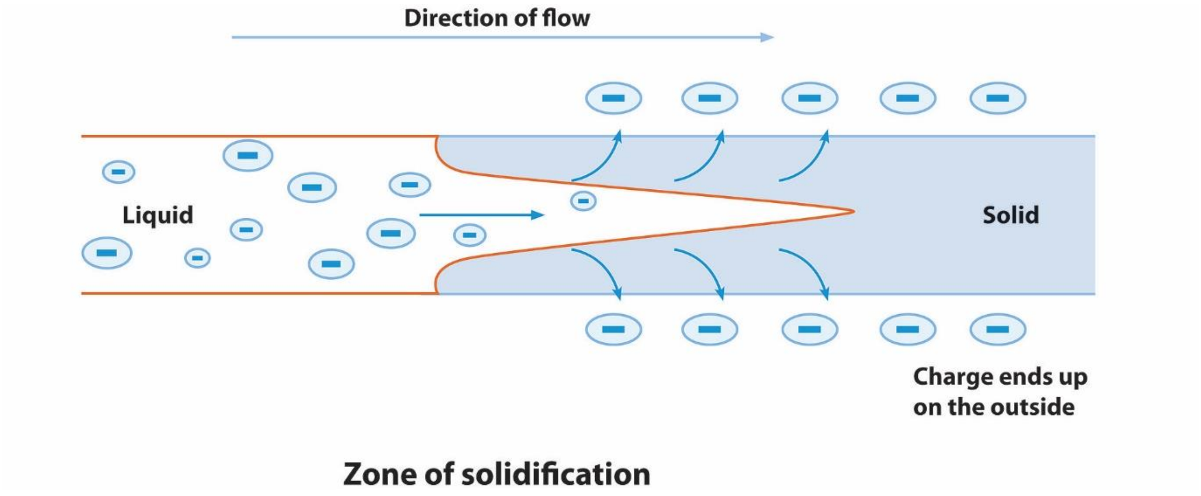

Figure 2-5: How the distribution of charge in the fibre changes as the fibre dries during flight.

Diagram by Joanna Gatford at The New Zealand Institute for Plant and Food Research Ltd

As the focus of this work is on biomedical applications, the electrospinning process as used in the context of this application for the research purposes will be discussed. Other industries use variations on this process, while the core principles remain the same the differences in requirements mean that specifics differ significantly. At its core, the electrospinning setup consists of four basic components: the solution of polymer in a solvent, glass syringe with a metallic needle, the electric potential applied between the needle in which the solution is contained and the collector, and finally the collector itself. The variations in the shape, composition and relative position of these components dictates the material properties as well as the morphology of the membrane on both macroscopic and microscopic scale. The process of creating a polymer fibre from a solution is initiated by the application of electric potential to the metal needle, which leads to the induction of charge at the polymer droplet protruding from the needle opening. The repulsion of charges accumulated at the surface of the droplet counteracts surface tension and results in the ejection of a solution stream. This process in equilibrium is characterised by a broadly triangular solution cone at the needle tip, known as Taylor cone[120]. The ejected solution stream travels though the space between the source and the collector as a single fiber[121,122], in which time it dries and lands on the metallic collector to produce a solid polymer fibre network. In the space between the source and the collector, the jet undergoes whipping motion as a result of Rayleigh instability[121]. The whipping motion draws the fibre and reduces the diameter to the nanometre scale.

Broadly speaking the success of the production process can be qualified in terms of achieving the desired morphology, which can be further characterized by the fibre diameter, fibre curvature and pore size, as well as homogeneity of these parameters throughout the network. There is no consensus on the exact mechanisms that control the resultant material properties of the fibres during the ejection flight and collection. However, many studies have provided empirical evidence showing alterations in certain process parameters can lead to changes in crystallinity, crystallite and amorphous chain alignment within the fibre and changes in network morphological properties.

Overall, the controllable parameters that affect the desired properties are voltage, viscosity of the polymer solution, dielectric properties of the solution, flowrate of the solution, geometry of the collector and the source as well as their distance from each other. While the setup of the collector and the source is rather varied between different setups, it is also difficult to change. The distance between the collector and source is largely fixed to allow for evaporation of the solvent and collection of dry fibre, while being shortest possible to allow for a stronger electric field and lower voltages[123]. Therefore, in the context of bioengineering a basic model of single needle tip and flat collector or a rotating drum collector is used when the aim is to investigate and compare the other parameters. Flowrate is tuned to the specific setup and rarely considered as a control parameter, as only a narrow effective flowrate exists for every configuration of other parameters. The flowrate is usually chosen to be the minimum possible to achieve a stable Taylor cone[124,125] and is therefore dictated by the choice of voltage and solution properties for a given setup. As such the effects of voltage applied to the source coupled with its distance to the collector, as well as solution composition are of primary interest for the purpose of achieving high quality electrospun membranes for bioengineering and regenerative medicine applications. In addition, ambient parameters such as humidity and temperature have a significant effect on the process.

2.4.1.1: Effect of voltage on geometry of electrospun fibres

Commonly, thinner polymeric fibres cab be achieved by increasing the voltage at the source, as the increase in voltage is responsible for increasing the repulsive forces in the solution and consequently believed to increase the jet velocity and decrease the jet diameter[126–128]. However, some researchers have observed a non-linear relationship between diameter and voltage[129–131]. This was attributed to the interplay of the drawing velocity as in the other studies, but here coupled with drying of the fibre. The two effects lead to a non-linear relationship.

2.4.1.2: Effect of solution viscosity

Solution viscosity driven by the choice of solvent and polymer concentration in turn has a strong effect on formation of the Taylor cone and the stretching of the polymer jet. While the proper shape and stability of the Taylor cone will affect the overall quality of the produced fibres, the deformation induced on the fibres through stretching will lead to formation of thicker fibres in case of a viscous solution or thinner fibres and even break up into droplets for solutions with low viscosity, which is known as electrospraying [116,130–139]. The effects of stretching and surface tension during flight are balanced by the chain entanglements in the polymer solution, and prevent fibre break up. The quantitative effect of viscosity on the fibre diameter is dependent on the polymer and its chain length, and is commonly formulated a s power law relationship[140–142]. The practical limits however dictate that a solution that is too viscous will be too difficult to pump to pump through the system and can also dry at the tip of the needle hampering the process. This can however be solved by the addition of solvent saturated vapour shield at the needle tip. A side effect of increasing solution viscosity and fibre dimeter is that the evaporation of the solvent might take longer than the flight, leading to fused fibres at the collector[132,134,141,143]. The exact viscosity that is spinnable is dependent on the polymer that is spun and the dielectric properties of the solution.

2.4.1.3: Effect of solution conductivity and dielectric properties

Dielectric properties define the susceptibility and permittivity of the chosen solution. Permittivity affects how much charge can be built up on the surface of the drop to counteract the surface tension and create the Taylor cone. While susceptibility defines how much potential needs to be applied to achieve the desired result. Both these values define the voltage that needs to be applied to produce a stable cone and fibre in a given electrospinning setup. The dielectric properties of the solution are of course determined by the choice of polymer and solvent. While the polymer is often dictated by the application and desired material and mechanical properties, the choice of solvent is in turn limited by the polymer. In general, increasing permittivity of the solution will increase the charge on the droplet surface and lead to the decrease in fibre diameter[144].

The conductivity can be further modified by the addition of salts such as NaCl, KH_2PO_4, NaH_2PO_4 to the solution as they increase the ionic content of the solution, as well as adding dimensionally small ions thus increasing its conductivity[112,116,143,145]. The increase in the conductivity of the solution is commonly associated with decrease in the fibre diameter[130,131]. This is explained by increase in charge density and consequently higher stretching forces on the fibre associated with the electric potential applied at the needle.

2.4.1.4: Humidity and temperature

Humidity and temperature play a crucial role in creating a stable electrospinning environment as they affect all other parameters such as viscosity, surface tension, evaporation of the solvent and dielectric properties. It is therefore extremely important to have a consistent and controlled environmental conditions to obtain reproducible results. In general increasing temperature leads to lower solvent viscosity and marginally faster evaporation of the solvent, which in turn results in smaller fibre diameters[146]. While increasing humidity has a significant impact on solvent evaporation, which leads to variations in fibre surface topology and overall drying of the fibres similarly to changing from highly volatile solvent to low volatility solvent.

While utilizing the above considerations to achieve the desired fibre and network morphology it is important to remember that a change in one parameter will require an adjustment in other parameters. Therefore, a parameter space in which a stable process exists is rather narrow, and individual parameters cannot be varied independently.

2.5: Limitations of prior work and thesis aims

The authors identified two key limitations of the work previously done on finding a satisfactory solution for a biocompatible repair of IVD herniation and specifically failure of AF on the periphery.

Firstly, previous work documented limited investigation into mechanics of electrospun scaffolds in the scope of biocompatible repair in vivo, especially when considered in the long term. Therefore, one of the key goals of the work presented in this thesis is associated with generating a clear understanding of the mechanical response of the electrospun networks at micro and macro scale subjected to long- and short-term loads and strains closely associated with the intended application.

Secondly, no repair solution described in literature showed a significant mechanical restoration of the IVD when subjected to forces associated with large animals. To validate the proposed repair strategy, an ex vivo model that closely simulates the mechanical environment of the human IVD under physiological loading was proposed and investigated. The repair strategy informed by the investigation into mechanical behaviour of the electrospun networks was tested on the newly developed model.

Chapter 3: Mechanical evaluation of electrospun poly(ε-caprolactone) single fibres

Dmitriy Alexeev[1], Nils Goedecke[1,2], Jess Snedeker[1,2], Stephen Ferguson[1]

[1] ETH Zurich, Institute for Biomechanics, Zurich, Switzerland

[2] University of Zurich, Department of Orthopaedics, Zurich, Switzerland

Published as:

Alexeev, D., Goedecke, N., Snedeker, J. & Ferguson, S. Mechanical evaluation of electrospun poly(ε-caprolactone) single fibres. *Mater. Today Commun.* **24**, (2020).

DOI: https://doi.org/10.1016/j.mtcomm.2020.101211

3.1: Abstract

In the scope of biomechanical applications of electrospun polymer microfibers, a new method for testing single electrospun microfibers was used to reliably establish mechanical properties of poly(ε-caprolactone) microfibers within a wide range of diameters from 0.4 to 6.0 µm. Cyclic mechanical tests were used to establish a bimodal linear relationship between fibre diameter and Young’s modulus. An inflection point was found at approximately 0.9 µm, where a sharp increase in modulus below this diameter was observed. The abrupt rise in modulus was not observed on the same scale in scaffolds produced with corresponding fibres and could not be explained only through a change in crystallinity of the polymer. Furthermore, the elastically recovered strain was assessed at maximum strain up to 20%. It was found that polycaprolactone exhibits a viscoelastic range up to 13.17 ± 3.1% after preconditioning, which is sufficient for most relevant biomechanical applications.

3.2: Introduction

Electrospun (ES) poly(ε-caprolactone) (PCL) is widely used as a substrate for tissue engineering (TE) and as a mechanical support in regenerative medicine, because the scale and the morphology of the ES networks can closely mimic those of the extra cellular matrix[147–149]. Macroscale applications for such networks are often associated with the repair of tissues that have a significant elastic character and undergo regular dynamic stresses. These include, but are not limited to, the cardiovascular system[150–152], skin[153,154] and other collagen based tissues such as tendons, ligaments and the annulus fibrosus of the intervertebral disc[155,156]. In this context, understanding the specific mechanical properties required to guide cellular activity[157–159] and resist deformation in a cyclic loading environment with potentially large strains is necessary[160,161]. In addition, understanding the micromechanical properties of electrospun PCL is relevant for the development of theoretical models of the macroscale behaviour of the scaffolds[83,162,163] and for the precise definition of process parameters to produce membranes with the desired characteristics. Specifically, the mechanical properties of the single electrospun fibre, and the relationship between single-fibre properties and those of the final membrane, must be comprehensively described.

While more complete works on commonly used electrospun materials such as Nylon have been completed[164], information on materials commonly used in tissue engineering applications is generally lacking. In particular, the fibre diameters above 2 µm used in in vitro and in vivo applications that have been shown to be required for nutrient access and efficient cell infiltration[165,166]. Previous works on PCL have characterized its mechanical behaviour, albeit only in the range below 2 µm of fibre diameters[167–171].

While PCL exhibits isotropic mechanical properties when produced in bulk, at the scale of single fibres, other factors must be considered which may influence the measured response. At the high drawing ratios and fast drying conditions achieved by electrospinning, the polymer chain alignment and crystallinity of the material can be directly influenced by the production process[167,172]. Both have a strong influence on the mechanical properties of the overall networks as they lead to anisotropic mechanical response on the single fibre level.

In this study, a robust method was developed to allow for the collection of single fibres and to facilitate the direct measurement of mechanical properties of electrospun single fibres in both single and cyclic deformation modes. The method was used to determine the mechanical properties of single fibres with a comprehensive range of diameters under cyclic loading conditions. We hypothesize that the mechanical properties of the single fibres are dependent on crystallinity, and that crystallinity in turn is dependent on processing conditions which are used to achieve a certain fibre diameter. Therefore, there is a direct relationship between single fibre diameter and the measured mechanical properties. For additional context, the mechanical properties of electrospun membranes were also measured for comparison.

3.3: Methods

3.3.1: Materials

Polymer solutions for electrospinning were prepared using only polycaprolactone (PCL, M_n 80,000, Sigma-Aldrich), chloroform (>99.8% pure, Fisher Scientific) and methanol (analytical grade, M/4000/15) mixture. In Table 3-1, the various formulations used to achieve different fibre diameters are summarized. Additionally, to obtain a scaffold made up of very thin single fibres of sub 200 nm diameter, a different solvent composition based on formic acid-acetic acid (9:1) with PCL concentration of 22 % wt.

Table 3-1: Table of electrospinning solution recipes for varying fibre thicknesses.

Fibre Diameter [um]	**Chloroform [parts]**	**Methanol [parts]**	**PCL [% wt.]**
0.4 – 1.4	6	1	8 – 12
1.2 – 4	12	1	12
4 – 7	24	1	12

The method for producing freestanding single fibres was adapted from the work by Tan et al.[172]. The electrospinning solution was loaded into a glass syringe (5 ml, Fortuna W.G.Co), and a flexible Teflon tube was attached to the syringe terminating with a blunt metal needle (0.8 mm ID, 1.0 mm OD). A positive voltage source was attached to the metal needle at 16 – 20 kV. Two grounded vertical collector pillars with a separation of 50 mm were placed at a distance of 175 mm from the needle. The solution was spun for a brief period until several freestanding fibres appeared between the pillars of the collector as seen in Figure 3-1. Electrospinning was performed in an environmental chamber (Parameter Generation & Control), with conditions kept constant at 24 °C and 40 % relative humidity.

The full electrospun membranes were produced using the same conditions as the single fibres. The spinning was carried onto a drum collector (d = 7.5 cm) rotating at 1 rpm. The spinning time was 15 hours and flow rate was 26 µl/min.

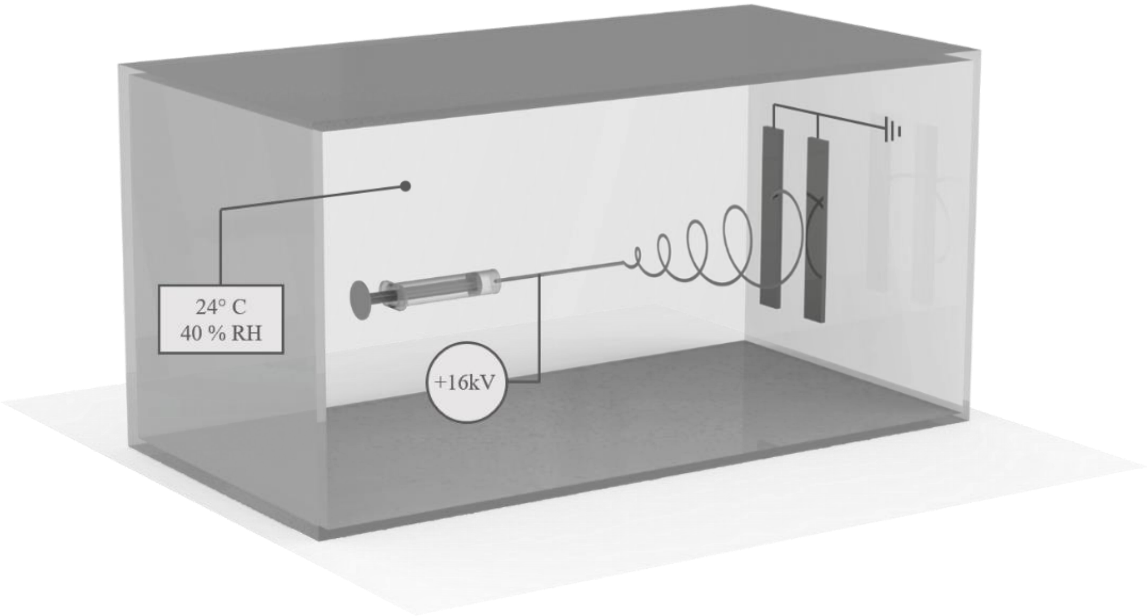

Figure 3-1: Environmentally controlled electrospinning setup.

3.3.2: Mechanical testing

Freestanding single fibres were transferred from the collector pillars by directly placing them between two metal plates as shown in Figure 3-2. The plates were tightly screwed together to prevent movement in the fixed sections and clamp the fibres. The samples were then imaged with an optical microscope prior to testing to obtain the deviation angle as well as to evaluate fixation and quality consistency of the fibres. fibres with significant inconsistencies such as inconsistent diameter or large morphological defects were excluded from the testing procedure.

A FemtoTool mechanical testing machine with 100 µN (±5 nN, FT-S100) sensor was used. The fibres fixed in the holder were placed into the FemtoTool and optical microscope assembly. To manipulate the fibre, a tungsten hook (Pacific Instruments, d = 200 µm) with 120° bend was glued on to the tip of the sensor. The hook was positioned in the centre of the opening in the holding plates and adjusted to be in plane with the fibre.

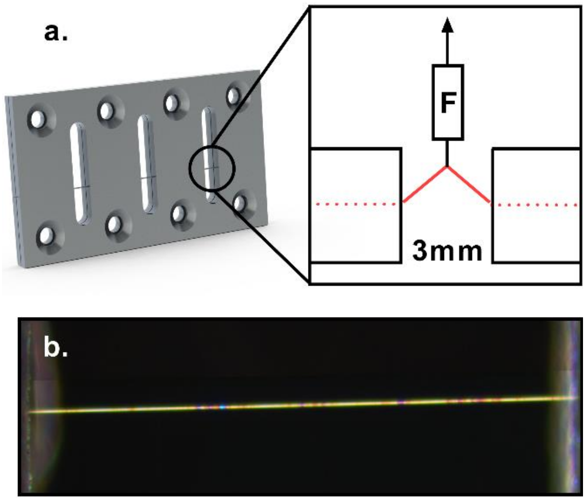

Figure 3-2: Fibre clamped between plates and a schematic of extension applied (a). Polarized light microscopy image of e-spun fibre in holder (b).

Cyclic mechanical tests were carried out by displacing the hook in the vertical direction as shown in Figure 3-2. Four end displacement values were investigated: 480 µm, 687 µm, 852 µm, 995 µm at a rate of 60 µm/s in 4 µm steps (device-dependent). These values translate to 5, 10, 15 and 20 % extension and strain rate of 1 – 4 % per second. Stress and strain were calculated from geometry using the following equations:

Strain: $\varepsilon = \frac{\sqrt{x_0^2+z^2}-x_0}{x_0}$ where x_0 is initial length and z is the vertical displacement.

Force: $F = {}^{F_z}\!\Big/_{2 * \sin\left(tan^{-1}\frac{2z}{x_0}\right)}$ where F_z is the force measured by the sensor in the z (vertical) direction.

Stress: $\sigma = {}^{F}\!/_{x_0} * \pi r^2$

Modulus values were then extracted from the data by evaluating the apparent linear section of the stress vs. strain data. Hysteresis was calculated by subtracting the area under the unloading curve from the area under the loading curve. Elastically recovered strain was calculated as a strain value between the maximum strain reached in the cycle and when the unloading cycle stress reaches 0 value, at which point the fibre would become slack.

To test the membranes, dogbone pieces (area: 138 mm^2, length: 50 mm) were punched from each sample. These underwent cyclic extension mechanical testing on Instron E10000 machine with a 200N sensor (KD24s, Transmetra). Strain rate of 0.5 mm/s with 4 cycles at each of the 6 strain steps, each increasing by 5 percent (5, 10, 15, 20, 25 and 30 % strain) was used. Stress was calculated $\sigma = F/(\frac{wm}{A\rho})$, where F is force, w is width (2 mm), m is mass of the dogbone, A is the area of the dogbone (138 mm^2) and ρ is density of PCL (0.001145 g/mm^3).

All tests were performed in a normal lab environment, dry and 24ºC.

3.3.3: Imaging

During mechanical testing, the samples were observed and imaged using an optical microscope with a dark field attachment. Following testing, the precise diameter of each fibre was determined from the untested section using scanning electron microscope (Quanta 200F FEI) after coating the fibres with a 10 nm gold layer.

3.3.4: Dynamic scanning calorimetry

Dynamic scanning calorimetry is a well-established method for measuring enthalpy of melting, from which crystalline fraction of the polymer can be calculated. Assuming the polymer is pure and free of solvent the method is precise [173]. DSC measurements were performed using DSC 822 (Mettler Toledo) on representative electrospun membrane samples produced using the same conditions as the single fibres. The polymer sample was heated at 10 °C/min from -40 °C to 100 °C. The crystalline fraction of the polymer was calculated based on the endothermic transition on first heating and reported enthalpy of fusion for 100 % crystalline polycaprolactone 139.5 J/g [174].

3.3.5: Statistical Analysis

Significance was established by $p \leq 0.05$. Linear regression analysis was used to identify the relationship between single fibre diameter and Young’s modulus. Two-way ANOVA was used to evaluate the grouped cyclic mechanical data. Prism 8 software was used for statistical analysis.

3.4: Results

A representative stress versus strain curve with multiple loading cycles at different strain steps for such fibres is presented in Figure 3-3, showing the four strain levels of 5, 10, 15 and 20 % as well as repeated cycles at each strain level. The noise associated with geometric conversion to longitudinal strain at low deflection angles is < 0.5 % strain.

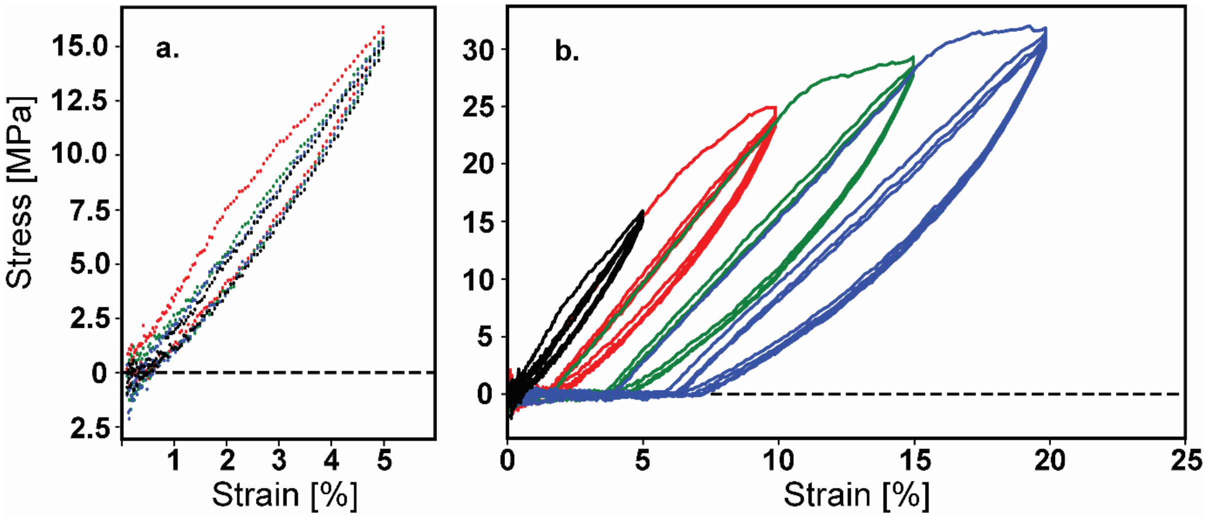

Figure 3-3: Representative stress versus strain curve for fibre with diameter of 0.87 µm. 4 cycles up to 5 % strain (a) and up to 20 % in 5 % strain steps with 4 cycles in each step.

The data on the relationship of fibre diameter to the modulus of single fibres in Figure 3-4a suggests that fibres with lower diameter have higher modulus; however, the relationship is not linear. It was found that, below approximately 1 µm fibre diameter, there is a steep increase of the modulus with decreasing diameter, characterized by a linear regression fit ($R^2 = 0.71$, $p < 0.0001$, $n = 21$). Above 1 µm there was no correlation between the diameter of the fibre and modulus.

The crystalline fraction obtained through DSC measurements shows a small linear increase from 43 ± 2 to 47 ± 3 % with decreasing fibre diameter from 6.73 ± 0.51 to

0.74 ± 0.23 in Figure 3-5.

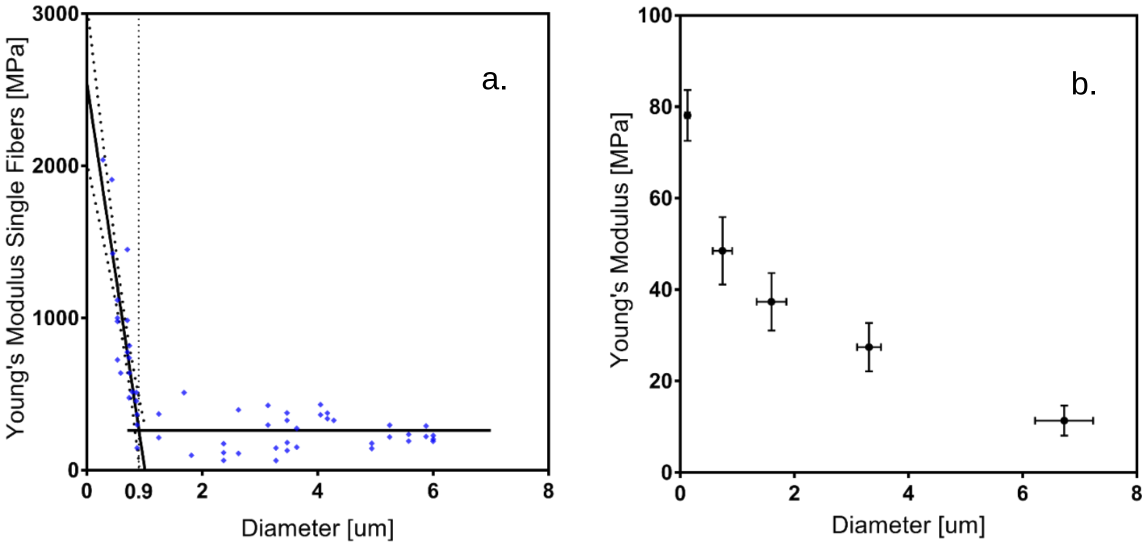

Figure 3-4: Young's modulus variation with respect to fibre diameter can be seen for both single fibres (n = 56) (a) and e-spun mats (b) (n = 18 per data group). For regression fit d < 0.9 µm p<0.0001 R2=0.70; for d > 0.9 µm no correlation. Regression line in solid stroke and confidence interval in dotted line.

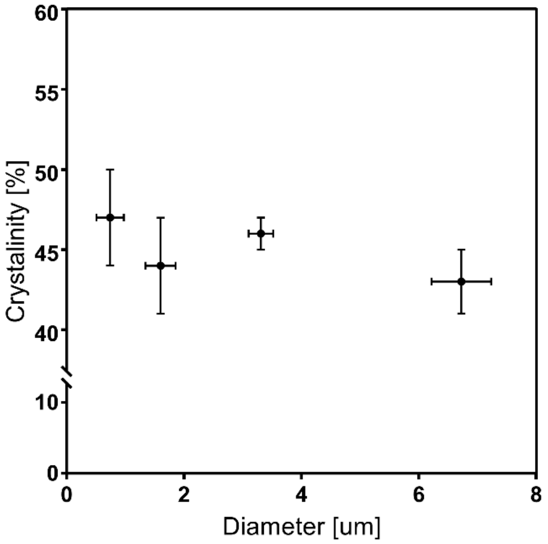

Figure 3-5: The crystalline fraction determined through DSC measurements at different fiber diameters is shown.

There is a significant plastic deformation after the first loading cycle, which is evident from a decrease in loading energy and hysteresis quantified in Figure 3-6a. The reduction in hysteresis increases significantly with strains above 5 %. Furthermore, the following loading cycles showed significantly lower reduction in hysteresis in the range of 5 ± 3 % with no significant difference between different maximum strain levels. As can be observed in Figure 3-3, above approximately 5 % strain the fibre does not return to its original length. This deformation is not recovered over time. Figure 3-6b quantifies the strain that is recovered elastically from the maximum strain reached during the cycle. The stable elastically recovered strain showed an expected increase from 4.34 to 13.17 % with 5 to 20 % maximum strain, which translated to 87 to 66 % of the viscoelastic range normalized as a fraction of maximum strain. No correlation was found between elastically recovered strain at all maximum strains and fibre diameters.

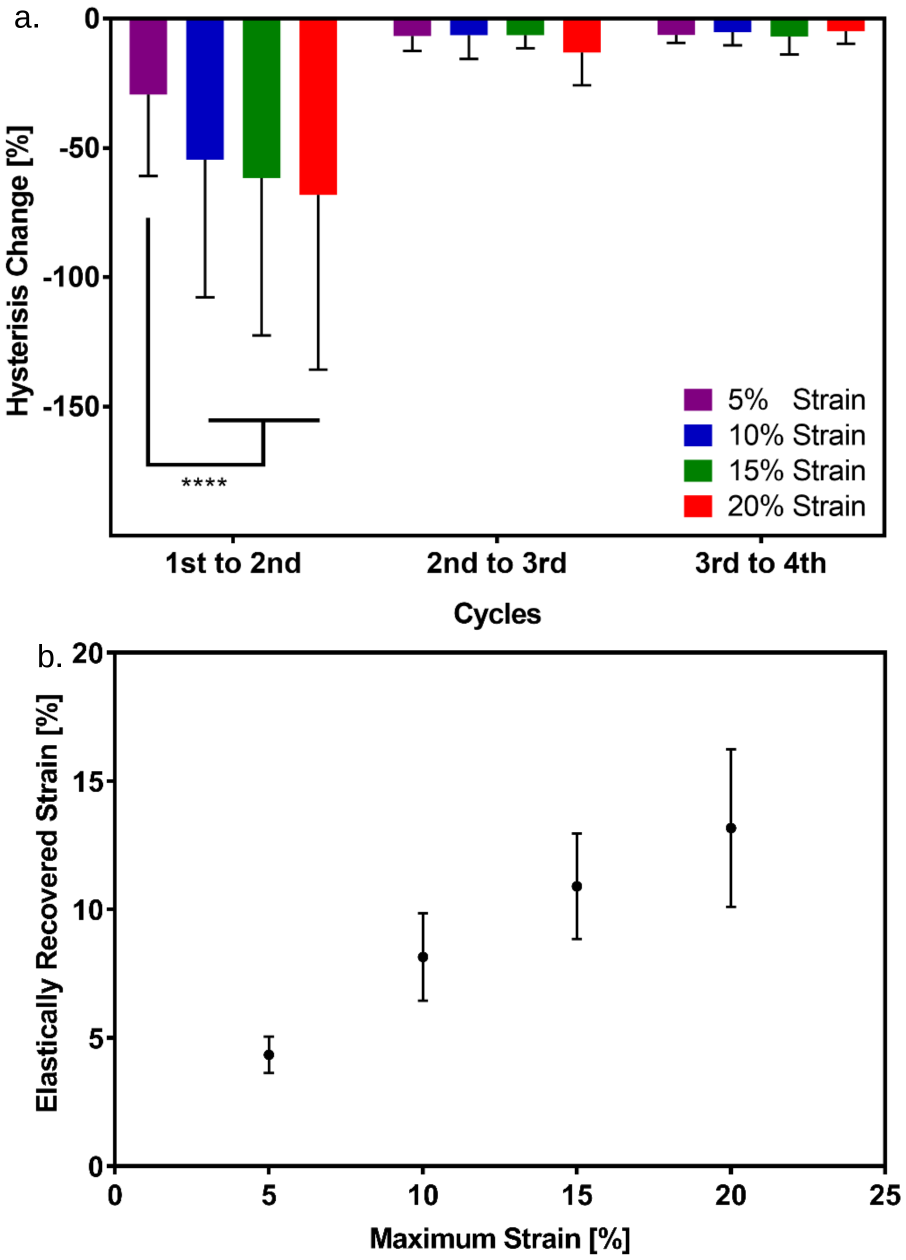

Figure 3-6: Change in hysteresis after 1st, 2nd and 3rd cycle at each strain step denoted with maximum strain (a). Average elastically recovered strain of 2nd, 3rd and 4th cycles at different maximum strain levels (b). n = 56 (b)

3.5: Discussion

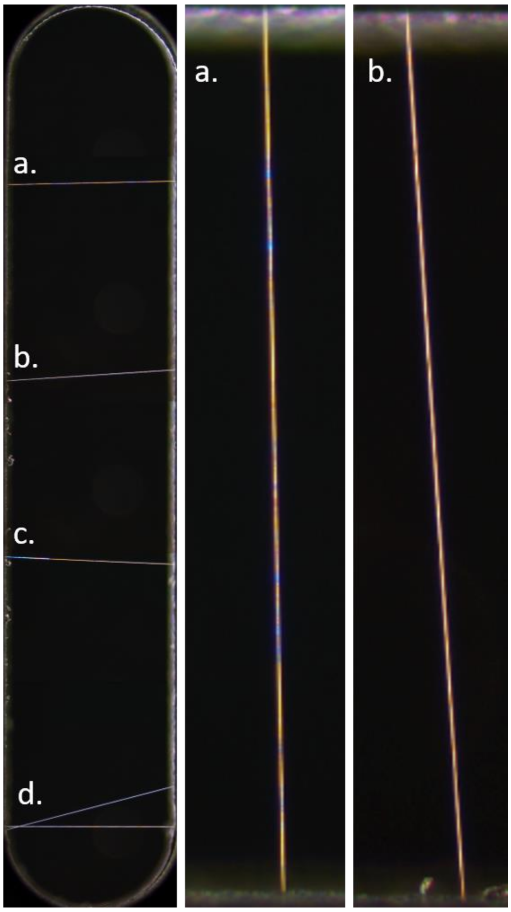

Figure 3-7: Image, obtained under dark field conditions, of single fibers clamped in the holder prior to mechanical testing. d = 0.87 (a), d = 0.86 (b). The gap is 3 mm.

The new collection and testing method allowed for an efficient and robust fibre collection process, as many fibres were captured simultaneously in a single holder and fixed for tensile testing, Figure 3-7. This is a major limitation of previous methods that allowed for only a single fibre per holder, and relied largely on operator precision during handling [169,170]. In addition, direct optical observation of the sample prior to and during testing ensured consistency in fixation, testing and fibre quality, despite the sensitivity of the electrospinning method as well as the mechanical testing setup. The first few seconds in the electrospinning process, when the Taylor cone is established, are inherently unstable. However, to produce free standing single fibres, this time period must be used, which means that an evaluation of the quality of the fibres prior to testing is imperative, to produce representative and reliable results.

Electrospun PCL networks are often used as substrates for tissues that undergo cycling loading. It was therefore important to characterize the mechanical behaviour beyond a single loading cycle, and to quantify the expected plastic deformation when exposed to increasing levels of tensile strain. The strain steps, strain rate and testing mode were chosen such that they were relevant for biomechanical conditions that such scaffolds might experience in commonly considered applications, listed in Table 3-2.

Soft tissues, as seen from the table, experience large strains that the membrane needs to accommodate and ideally still elastically recover.

	Strain [%]	Strain Rate [%/s]
Skin	25 - 30 [175]	0.1 – 10 [176]
Heart muscle	1.5 – 14 [177]	(1.3 – 3 Hz, Heartbeat)
Tendon	5 – 9	5 – 9 (1 Hz, Walking) [178]
Aorta	6 – 15	8 – 40 (1.3 – 2.7 Hz) [179,180]
Intervertebral disk	2 – 10	4 – 20 (2 Hz, Walking) [181]

Table 3-2: Table of typical strains and strain rates experienced by human soft tissues, that are commonly targeted in regenerative medicine applications involving electrospun membranes.

The most widely reported value in literature, Young's modulus, was evaluated. This study found similar moduli for PCL single fibres to those previously reported: 200 – 500 MPa for 1 – 6 µm diameter and 300 – 2500 MPa for 0.28 – 1 µm. In previous works Wong et al. reported 250 – 300 MPa for the 0.5 to 2.5 µm diameter range [169], and Lim et al. reported 100 – 3000 MPa for the 0.2 -1.2 µm [168] using traditional tensile testing. Croisier et al. reported 3700 MPa for the 0.15 – 0.35 µm range using AFM and 3 point bending test [167]. All the above studies used PCL with molecular weight of 80000 g/mol. The results by Baker et al. who reported 10 MPa to 310 MPa for 0.44 – 1.04 µm fibre diameter range using AFM to induce large strains up to 95 % [171]. The last study shows rather lower values than the rest, likely due to higher molecular weight of the PCL used (120000-300000 g/mol). Extruded PCL films have been reported to have modulus of 190 – 375 MPa [182,183], which coincides well with the values found for the larger single fibres. It can therefore be concluded that significant change in the mechanical properties with respect to dimensional parameters for electrospun PCL is only relevant below 1 µm diameter.

In isotropic homogeneous materials, sample geometry should have no effect on the modulus. It is however well established that a unique property of electrospun fibres is inhomogeneity resulting from the production process, where drawing in conjunction with rapid drying leads to a significantly different microstructure between the surface regions of the fibre and the bulk [164,168]. The surface has highly aligned amorphous regions, while the bulk has lower alignment. The increase in surface to bulk ratio with decreasing fibre diameter should lead to a change in underlying material mechanical properties and an increase in modulus.

The fibre diameter had no measured effect on modulus above 1 µm fibre diameter, likely due to the surface region being negligibly small. In Figure 4a there is a sharp rise in Young's modulus below approximately 1 µm. The abrupt change can be explained by a rapid increase in surface to bulk ratio. The surface region should have a higher amount of aligned amorphous regions as described by Lim et al. [168,184]. The fibre overall should have an increased crystalline content, similarly to extruded fibres, due to increased drawing ratio. Supporting this theory, in this study the abrupt change cannot be explained purely by an increase in the crystalline content of the fibre, as the crystalline fraction determined through DSC measurements did not demonstrate the same relationship to the fibre diameter, shown in Figure 3-5. This behaviour is consistent with several other works done on the topic for PCL as well as other semi-crystalline polymeric materials [169,170,185–188]. The assessment of crystalline fraction of sub 200nm fibre diameter scaffolds was not performed due to the different solvent composition. The acid based solvent would evaporate at a substantially different rate and therefore it would have a significant effect on crystalline fraction [184], consequently these scaffolds would not produce representative values for the main electrospinning process utilizing chloroform and methanol solvent.

Fibre diameter is often reported as a selection and characterization criterion for the electrospun scaffolds and resultant desired mechanical behaviour. Although the underlying material properties of the single fibre influence the resultant scaffold properties, it is clear when comparing Figure 3-4 a and b that this relationship is not direct. The high tensile modulus of thin fibres does not translate to a change of the same magnitude in the modulus of the network. This is largely due to method-dependent parameters such as inter fibre adhesion[189] and curvature[190]. These parameters affect the fiber-fiber interactions which play a key role during fibre reorientation under stress[83,191] and lead to mismatch between the membrane and single fibre mechanics. The observations performed on electrospun networks are also supported by multiple computational models[191–194]. The inter fibre adhesion as well as curvature in the membranes should be evaluated in future work with direct imaging of relative fibre motion under loading. It must be further noted that to calculate the modulus of the membranes, density measurements were used instead of cross-section, as the cross-section measurements are unreliable due to very low cross-sectional stiffness of the networks. Because density of PCL fibres can vary slightly due to changes in crystalline fraction and drawing ratio of the fibres, a small error is likely present in the modulus calculations.

Optical observation of the fibres for the purposes of the quality control revealed a large number of small structural defects in some fibres. These observations were performed qualitatively using dark field optical microscopy in Figure 3-7. Fibre a. (d = 0.87 µm) shows colour variation along its length which highlights structural defects, while fibre b. (d = 0.86 µm) of similar diameter is consistent. Similar defects are observed on fibres of larger diameter. It was not possible to relate the observed defects to specific material characteristics, as the observations are likely a result of both morphological and multiple material variations. Furthermore, this observation was not confirmed on the electrospun membranes, as the opacity of the PCL fibres precluded appropriate light transmission on larger samples. If confirmed on the membranes, the presence of these defects could play an additional role in affecting how the underlying fibre properties translate to the membrane properties for fibres of different diameters. However, quantitative assessment requires a different technique to characterize the defects and distinguish both origin and magnitude.

Due to the nature of the loading setup, the strain rate is variable between 1 – 4 % strain per second, which corresponds to cyclic loading in the sub 1 Hz range for the strain steps evaluated. Therefore, it is not possible to perform a standard viscoelastic characterization with the proposed technique. However, it is possible to provide functional quantification of the mechanical response.

PCL fibres exhibit a classic viscoelastic response to tensile loading, with a significant plastic character. During cyclic testing, PCL single fibres showed significant reduction in hysteresis after the first cycle, indicative of plastic deformation. The relative increase in plastic loss with increasing maximum strain highlights the limitations of using this material in applications with exceptionally large strains. However, at each strain level the viscoelastic region appearing after the first loading cycle quantified in Figure 3-6b can be utilized in such cases. The size of this region is larger at higher strains but accounts for a smaller portion of the overall displacement. These characteristics must be considered when preparing the sample, as precise mechanical preconditioning will be necessary to achieve desired viscoelastic behaviour.

In the future the data obtained using such a methodology will allow for the optimized design of PCL electrospun networks and facilitate the development of more precise computational models.

3.6: Conclusion

The application of the new testing methodology for single fibres allowed to produce exceptionally reliable measurements on a wide range of fibre diameters. Young's modulus showed an abrupt increase with decreasing fibre diameter with an inflection point below 1 µm. Randomly oriented scaffolds produced using the same conditions did not show the above-mentioned relationship, likely due to complex fiber-fiber interactions present in the scaffolds under strain. Furthermore, the mechanical properties could not be solely explained through change in crystallinity. The technique also allowed to investigate cyclic mechanical loading in the strain range and frequency relevant for major regenerative medicine applications. This data was used to show that an elastically recoverable range of 4.3 to 13.2 % exists for single fibres at strain levels of 5 to 20 % respectively. These findings put PCL single fibres well in the range for most biomechanical applications. In addition, the viscoelastic range can be further enhanced thought the scaffold geometry. Consequently, future work will be focused on applying the findings to design scaffolds with appropriate properties to provide mechanical tissue support in regenerative medicine applications.

Chapter 4: Electrospun biodegradable poly(ε-caprolactone) membranes for annulus fibrosus repair: Long-term material stability and mechanical competence

Dmitriy Alexeev[1], Melanie Tschopp[1], Benedikt Helgason[1,2], Stephen J. Ferguson[1,2]

[1] ETH Zürich, Institut für Biomechanik, Zürich, Switzerland

[2] Collaborative Research Partner of AO Foundation, Davos, Switzerland

Submitted to *JOR Spine* as:

Alexeev, D., Tschopp, M., Helgason, B. & Ferguson S Electrospun biodegradable poly(ε-caprolactone) membranes for annulus fibrosus repair: Long-term material stability and mechanical competence.

4.1: Abstract

Electrospun (ES) poly(ε-caprolactone) (PCL) is widely used to provide critical mechanical support in tissue engineering and regenerative medicine applications. Therefore, there is a clear need for understanding the change in the mechanical response of the membranes as the material degrades in physiological conditions. Electrospun membranes with fibre diameters from 1.6 to 6.7 μm were exposed to in vitro conditions at 37 °C in DMEM or dry for up to 6 months. During this period, the mechanical properties were assessed using cyclic mechanical loading, and material properties such as crystallinity and ester bond degradation were measured. No significant difference was found for any parameters between samples kept dry and in DMEM. The increase in crystallinity was linear with time, while the ester bond degradation showed an inverse logarithmic correlation with time. All samples showed an increase in modulus with exposure time for the first loading cycle. Modulus changes for the consecutive loading cycles showed a nonlinear relationship to the exposure time that depended on membrane type and maximum strain. In addition, the recovered elastic range showed an expected increase with the maximum strain reached. The mechanical response of electrospun membranes was compared to experimental tensile properties of the human annulus fibrosus tissue and an in silico model of the intervertebral disc. The modulus of the tested membranes was at the lower range of the values found in literature, while the elastically recoverable strain after preconditioning for all membrane types lies within the desired strain range for this application.

4.2: Introduction

Electrospun (ES) poly(ε-caprolactone) (PCL) is commonly used as a substrate providing mechanical support and guiding cellular activity in tissue engineering (TE) and regenerative medicine applications. ES networks can be produced with wide variety of fibre diameters and morphologies, depending on the production process. Thus, they can closely mimic the scale of structures and the fibrous morphology of natural soft tissues [147–149]. In vivo applications of such networks include, but are not limited to, cardiovascular systems [150–152], skin [153,154] and other collagen based tissues such as tendons, ligaments and the intervertebral discs (IVDs) [155,156]. In particular, ES membranes have been widely used to produce templates and membranes for tissue engineered IVDs [84,195]. In this context, understanding the functional requirements for such networks, the achievable mechanical properties and how these might change over time, when exposed to in vitro and in vivo TE environments, is required. The specific changes that the networks will undergo affect cellular activity [157–159] and how the membranes will resist deformation in a cyclic loading environment with high strains [160,161].

A significant amount of work has been done on the degradation of bulk PCL, both in vitro and in vivo. In vitro incubation for periods up to 30 weeks in water and hydroxyl radicals showed a linear reduction in molecular weight and a negligible increase in crystallinity of +2% [196]. Another study found no change in molecular weight after 27 weeks in water at 37 ºC and a similar increase in crystallinity [197]. The same study found a significant increase in stiffness after 14 weeks followed by a steady state. Patel et al. showed a similar increase in modulus after 4 weeks [47]. In vivo studies showed an inverse log rate dependent increase in crystallinity and log rate dependent decrease in molecular weight of capsules implanted in rats for up to 30 weeks [198] and rabbits up to

140 weeks [199]. A different study showed a linear increase in crystallinity and no significant change in molecular weight of thin extruded sub-millimetre PCL fibres in a rabbit model [197]. However, no mechanical tests were performed on the degraded PCL samples that were implanted in vivo due to difficulties associated with separating the living tissue and the sample post extraction. All studies concluded that implantation has no significant effect on the material degradation.

Electrospun PCL samples have been studied to a lesser extent. There are some key differences between the electrospun networks and bulk polymers. The surface to bulk ratio is much higher for the ES networks, as well as the nature of the production method, which imparts certain changes in the alignment of the amorphous regions and crystallites within the polymer fibres [164,168]. The consistency of the results depends largely on the quality and consistency of the networks. Therefore, the observations from different groups are varied. Duling et al. performed a systematic study on electrospun samples with exposure to water and elevated temperature, however the exposure was only up to 90 minutes [200]. Multiple studies have documented the lack of mass loss after up to 6 month exposure to aqueous solutions at 37 °C [201–203], although there are contradicting results whether the mass has indeed decreased [204]. The reduction in molecular weight due to degradation is also widely documented [205–207]. The linear modulus has been shown to generally increase with exposure time , although some studies have inconclusive results up to 3 month [203,205], [208].

Bolgen et al. showed an accelerated reduction in molecular weight in vivo in a rat model, relative to their in vitro study. These results were closely supported by Pektok et al. with membranes made up of fibres of 1.9 µm diameter implanted subcutaneously in a bovine model [206]. De Valence et al. showed an even faster reduction in molecular weight for vascular grafts with fibre diameter of 2.2 ± 0.6 µm in rats [209]. However, in vivo studies do not provide any mechanical measurement results due to soft tissue ingrowth.

Another aspect that needs to be studied in relation to the degradation of PCL membranes is how well these membranes match the native tissues that they are intended to replace, in terms of mechanical properties and their evolution over a relevant healing time. This is in fact tissue and application specific. One tissue engineering application of interest is the minimally invasive repair of annulus fissures in human IVDs. This application requires an enduring elastic character to be present in the material used for mechanical support, as well specific range of tensile and shear stiffness [82]. For the purpose of producing a conclusive set of mechanical data characterising the material properties of electrospun PCL membranes for potential use in this application, the aims of this study were threefold. First, to determine the mechanical behaviour of electrospun PCL membranes with a range of commonly used and biologically relevant fibre diameters. Second, to identify the relationship between the changes in mechanical behaviour and underlying material changes. Finally, to compare the measured mechanical response of these electrospun networks to the mechanical response of human annulus fibrosus tissue over a wide range of loading conditions. We hypothesize that the mechanical properties of the ES membranes will change with time as a result of material changes, and that the rate and nature of change will depend on the cross-sectional diameter of the fibres used in the membrane. Additionally, we hypothesize that the mechanical properties of ES membranes are persistently within the range of natural annulus fibrosus tissue.

4.3: Methods

4.3.1: Sample preparation and study design

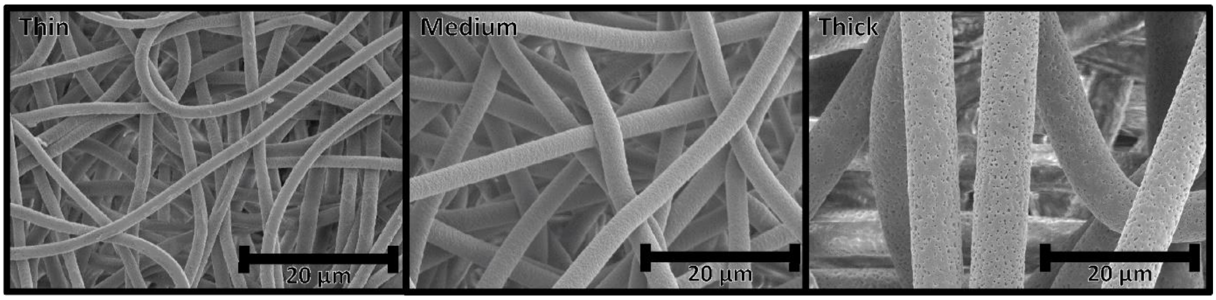

Figure 4-1: Representative micrographs of three different membranes types used in the study. Thin (a), medium (b) and thick (c).

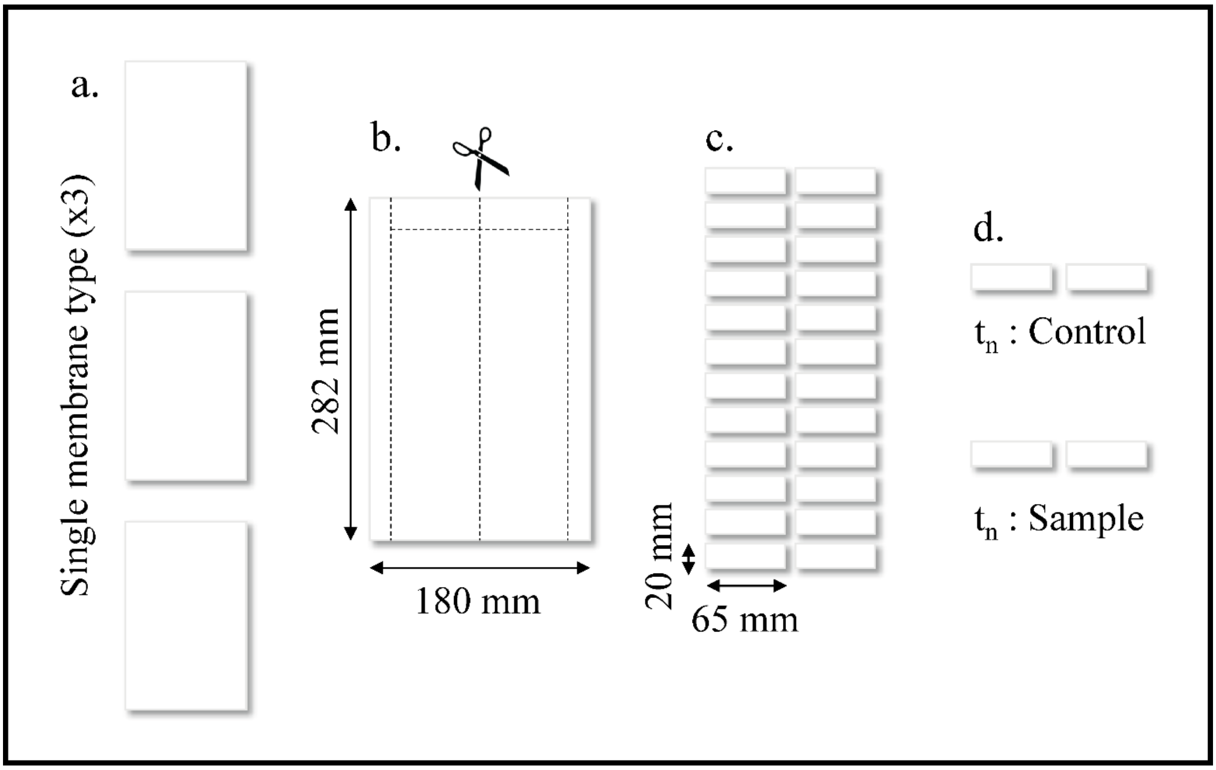

Figure 4-2: Sample preparation from electrospun mat to single samples. 3 membranes of the same type are produced (a). The membranes are cut into smaller pieces (b, c). The pieces are randomly separated into groups of 4 for each time point (tn), which are then split into sample and control group (d).

Three types of electrospun PCL (Mn 80’000 g/mol, Sigma Aldrich Chemistry, 440744) membranes of distinctly different fibre diameters were produced, as shown in Figure 4-1. The processing was done under variable electrospinning conditions reported in Table 4-1, using chloroform ($CHCl_3$, Sigma Aldrich, ReagentPlus, 132950) and methanol (CH_3OH, Fisher Chemicals, HPLC grade, CAS: 67-56-1) solvents. IME Technologies EC-CLI electrospinning equipment was used with a translation nozzle stage and an 8 cm diameter rotating drum collector rotating at 10 rpm, with a 19 cm spinning distance. The environmental parameters were controlled at 24 °C and 40 % relative humidity. The resultant mats were cut into pieces of 20 by 70 mm, which were randomly distributed among sample groups (Figure 4-2), where two randomly selected pieces were treated as a single sample for all tests.

Table 4-1: Electrospinning parameters for three fibre diameters used in the study.

Fibre diameter [μm]± SD	PCL [wt. %]	Solution and solvent ratio	Needle inner diameter [mm]	V source [kV]	V collector [kV]	Flowrate [μl/min]
1.60 ± 0.26 (thin)	12	1:6 $CHCl_3$:CH_3OH	0.6	16	-1	27
3.31 ± 0.21 (medium)	12	1:7.3 $CHCl_3$:CH_3OH	0.8	24	-2	26
6.73 ± 0.51 (thick)	12	$CHCl_3$	0.8	24	-2	26

The membranes were dried in a desiccator under vacuum for 12 hours, then sterilized in 70 % alcohol solution for 1 hour followed by drying in a sterile environment for an additional hour. Samples were then separated into 2 groups with 3 pieces per group: controls which were kept dry and the sample group which was washed two times with PBS (SIGMA Life Science, pH 7.4) before being submerged in 50 ml of DMEM (DMEM (1x) + GlutaMAX-I [+] 4.5g/L D-Glucose [+] Pyruvate, Gibco by Life Technology) with 1% penicillin-streptomycin (Gibco, Zug, Switzerland) and 10% Fetal Calf Serum (FCS). All samples were kept at 37 °C. The solution was continuously agitated and changed every 2 weeks. Six time points (0, 14, 30, 60, 90 and 180 days) were chosen, at which each sample was washed with PBS, dried and underwent mechanical and material testing.

4.3.2: Mechanical testing

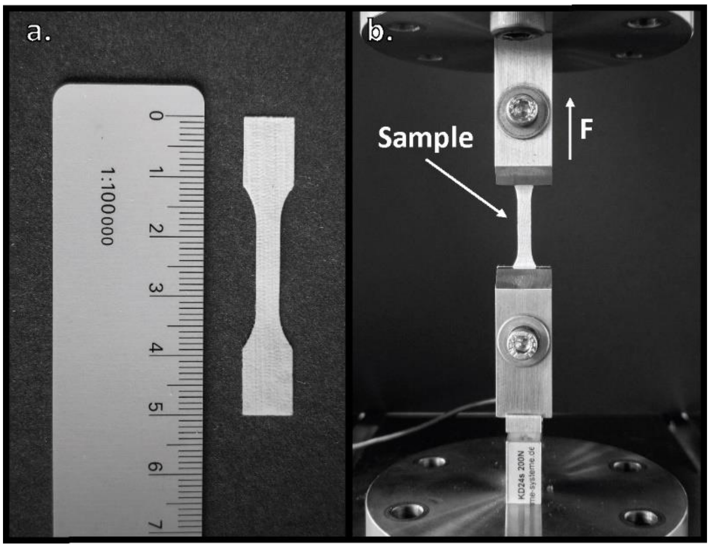

Figure 4-3: Representative dogbone sample (a), mechanical testing rig and dogbone sample placed in the rig (b).

Three dogbone-shaped specimens were punched from each sample, producing 9 specimens per membrane type per time point in each control and sample group. The samples were washed and dried prior to testing. The length of the specimen between the clamps was 12 mm (Figure 4-3). These underwent cyclic extension mechanical testing at a strain rate of 0.5 mm/s (4.2 strain %/s) with 4 cycles at each of the 6 strain steps, each step increasing by 5 percent (5, 10, 15, 20, 25 and 30 % strain). In the final step the membranes were loaded to 150 % strain in a single cycle. Engineering stress was calculated from force divided by linear density: $\sigma = F/(wm/A\rho)$, where F is force, w is width of the dogbone (2 mm), m is mass of the dogbone, A is the area of a face of the dogbone (138 mm^2) and ρ is density of PCL (0.001145 g/mm^3). To calculate the traditional stress values (force over cross section area) the linear density was divided by porosity fraction of the sample. The porosity values were obtained using dimensional measurements of the samples in the undamaged state combined with the known density of PCL. The thickness of the membrane samples was determined using thickness gauge (Käfer Messuhren, Villingen-Schwenningen, Germany) at a standardized contact pressure of 7.85 kPa (1 N, Ø 10 mm) and with an accuracy of

0.01 mm. Additional parameters such as hysteresis and recovery were also calculated. Hysteresis was calculated as the area under the unloading curve subtracted from the area under the loading curve. The recovery was defined as a strain value between the maximum strain reached in the cycle and when the unloading cycle stress reaches 0 value, at which point the membrane would become slack. All tests were performed in an ambient lab environment, dry at 24ºC.

4.3.3: Material testing

Dynamic scanning calorimetry (DSC) was performed using a differential scanning calorimeter (DSC 822, Mettler Toledo) with samples exposed to a temperature range from -40 to 100 °C with a heating and cooling rate of 10 °C/min. The crystallinity change of PCL was determined by comparing the enthalpy of fusion to that of 100% crystalline PCL (139.5 J/g) [174]. Attenuated total reflectance (ZnSe crystal) - Fourier transform infrared spectroscopy (ATR-FTIR) was performed using a Vertex 70 (Burker Optik GmbH) machine. The spectrum measured was between 500 and 4000 cm^{-1} with 64 scans. To evaluate the data, it was assumed that carbon-hydrogen bonds (CH) do not degrade, following, changes in ester bond (C=O) and carboxylic acid bond (COC) peaks were evaluated by the ratio of each to C=O bonds. 3 samples per membrane type per time point were tested with these methods.

Reference SEM images were acquired using a Hitachi SU5000 scanning electron microscope to evaluate the visual appearance and change in fibre diameter of the incubated membranes. The images were taken from unused parts (i.e., non-tested) of the incubated sample at each time point.

4.3.4: Finite element analysis

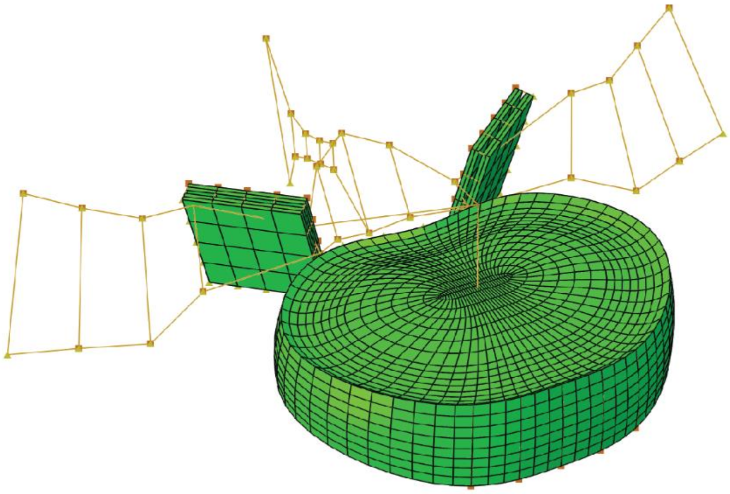

Figure 4-4: A Parameterized FE model of a L4-L5 intervertebral disc. Nine different vertebrae geometries were investigated in the study of Helgason et al. [210]*. The vertebra body size was varied from -1.5 to +1.5 standard deviations (SD) from the average geometry reported by Panjabi et al.* [211]*. The disc height and lordotic angle were varied from -1.0 to +1.5 standard deviations from the average of the values reported by Abuzayed et al.* [212] *the study of Rohlmann et al.* [213].

To provide context to the mechanical properties for annulus repair membranes, we used the results from a finite element (FE) analysis reported in a previous study [210], in order to identify the distribution of local strain values for annular tissue during simulated physiological loading of the segment. The parametrized FE model used in the study and the outcomes of that study are only briefly described here for clarity and context (Figure 4-4). An X-ray computed tomography scan of a pair of L4-L5 vertebrae was used to define a generic intervertebral disc shape. These vertebrae were found to be representative of average human anatomy at this level in the spine [211]. The vertebrae were modelled as rigid structures and the facet joints were simplified by two parallel plain surfaces that represent the cartilage layers. The outer shape of the disc was parametrized including the lordotic angle, disc height, endplate shape and disc bulge. The ratio of nucleus area vs. disc area (0.43) was defined according to literature [214]. The nucleus was modelled as an incompressible fluid filled volume. Annulus fibre orientation, which was alternated in each annulus layer, was set to +/- 30˚ from a horizontal plane. The annulus matrix was implemented as a Neo-Hookean material in accordance with the study of Rohlmann et al.[213], with: C10 = 0.3448 and D1 = 0.3. The fibre reinforcement was defined following the study of Markert et al.[215], with the coefficient $\mu = 0.1073$ and $\gamma = 25.8129$ taken from the study of Studer et al.[127]. The material behaviour was implemented as a user subroutine (UMAT) in ABAQUS. Through parametrization of the FE model, new instances of the model were generated by systematically varying the disc height, lordotic angle and vertebral body size. The disc height and lordotic angle were varied from -1xSD to +1.5xSD. The vertebral body size (and thus disc size) was varied from -1xSD to +1.5xSD. The FE models were subjected to a range of loading conditions with up to 7.5 Nm being applied in flexion, extension, lateral bending, and torsion respectively. For all loading cases a compressive follower load of 1000 N was applied.

4.3.5: Data post processing and statistics

To evaluate the significance of the effect of fibre diameter and time on the modulus measured on the first loading cycle a two-way ANOVA was conducted. As the interaction between the factors was found to be significant, simple effects analysis was performed by splitting the samples by thickness and performing a one-way ANOVA with Turkey's HSD post-hoc analysis to evaluate the differences between different time points. The analysis was performed in IBM SPSS v26.

To investigate the change in hysteresis and crystalline fraction over time and the effect of strain on modulus measured on the 4th loading cycle linear regression was fitted to the results. Linearity was established by visual inspection of a scatterplot. There was homoscedasticity, as assessed by visual inspection of a plot of standardized residuals versus standardized predicted values. Residuals were normally distributed as assessed by visual inspection of a normal probability plot. The analysis was performed in IBM SPSS v26.

To evaluate the change in ester bond density over time and the elastically recoverable strain with respect to maximum strain, a one phase decay model was used with the following equation: $Y = (Y_0 - Plateau) * exp(-K * X) + Plateau$, where Y is modulus or ester bond density and X is maximum strain level or time, respectively.

The outcome of the mechanical testing was qualitatively compared to the range principal strains from the FE analysis. To achieve this, the tensile principal stress-strain response was sampled for all nodes on the outer surface of the annulus in the FEMs, where an electro-spun PCL membrane would be applied as a part of a repair procedure. This was done in steps of 20, 40, 60, 80 and 100% of the max loading, for all the FE model geometries and loading cases simulated. These results should conceptually represent the range of appropriate candidate implant material strains for annulus surface repair.

4.4: Results

4.4.1: Morphology

Three types of membranes were produced for this study with three different sets of electrospinning parameters. These membranes differed significantly primarily in their fibre diameter, as measured through electron microscopy (Figure 4-1). The SEM micrographs were taken at each time point and the membranes did not show any change in fibre diameter with incubation time. No changes in the appearance of the fibres and inter fibre bonds were observed at any time point. Additionally, fibres submerged in medium and kept dry showed no differences.

4.4.2: Mechanical testing

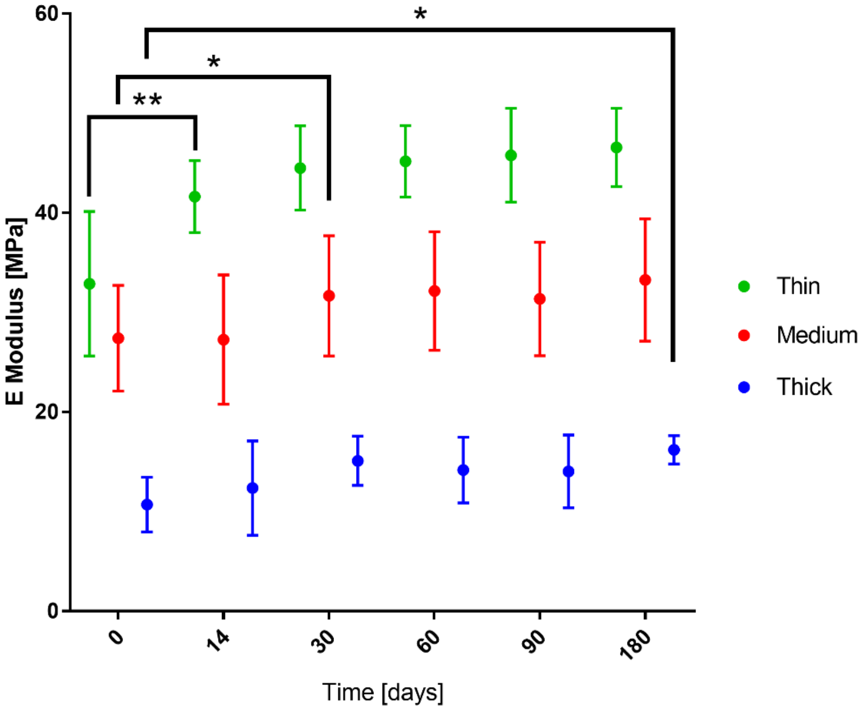

*Figure 4-5: The effect of incubation time on Young's modulus of the first loading cycle of 3 types of samples. n = 9, * p < 0.05, ** p < 0.005. n = 18*

Young's modulus measured at each time point for both dry and submerged samples showed an increase over time for all membranes. No significant difference between the data from dry and submerged membranes could be detected. Therefore, the results shown in Figure 4-5 are only for the submerged samples. A large and significant difference in modulus was observed between membranes made up of fibres of different diameters, where thinner fibres showed higher modulus, as seen in Figure 4-5. For samples with thin fibres at 1.60 ± 0.26 µm fibre thickness, modulus was 32.80 ± 6.43 MPa, medium samples with fibre thickness of 3.31 ± 0.21 µm had a modulus of 24.71 ± 2.74 MPa and for samples with thick fibres of 6.73 ±0.51 µm diameter, and the modulus was 10.55 ± 2.58 MPa. However, there was a statistically significant interaction between the effects of fibre diameter and time on modulus, F (10, 306) = 1.859, p = 0.05. Leading to the conclusion that the incubation time affects fibres of different thickness differently. Simple main effects analysis showed that the effect of time is significant for the three fibre diameters. Specifically, for the thin fibres (1.6 µm) F (5, 102) = 12.190, p = 0.000; the medium fibre diameter (3.31 µm) F (5, 102) = 6.885, p = 0.000; and thick fibre diameter (6.73 µm) F (5, 102) = 8.223, p = 0.000. Furthermore, it was found the onset of the significant change in modulus was at a different time point. The samples made up of the thinnest fibres showed a significant increase (41 %) after 14 days with no further changes, the medium fibre diameter samples showing an increase (34 %) after 30 days, and the thickest fibre diameter samples showing an increase (43 %) after 90 days only. In addition, the thickest fibre diameter samples showed another change after 180 days, which was significantly higher from 0, 14, 30 and 60 days.

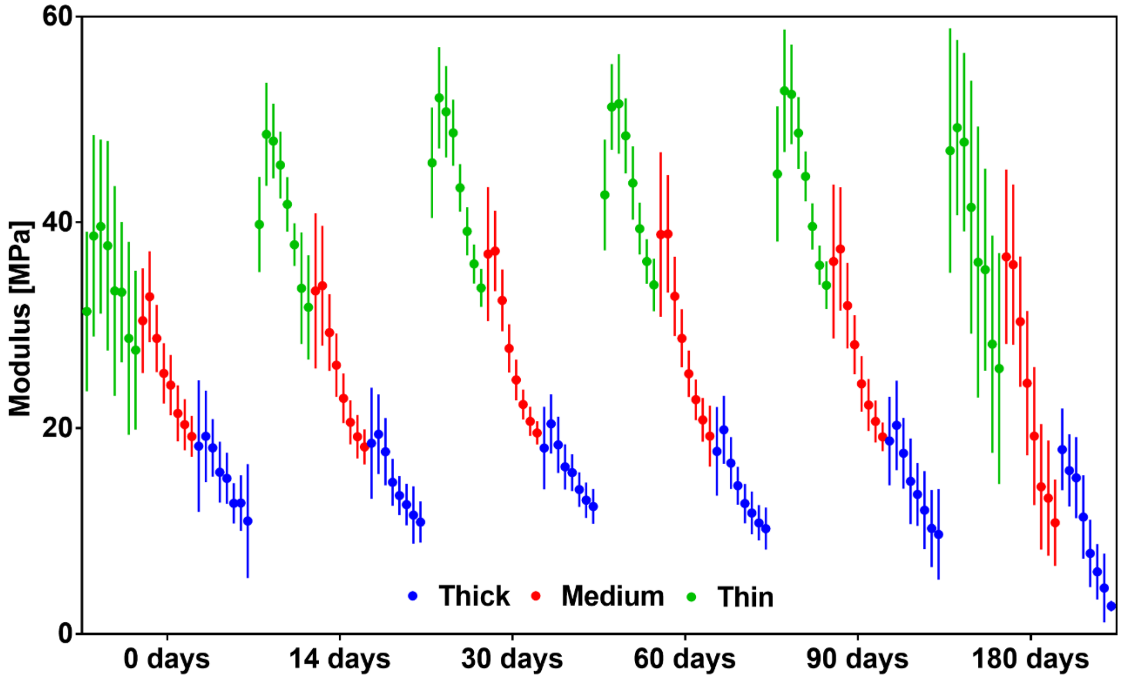

Figure 4-6: Graph showing change of Young's modulus. Seven consecutive 5% strain steps from 5% strain are shown grouped by membrane type at each time point. n = 18

The modulus measured on the 4th loading cycle was assessed relative to the maximum strain reached during the cycle and grouped with respect to the membrane type and time, as shown in Figure 4-6. The data is presented in seven strain steps from 5 % to 35 % and constant step size of 5 %, grouped by membrane and time point. The results for the inverse correlation that was established for modulus with respect to strain step are summarized in Table 4-2. The magnitude of the inter-strain reduction increased with time for all types of membranes, the change was larger for membranes made up of thinner fibres. The magnitude of the effect the strain had on modulus is characterized by the R2 and R2adj values in Table 4-2 show overall a medium to large effect [216], with the exception of day 0 of the membrane made up of thin fibres where there was a small effect. Furthermore, the intercept which represents a theoretical zero damage modulus for the membranes increased over time for the 2 membranes made up of thinner fibres (1.6 µm and 3.31 µm), while staying unchanged up to 180 days for the membrane made up of thickest fibres (6.73 µm).

Thin

Day	0	14	30	60	90	180	mean
Slope	-.335	-.442	-.540	-.551	-.581	-.727	-.529
Slope (95% CI)	(-.500, -.171)	(-.567, -.408)	(-.604, -.486)	(-.625, -.477)	(-.654, -.526)	(-.961, -.576)	
Intercept	38.857	48.571	52.465	53.180	53.826	50.342	49.540
Intercept (95% CI)	(35.173, 42.54)	(47.330, 50.895)	(51.321, 53.969)	(51.528, 54.832)	(52.672, 55.517)	(46.141, 54.544)	
R2, R2adj	.116, .109	.607, .604	.770, .768	.637, .634	.739, .737	.325, .319	0.532, 0.529

Medium

Day	0	14	30	60	90	180	mean
Slope	-.374	-.536	-.567	-.625	-.597	-.909	-.601
Slope (95% CI)	(-.470, -.341)	(-.621, -.483)	(-.636, -.528)	(-.691, -.559)	(-.665, -.528)	(-1.028, -.791)	
Intercept	32.709	35.380	37.487	39.166	37.761	38.024	36.755
Intercept (95% CI)	(31.271, 34.148)	(33.836, 36.924)	(36.286, 38.687)	(37.682, 40.650)	(36.231, 39.292)	(35.380, 40.668)	
R2, R2adj	.561, .557	.673, .670	.801, .800	.737, .735	.706, .704	.651, .649	0.688, 0.686

Thick

Day	0	14	30	60	90	180	mean
Slope	-.278	-.300	-.267	-.296	-.341	-.389	-.312
Slope (95% CI)	(-.318, -.207)	(-.356, -.248)	(-.321, -.234)	(-.374, -.268)	(-.414, -.268)	(-.483, -.348)	
Intercept	20.192	20.246	20.950	20.309	20.393	16.626	19.786
Intercept (95% CI)	(18.956, 21.429)	(19.033, 21.459)	(19.980, 21.921)	(19.131, 21.486)	(18.767, 22.020)	(15.115, 18.136)	
R2, R2adj	.485, .480	.541, .537	.564, .561	.544, .540	.409, .405	.562, .558	0.518, 0.514

Table 4-2: Summary of the results obtained from fitting linear regression model to assess the effect of maximum strain on modulus measured on the 4th loading cycle. The model fitting was significant for all groups with $p < .0005$, $n = 18$.

The hysteresis between the loading and unloading energy was calculated for the 1st loading cycle of each strain step and time point for the three sample groups, as seen in Figure 4-7. Seven strain steps from 5 % to 35 % at a constant step size of 5% are shown. Values were normalized to time point 0 at the corresponding strain steps. Here once again the submerged sample group and the dry samples did not show a significant difference. Since material properties were also consistent for both groups, the results were pooled. Fibre diameter and time both had a significant impact on the hysteresis. Membranes made up of fibres of different diameters showed significantly different hysteresis. All membranes showed a significantly lower hysteresis after 180 days. The change in hysteresis with respect to the maximum strain was not significant for thin samples, while medium and thick samples showed a significant correlation.

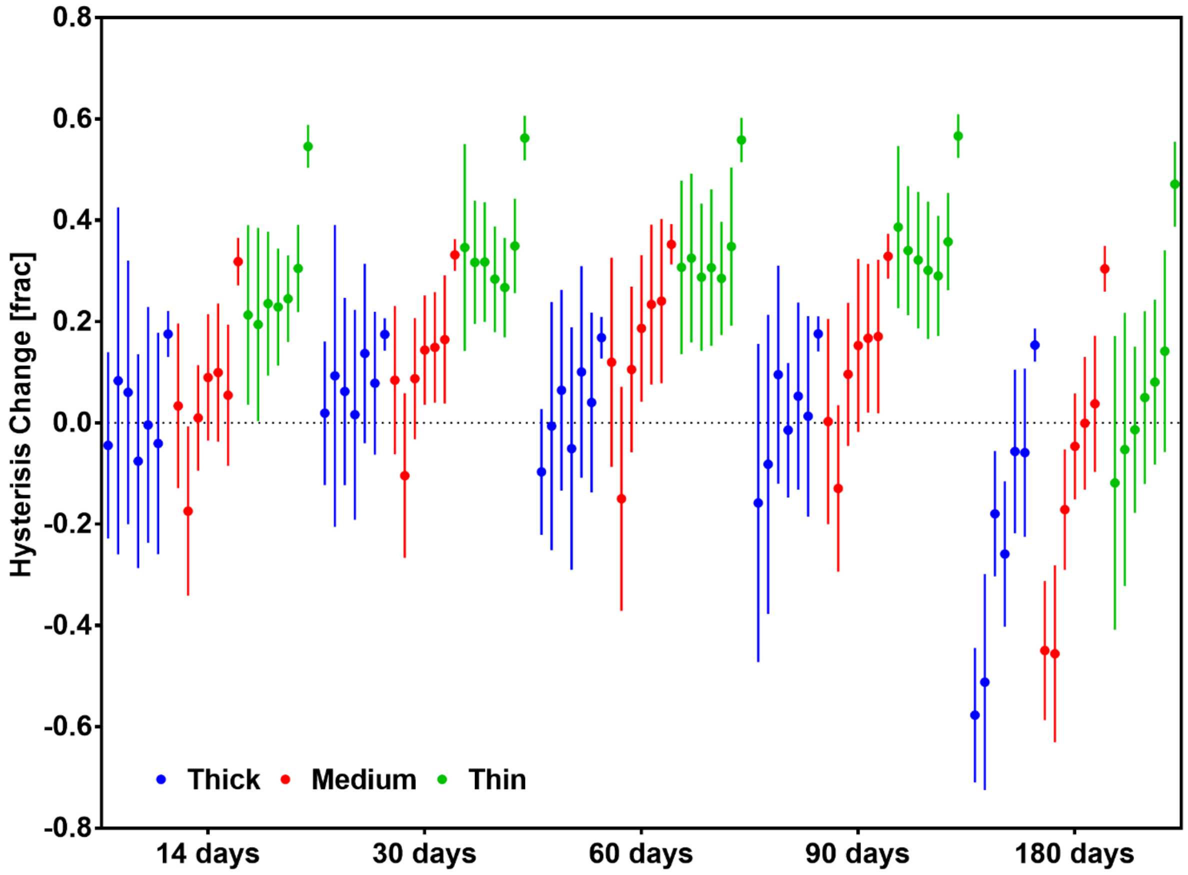

Figure 4-7: Graph showing change of hysteresis normalized 0 time point. Seven consecutive 5% strain steps are shown grouped by membrane type at each time point. Time showed a significant effect on the change in hysteresis for all samples ($p < 0.05$). Fibre diameter shows a strongly significant effect on this change ($p < 0.0005$), as well as the strain level for the Medium ($p < 0.05$) and Thick sample ($p < 0.05$). $n = 9$

Similarly, to Figure 4-6 and 7, in Figure 4-8 the results for elastically recovered strain were grouped with respect to membrane type and time, as well as seven strain steps from 5 % to 35 % and constant step size of 5 % are shown in each group. At 5 % maximum strain the elastic range was not significantly different from the maximum strain. Above 5 % the recovery was consistently lower than the maximum strain reached with an increasing fractional decrease. The elastically recoverable strain over the whole testing period with preconditioning to 35 % strain was 22.19 % ± 1.320 SD for samples made up of thin fibres (1.6 µm), 22.48 % ± 1.397 SD for medium (3.31 µm) fibres and 19.6 % ± 1.9 SD for the thick (6.73 µm). Recovery against maximum strain was evaluated using a one phase decay function at each time point individually, shown in Figure 4-9. This evaluation produced two values K and Plateau. The Plateau value shows the maximum recovery that can be reached by the sample and how it changes with incubation type. The K value shows how quickly the recovery plateau is reached with respect to maximum strain. The membranes were tested up to 150% strain without failure in all membrane types and all time-points in this study.

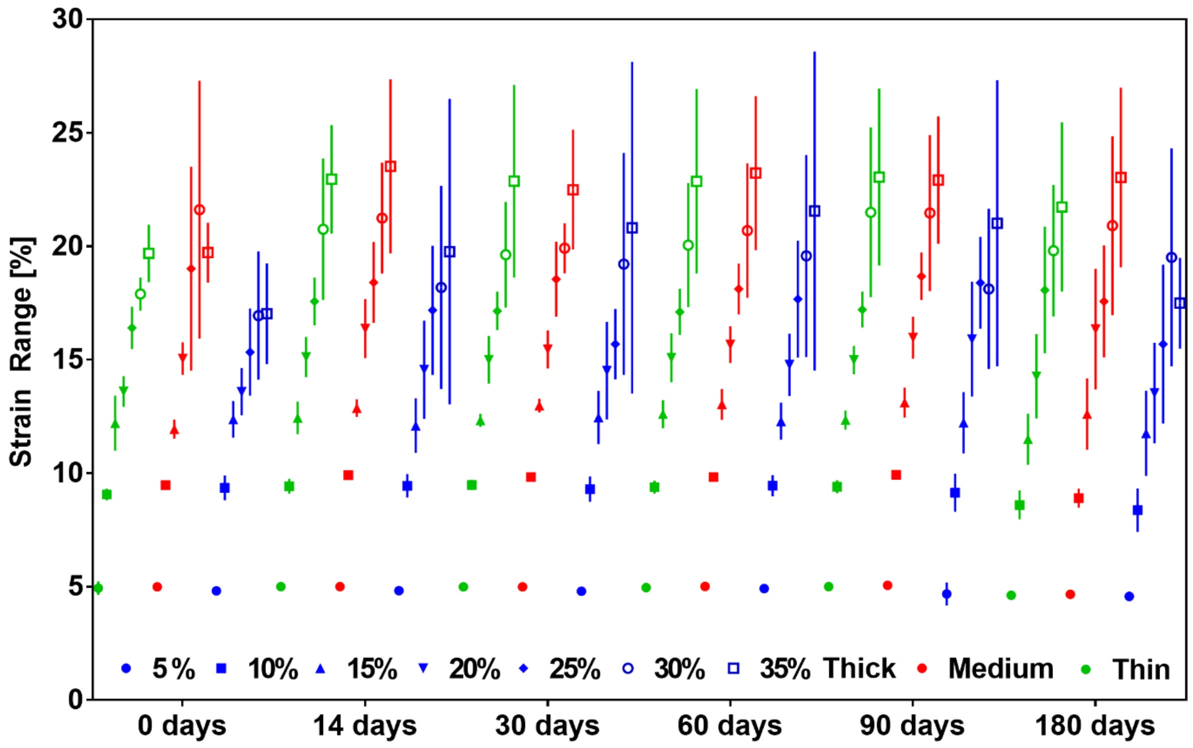

Figure 4-8: Graph showing change in elastically recovered strain in % strain calculated at consecutive 5% maximum strain steps grouped by membrane type at each time point. n = 18

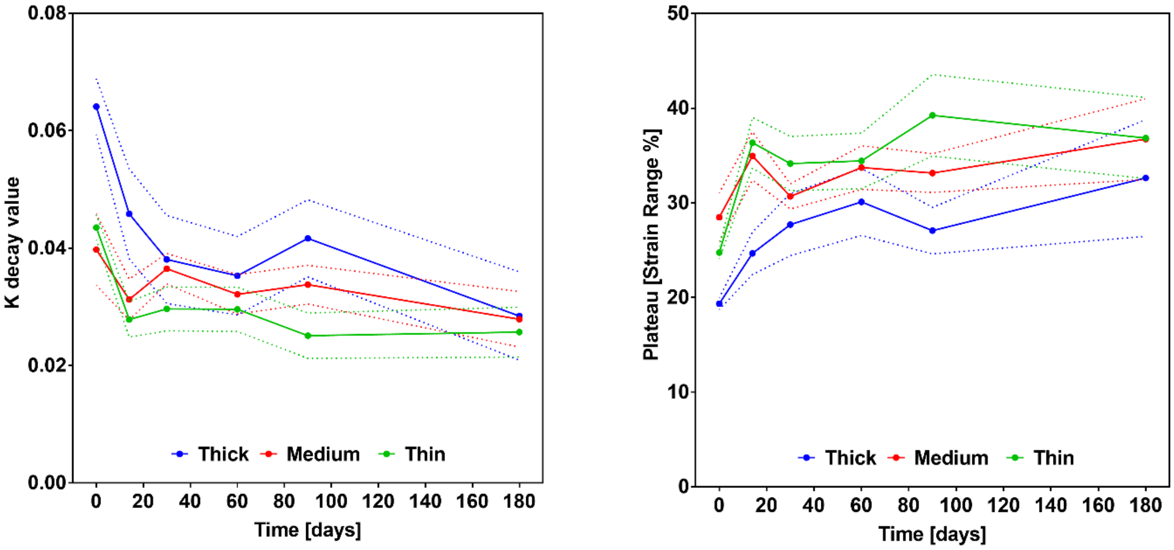

Figure 4-9: K (a) and Plateau (b) values for the one phase decay fitted to recovery against maximum strain data grouped by time point and membrane type. n = 5

4.4.3: Finite element model

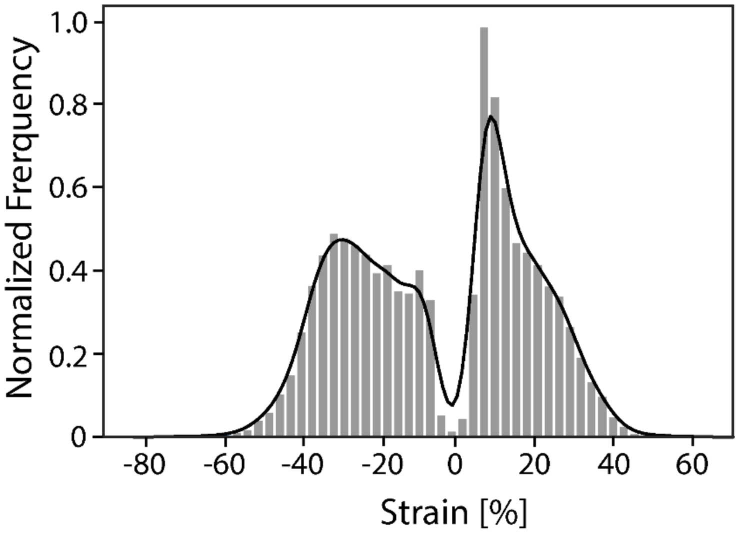

Figure 4-10: Graph showing normalized frequency of strains predicted by the FE model.

In this study the strain environment of human IVDs under severe loading was assessed across a wide spectrum of human IVD anatomies, and it was found based on the frequency plots that a small portion of the IVD may experience local tensile surface strains that are about or slightly above 40%. The frequency of strains recorded in annulus tissue according to the FEM results is illustrated in Figure 4-10 to provided context for the resilience requirements on the electrospun membranes for AF repair.

4.4.4: Material testing

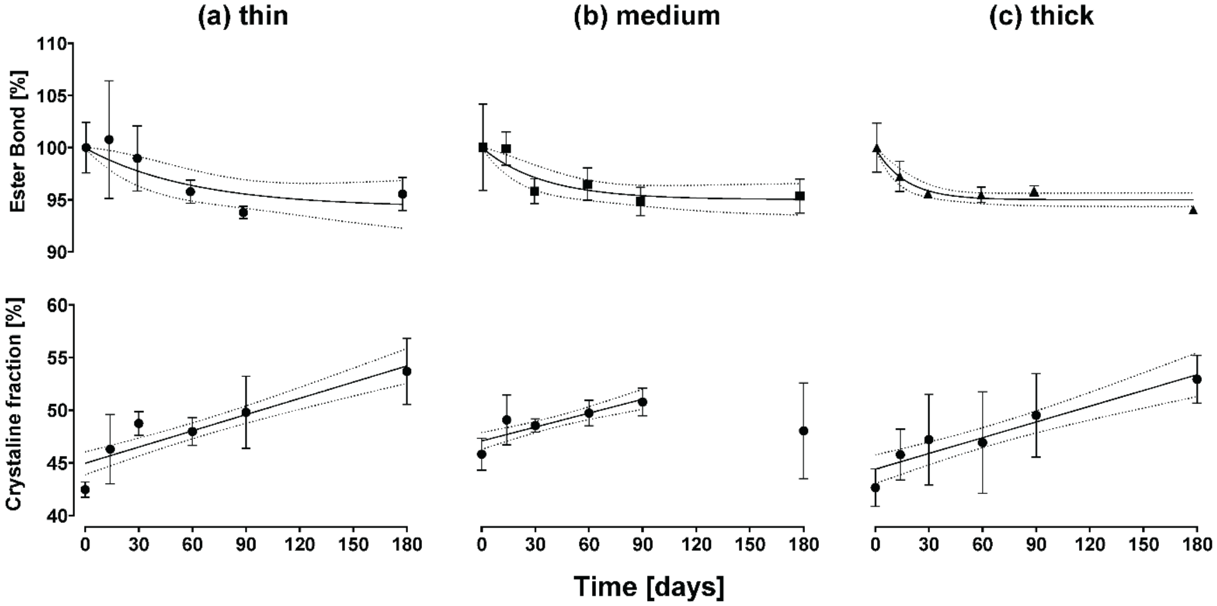

Figure 4-11: Change of ester bond density against time grouped by sample type (a) membrane made up of thin fibre (1.6 µm), (b) medium fibres (3.31 µm) and thick fibres (6.73 µm). Crystalline fraction is represented with respect to time and grouped by the same sample types.

The change of ester bond is reported as a fraction of C-C bonds. Figure 4-11 shows the change of ester bond fraction over time for the three different membranes, normalized to time point 0. A significant decrease in relative ester bond density is indicative of hydrolytic degradation of PCL, which would lead to shortening of polymer chains. No difference was found between the submerged samples and those kept dry; therefore, the results presented are only for the submerged samples. A one phase decay function was fitted to the data. It was found that the decay exponential K (mean ± standard error) increased with increasing fibre thickness of the membrane: 0.016 (±0.011) for thin fibres, 0.028 (±0.013) for medium and 0.058 (±0.015) for thick fibres.

The crystalline fraction increased in membranes of all three types from approximately 42 – 45 % to 50 – 55 %. The submerged group did not have a significantly different result from the dry group, therefore the result only shown for the submerged samples in Figure 4-11. The three types of membranes were not significantly different from each other in crystalline fraction or recrystallization rate. A linear regression model was fit to the crystalline fraction over time data. The model showed a significant fit for all three types of membranes with a strong to medium effect of time on crystalline fraction [216] summarized in Table 4-3.

Table 4-3: Summary of linear regression model fitted to the crystallinity over time data for three types of membranes used in the study. n = 34

Fibre diameter [μm] ± SD	Intercept [% Crystallinity]	Slope [% Crystallinity.day^{-1}]	R^2, R^2_{adj}	Model	p
1.60 ± 0.26 (thin)	45.3	0.718	0.516, 0.501	F (1,32)=34.126	< 0.0005
3.31 ± 0.21 (medium)	47.1	0.634	0.402, 0.381	F (1,28)=18.819	< 0.0005
6.73 ± 0.51 (thick)	44.3	0.635	0.404, 0.385	F (1,32)=21.671	< 0.0005

4.5: Discussion

In the scope of intervertebral disc repair using electrospun membranes as a mechanical support, this study aimed to establish the influence of fibre diameter on the mechanical and material properties of electrospun membranes not only directly after production but also following extended exposure to conditions similar to those found in vivo. No statistically significant difference between membranes kept in solution and membranes kept dry over the whole period were found for any of the investigated parameters. Therefore, only the results for those samples kept in solution are discussed. Finally, the membrane functional limits were found to fall within the range of the targeted strain range of annulus fibrous tissue under physiological loading as assessed by comparison with computational model.

The choice of solution and electrospinning parameters in this study was based on a common parameter set, widely used to produce membranes for in vivo and in vitro applications [217]. These membranes can be easily sterilized using a variety of methods, while the methanol and chloroform solvent has been shown to completely evaporate after vacuum treatment and be nontoxic [218]. As these membranes are intended for in vivo applications, fibre diameters chosen for this study were based on the range deemed useful in such applications. Considerations such as cell proliferation, infiltration and nutrient delivery are of utmost importance for cell viability, and require porosity size on the scale of micrometre [165], which is in turn largely dependent on fibre diameter especially in the plane orthogonal to the spinning direction.

4.5.1: Evolution of mechanical properties

Direct assessment of the mechanical properties post long term (> 1 week) in vivo implantation is not possible due to integration of soft tissue [206,209], therefore the study was carried out in vitro. The appearance of membranes as well as material properties were evaluated at each time point up to 6 months (180 days). The mechanical properties were assessed through cyclic tensile loading. Degradation has been shown to proceed though hydrolytic cleavage of ester bonds in PCL [196,199], consequently dry state at 37 °C was chosen as control for the study.

In this study fibre diameter and morphology were observed using SEM and showed no change throughout the incubation period. There is a consensus in literature that PCL does not show mass loss and dimensional changes when exposed to aqueous solutions such as PBS at 37 °C for up to 6 months. A study by Lam et al. showed no morphological differences were observed after exposure up to 6 months, due to very low mass loss on the order of 1 % that was observed [197]. No changes in fibre diameter were also observed by Li et al. after 2 month [219]. Insignificant mass loss was also observed by multiple other studies in PBS over a period of 7 days to 2 month [201,202,220,221]. In addition depending on the medium that the membranes are kept in the mass can even increase, as was shown in plasma by Johnson et al. [208].

The density of PCL for the purpose of calculating modulus for comparison with literature was assumed to have been unchanged throughout the experiment, this assumption is supported by only minor degradation observed in the samples. The porosity and dimensional changes were observed and quantified throughout the experiment at each time point and have shown no variation at all.

The tensile linear modulus of the membranes was in the range of other studies that performed uniaxial tensile tests. For mats made up of thin (1.60 µm) fibres, the modulus when accounted for porosity was 6.57 to 9.32 MPa though out the 6 month period, which the range found in literature of 8.5 – 17.5 MPa [47,219,222–226] for fibres of broadly similar diameter. For mats made up of medium (3.31 µm) Kim et al. measured 7.6 ± 0.7 MPa on fibres 3.43 ± 0.57 µm [225], compared to 4.93 ± 0.95 MPa measured in this study. No definitive data is available in literature on electrospun PCL fibres in the order of the thick (6.73 µm) fibres used in this study. However, the 1.6 ± 0.41 MPa modulus adjusted for porosity in this study is well in line with the trend from the measurements from the thinner fibres. Overall, the values of linear tensile modulus for electrospun PCL membranes in this study fall within in the lower range from the values previously described in literature.

The modulus of the membranes increased with time when measured only on the first loading cycle; however, the significant change occurred later for membranes made up of fibres of higher diameter. This finding is consistent with previous studies [197,205], which also showed an increase in modulus when exposed to elevated temperatures in PBS and DMEM, theorized to be due to annealing leading to an increase in crystallinity. However, the variation in the onset of the change in the modulus is not directly correlated with the change in crystallinity in this study, as the rate of increase of crystallinity was rather linear and not significantly different between different fibre diameters. When the membranes were exposed to repeated strains in the region where plastic losses were significant (above 5%), there was an overall decrease in modulus linearly correlated with increase in strain, due to damage incurred in the previous cycles. This finding is supported by previous studies [200], where the likely explanation is breakage of weak inter-fibre bonds, which lead to softening. Evidently this damage is not significant up to 5 % strain as the modulus increased after loading up to 5 % due to work hardening. The rate of modulus decreases with increasing strain above 5 % increased with incubation time. This phenomenon can be explained by the increase in crystalline fraction and degradation of the polymer over time, which leads to the material being more prone to damage at lower strains. This consideration is paramount for adequate design of the electrospun PCL implants in the scope of biomedical applications with load bearing capability.

The difference in energy of the loading curve and the unloading curve (i.e., hysteresis) was quantified on the first loading cycle at each strain level (Figure 4-7). However, the mechanism by which the change in hysteresis occurs was not analysed in detail in this study as the complex network and material interactions require a focused set of experiments and models aimed at understanding the combination of plastic and visco-elastic behaviour of the samples, which is beyond the scope of this study. Other studies have suggested fibre reorientation as the source of hysteresis [208]. This mechanism could explain the increase in hysteresis with increasing maximum strain, as fibres need to move more to accommodate the deformation. As well as the overall decrease with incubation time, as the material becomes stiffer the capacity for non-destructive fibre motion decreases.

Recovery, defined as a reproducible range at which the membrane exhibits an elastic response, was measured at each maximum strain step. The elastic response of the material can be modified through preconditioning steps, as evidenced by the results in this study where it can be observed that the recovery increased significantly with increasing maximum strain reached on the first loading cycle. The first loading cycle can also be considered a preconditioning step that would eliminate the need to account for the slack in the membrane after the plastic deformation. The increase in elastic range with increasing preloading strain can be explained by plastic deformation of the underlying fibres and breakage of the inter-fibre linkages, which leads reduction in fibre interconnection density and consequent loosening of the network allowing for strain without plastic loss, this finding is supported by observations by Duling et al. [200]. Although PCL has a significant plastic character, as was hypothesized a useful elastic range can be accessed through this practice. In addition, the mechanical response is similar to that of natural collagen matrix, as it stems from a similar fibre realignment mechanism [227].

4.5.2: Degradation of the electrospun membranes

The change in material properties observed during the exposure of the membranes to DMEM at 37 °C was quantified using DSC measurements and IR-Spectroscopy. These measurements provided two main values: crystalline fraction and ester bond density respectively. Crystalline fraction did not differ significantly between samples made up of fibres of different diameter. Comparing this to literature is difficult as we are not aware of any studies that measured this directly on samples produced with similar methods and in this fibre diameter range for PCL. The crystalline fraction increased linearly as a function of time at elevated temperature as seen from Figure 4-11. This is consistent with previous findings in vivo extruded thin PCL fibres as well as other semi-crystalline electrospun polymers and is due to annealing that is accelerated at temperatures close to glass transition [197,228].

The ester bond density was used to assess the degradation of PCL through ester bond cleavage and establish the rate of this process. The degradation of bulk PCL has been theorized by Sun et al. to proceed through random chain scission in vitro, as the rate of molecular weight decrease with time was independent of geometry and aqueous solution constituents in vitro [199]. Lam et al. [197] did not support this view since the implied bulk autocatalytic cleavage of ester bonds should show an increase in degradation rate over time, which was not observed in their study. This can be explained by vastly different geometry of the implanted samples of the two studies, where the earlier study used bulk samples while the later thin fibres. Lack of bulk autocatalytic process is consistent with the findings of this study, where the fibres are still a magnitude thinner than those used by Lam et al. The reduction in ester bonds showed an exponential decay behaviour with a characteristic slowdown in the degradation after a certain time period. The rate of decay (*k*) showed a positive linear correlation with the fibre diameter. This finding implies surface area-controlled process, as when the easily accessible surface region is degraded, the bond cleavage that relies on hydration, proceeds at much slower pace in the bulk. Hence, thick fibres reached the plateau degradation state much quicker than thin fibres that have much more surface relative to bulk.

A direct linear relationship between modulus and crystalline fraction has been observed experimentally in electrospun single fibres of similar semi-crystalline polymers [191] as well as theoretically [229]. In this study, while the crystalline fraction increased linearly with time, modulus did not show the same relationship. This can be due to degradation, characterized here as change in ester bond density which leads to the reduction of the molecular weight of the polymer. It is expected that on the material level the effect on modulus from change in molecular weight would be small, while the largest effect is on strain at break, which decreases with decreasing molecular weight based on research done on semi-crystalline polymers [230]. The mismatch between the expected change in material properties and observations on electrospun networks arise from the complex fibre-fibre interactions which play a key role during fibre reorientation under stress [83,191]. In particular, inter-fibre adhesion, which plays one of the key roles [189], is affected by reduction in elongation at break as well as stiffening of material. It is therefore likely that the non-linear relationship between network modulus and incubation time is a result of interplay between the increasing modulus of the fibres and decreasing resilience of the inter-fibre bonds. This is qualitatively supported by the increasing difference between the hysteresis at low strains and high strains with time. The hysteresis in this study represents plastic energy loss after the first loading cycle. It suggests that at low strains, where the effect of inter-fibre interactions is low the networks were less prone to plastic deformation, while at high strains this was not the case due to weakening of the inter-fibre bonds. Paralleling this observation, the magnitude of the inter-strain reduction in modulus with increasing strain increased with time for all types of membranes. This is likely due to the same effect imparted by the failure of inter-fibre links, which provide a reinforcing effect on the network [83]. The breakage occurs more easily at later time points; therefore, the modulus reduction is higher. The complexity of the interaction of the effects of material parameters coupled with the network behaviour under stress puts a constitutive mathematical model outside the scope of this study. In conclusion, it was found that to arrive at a more conclusive relationship between the parameters discussed, microscopic 3-dimensional observation of the network deformation is required to distinguish the contribution of the changes in the material properties to the individual fibre segments and fiber-fiber interactions. A simplified empirical regression model did not lead to statically significant interaction of the crystalline fraction, ester bond density and modulus of the membranes.

4.5.3: Mechanical properties in the context of AF repair

4.5.3.1: Electrospun membranes compared to AF tissue level response

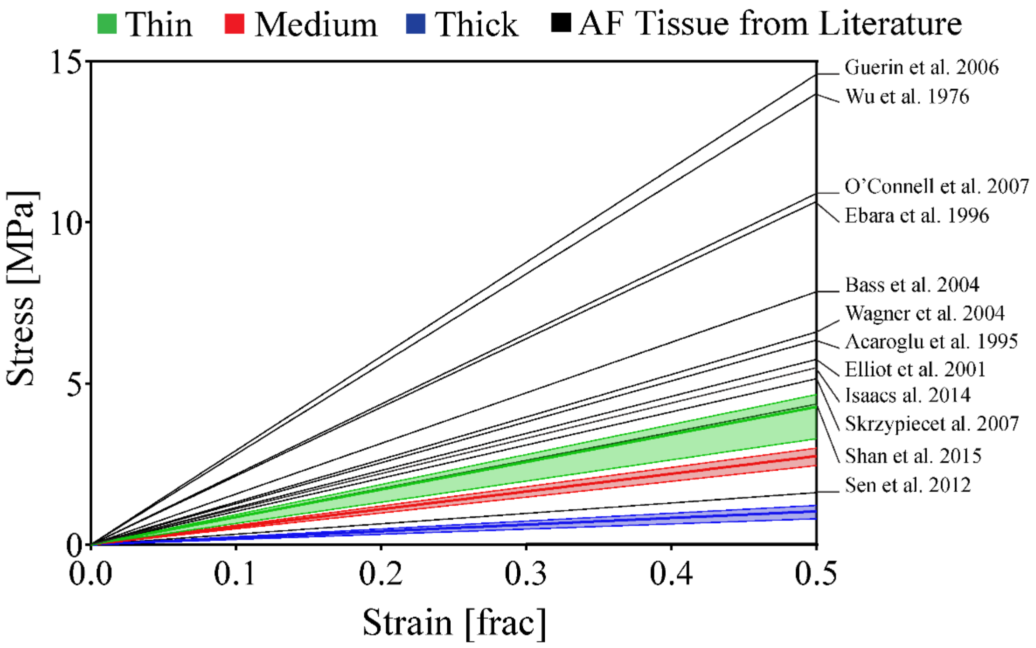

Figure 4-12: Mean, maximum and minimum tensile linear modulus of electrospun membranes obtained on the last loading cycle with a maximum strain of 35 % from all time points combined with circumferential linear moduli from tissue level AF response found in literature [76–79,231–238] visualized as stress vs strain curves.

There is a large body of literature that investigates the tissue level mechanical response of the AF extracted from human IVDs. These measurements done on multiple AF lamellae bundles loaded in the IVD's circumferential direction provide context for the stiffness and strength that is required of ES membranes to provide mechanical support. The linear tensile modulus obtained from tissue level circumferential AF measurements in literature are contextualized in Figure 4-12. The comparison shows that there is an overlap at the lower range of the mechanical response of the AF and the upper range of the PCL membrane properties used in this study. Furthermore, the scale of changes in the modulus due to aging of the material under in vitro conditions utilized in this study is negligible compared to the uncertainty of the mechanical properties of the AF. These results are promising for the use of electrospun PCL membranes as load bearing scaffolds in AF repair. With the addition of adhesives [239,240] and cell seeding techniques [204,219], the stiffness can be further increased if required.

4.5.3.2: FE model comparison

Local strain levels in the disc under complex physiological loading conditions were predicted. This provides complementary data to the tissue level response, where tissue samples are tested in uniaxial tension. The plateau value from Figure 4-9 which describes the maximum theoretically possible value that the elastically recoverable strain can reach at a given time point, suggests that recoverable strain in excess of 30 % is achievable for the electrospun membranes produced in this study. To achieve the desired elastic response, it is important to consider the preconditioning to prepare the membranes for the strains that will be present in vivo and access the hyperplastic J-curve response observed after preconditioning. Comparing this finding with the normalized frequency of the occurring strains in the AF in Figure 4-10 shows that a small number of loading cases invoke strains in excess of 40 %. Similar values for the strains experienced by the outer layers of the AF when tested on the organ level have been described in literature by Skrzypiec et al. 40% ± 11 SD [241] and Shan et al. 38.1 % ± 13.1 SD [238]. Others recorded even lower strains at failure of 13 - 25 % [79,234,236]. The strains above the elastically recoverable range would lead to a degree of plastic deformation and slack in the membrane. However, the samples exhibited exceedingly high tolerance to tearing up to 150 % strain, which means that a mechanical seal is guaranteed at the application site even if design strains are exceeded, which is important for maintaining organ isolation and integrity in vivo. While the ES samples were only tested in uniaxial tension, and the true strains are not assessed in this study, the high levels of resilience provide a promising result for their use in AF repair applications.

In this study it was possible to clearly establish the effect of an in vitro environment on the modulus and recovery in biomechanically relevant loading conditions for electrospun PCL networks. The effect of incubation produced clear trends and allowed to obtain valuable design guidelines for the membranes. Furthermore, the comparison of the mechanical behaviour of the synthetic membranes to the in silico model showed promising biomechanical compatibility of these constructs. However, the study was carried out without the presence of live cells, which can significantly affect the environment through enzymatic activity and induce significant changes to the material properties of the membranes. Introduction of live cells to the experimental design would have led to difficulties with accessing the changes mechanical and material properties of the membrane due to the presence of additional matter. In particular, distinguishing the mechanical changes attributed to the change in the membrane and those produced by cell proliferation. Furthermore, the cyclic experiments were carried out at only a single frequency, which meant that the viscoelastic properties of the material could not be assessed. No control group at room temperature was assessed, however such group would most likely have similar evolution to the group kept dry at elevated temperature, as observed by studies on various bulk polymers, and therefore would not provide any valuable insight.

4.6: Conclusion

In summary, the mechanical properties of electrospun PCL membranes of varying fibre diameters were investigated at different time points after exposure to cell culture medium at elevated temperature. The membranes showed stiffening and an increase in modulus with decreasing fibre diameter, as well as with longer incubation times. Furthermore, the modulus decreased with repeated cycles of increasing strain. The recovery after preconditioning increased with higher strain levels and did not vary significantly with incubation time. The magnitude of recoverable strain with a preconditioning cycle reached a theoretical maximum of approximately 30% which is in the range for many biomechanical applications. The results of the physical investigation were compared to predictions of an in silico model of intervertebral disc, where the strains experienced by the annulus fibrosus were investigated. The strain tolerance of the membranes showed a promising correspondence to the values observed in silico as well as experimental results from literature for native human disc tissue under physiological loading.

Chapter 5: In vitro validation of the IVD hernia repair strategy and repair strategy optimization

Dmitriy Alexeev[1], Stephen J. Ferguson[1]

[1] ETH Zürich, Institute for Biomechanics, Zürich, Switzerland

5.1: Abstract

Ex vivo models are labour intensive and can be expensive. They also come with high inter-sample variability and additional testing requirements. In the scope of testing strategies to repair ruptured annulus fibrosus (AF), this study investigates the design of an inexpensive synthetic model in vitro disc model that would perform mechanically similar to an ex vivo IVD model and would replicate some crucial aspects of the IVD herniation. Several synthetic analogues for the AF such as cast silicone and commercial silicone tubing are evaluated, as weak as hydrogel nucleus pulposus (NP) analogues made up of agarose and gelatin. It was established that while individual aspects of the mechanical response of the IVD could be approximated, such as compressive modulus, the overall mechanical response of the synthetic models was not significantly similar to be deemed scientifically relevant. Surface strain measurements of the synthetic samples in intact state, an injured state (central AF puncture), and repaired state (repaired with electrospun PCL membrane and silicone glue) were performed using 3D image correlation method. The strain measurements allowed to identify buckling behaviour under compressive strains related to membrane stiffness and cross-section. Overall, the electrospun membranes showed high resilience under strain conditions simile to those found in vivo.

5.2: Introduction

To utilize the membranes developed and described in the previous chapters in the intended application of intervertebral disc (IVD) herniation repair, the repair process needs to be defined and optimized. A well-established model of an ex vivo bovine IVD has been chosen as a gold standard. Outside of human ex vivo models or in vivo animal models, the ex vivo bovine IVDs are the closest to the intended application, as this model provides both similar size and mechanical properties to the IVDs found in humans [242,243]. However, the use of the ex vivo model imposes significant limitations on the testing throughput and cost of the experiment. To overcome these limitations a synthetic disc analogue can be utilized, provided it possesses similar mechanical properties to the organic counterpart.

The IVD is mechanically an extremely complex organ, with multiple tissues with significantly different anisotropic mechanical properties, viscoelastic behaviour, and mechanical response strongly dependent on environmental conditions such as hydration, ionic content, and temperature. Multiple attempts have been described in the past to create a whole organ replacement IVD [244–246] as well as individual tissues [82,247–249], mostly for the purposes of being used as a replacement or repair for damaged discs in vivo. For the purposes of testing repair strategies, the purely tissue engineering [250–252] approaches are too resource and time consuming and do not offer an advantage over ex vivo model.

There are further limitations on the design for repair testing, as it needs to morphologically approximate the organ, therefore strategies that focus only on the mechanical restoration and lack the morphological similarity are excluded. In addition, the herniation, which is the protrusion of the NP through the defect in the AF, needs to be approximated, consequently homogeneous materials that do not adhere to general tissue mechanics can also be excluded. Furthermore, the approaches that use expensive or time- consuming techniques would not be considered. Considering the abovementioned requirements, the authors are unaware of any pre-existing models that fulfil those requirements. Hence in this study, a model comprising a stiff outer AF and hydrogel inner NP tissue analogue, with and without endplate confinement, was assessed.

While replicating all mechanical properties of the native IVD is outside the scope of this study, the authors attempt to find a synthetic model that replicates the key aspects relevant for assessing the repair strategy. These aspects include compressive mechanical modulus and torsional stiffness and an intact and injured state similar in mechanical response to that found in native IVDs. This would allow to investigate the efficacy of the repair to mechanically support the injured discs. In addition, an investigation into the surface strains in the intact, injured and repaired state is conducted utilizing scaffolds made up of fibres of three significantly different diameters. This investigation allows to identify design flaws in the repair construct that might lead to inadequate mechanical performance in the final application.

5.3: Materials and Methods

5.3.1: Study Design

I this study the performance of various synthetic disk models is assessed. The model is broken down into the naturally occurring tissue components of the IVD. The AF is simulated using 3 silicone formulations: cast silicone tube, silicone sheet that is joined to form a tube and purchased silicone tubing.

5.3.2: Electrospun PCL

Electrospun PCL membranes were produced using the electrospinning device EC-CLI by IME Technology. PCL (Sigma-Aldrich, Mn = 80’000 g/mol) was dissolved together with NaCl (EMSURE, 99.5 %) in a mixture of methanol (Fisher Chemical, ≥ 99.8 %) and Chloroform (Sigma-Aldrich, ≥ 99.8%). The spun fibres were collected on a rotating drum with 90 mm diameter, rotating at 10 rpm and placed at a distance of 185 mm from the nozzle. To produce aligned fibres, another mandrel with a diameter of 20 mm was used and rotated at 2000 rpm. The spinning took place in a controlled environment at 24°C and 40% humidity. Every solution was left to spin for 15 hours. Four different films were electrospun with different PCL solutions and spinning parameters as listed in Table 5-1 below.

Protocol no.	w/v% PCL	wt.% NaCl	Methanol : Chloroform	Needle diameter [mm]	Voltage nozzle [V]	Voltage collector [V]	Feed rate (μl/min)
1	15.9	0.08	1 : 6	0.8	16	-1	16
2	12	0.08	1 : 6	0.6	16	-1	27
3	12	0.08	1 : 7.3	0.8	24	-2	26
4	12	0	0 : 1	0.8	24	-2	26

Table 5-1: Electrospinning parameters for the different electrospun scaffolds.

5.3.3: Disc Models

5.3.3.1: Annulus fibrosus analogues

Joined precast silicone

As an analogue to the AF, a ring of Polydimethylsiloxane (silicone, Maagtechnic MVQ L7200) was used. silicone was cut into strips of 7.4 mm × 10 mm × 3 mm. After ultrasonic cleaning in a solution of 70 % ethanol, the strips were dried at 80 °C for 30 minutes. To join the ends of the strips and form a circular shape, they were subjected to oxygen plasma (Harrick PDC-32G) for 30 seconds. Hose clamps were then used to immediately fix the strips in a circular geometry and join the strips' ends. Subsequent curing was allowed for 30 minutes at 80 °C, after which the strips' ends were attached with no visible seam.

Cast silicone

silicone rings were produced by moulding a silicone epoxy consisting of a pre-polymer base and a curing agent (silicone elastomer kit, Sylgard 184). Base and curing agent were mixed in different proportions summarized in Table 5-2 and degassed. Subsequently, the mixture was poured into tube-shaped aluminium moulds. After another round of degassing, the moulds were cured at different temperatures (Table 5-2). The obtained silicone tubes were cut into sections, yielding silicone rings with a thickness of 4 mm, a diameter of 27.3 mm and a height of 10 mm.

Ratio of base: curing agent	**Curing procedure**	**Wall thickness**	**Mechanical testing**
10 : 1	150 °C, 15 min	3 mm	Rings collapse
5 : 1	160 °C, 6 h	4 mm	Rings stable

Table 5-2: Moulding procedures for silicone rings and their performance.

Silicone tubing

Silicone tubing Rx-80 was purchased from DOW Corning with ID 12.70 mm, OD 19.05 mm and resulting wall thickness of 3.18 mm.

5.3.3.2: Nucleus Pulposus – Agar Gel and Gelatin

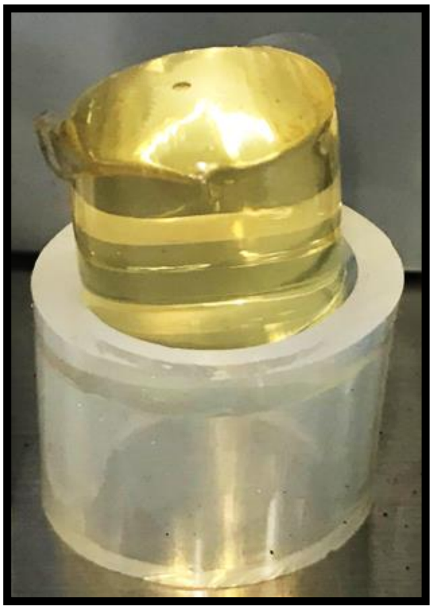

Figure 5-1: A sample of the gelatin core used to simulate nucleus pulposus removed from the outer synthetic annulus fibrosus.

The NP was simulated with hydrogels (Table 5-3). Solutions were prepared by mixing gelatin (Gelatin for microbiology, Merck) and Agarose (UltraPure Agarose, Invitrogen) with deionized water and heating in the microwave for 30s until the mixture is liquid. Due to its high viscosity, the solution with 25 wt.% gelatin had to be degassed after microwaving in an ultrasonic cleaning device to remove air bubbles. Before casting into the silicone rings, glutaraldehyde (GA, glutaraldehyde solution grade 2, Sigma-Aldrich) was added for some tests to crosslink the gels. To accelerate gelation, the structures were stored at 4 °C for an hour. Prior to mechanical testing, all samples were held at room temperature for 1.5 hours to equilibrate the temperature and ensure constant experimental conditions. Additionally, the gelatin core was always removed and reinserted to eliminate adhesion effects and preserve consistent test conditions as shown in Figure 5-1.

Core material	**Content [wt. %]**	**Additive**	**Content [wt. %]**
Agarose	2		
Gelatin	10		
Agarose	2	Gelatin	2
Agarose	2	Gelatin	8
Gelatin	5	GA	0.5
Gelatin	10	GA	0.5
Gelatin	10	GA	4
Agarose	2	GA	2
Gelatin	25		

Table 5-3: Hydrogels used to simulate the NP.

5.3.3.3: Endplates

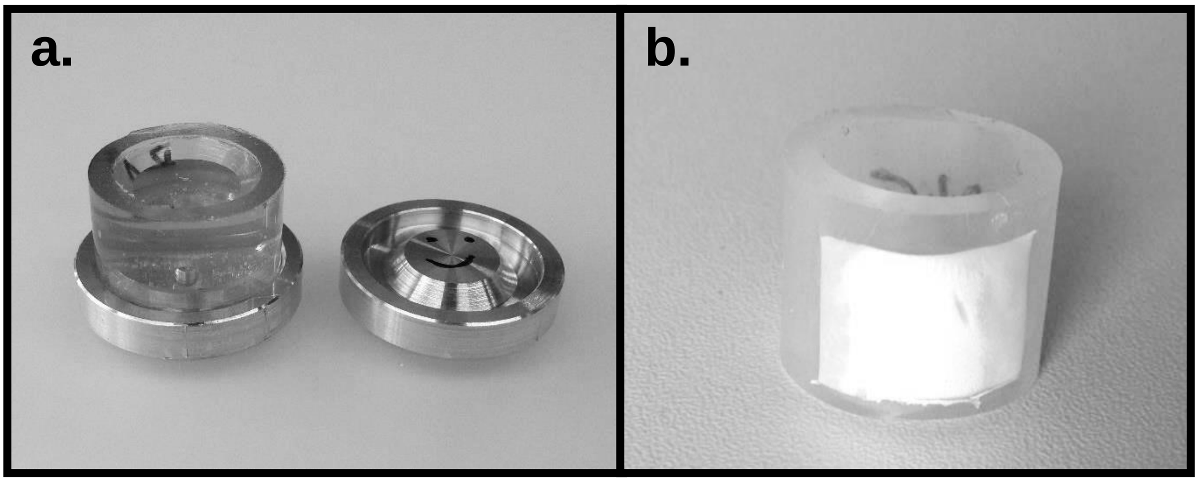

Figure 5-2: Punctured silicone tube filled with gelatin core with metal endcaps which were used during casting and mechanical testing to simulate the endplate (a). Punctured and repaired silicone tube (b).

Stainless steel endcaps were used for casting and testing to simulate the mechanical confinement provided by the vertebral endplates in an IVD. The caps were designed in a way that the strain of the core is higher than of the tube (Figure 5-2) to better replicate the conditions in a loaded native IVD with its curved endplates.

5.3.3.4: Defects and Repair

To simulate AF defects, the synthetic nucleus pulposus was removed and synthetic annulus fibrosus was punctured with a 4 mm diameter biopsy punch. The synthetic nucleus pulposus was then reinserted. 10 x 15 mm patches were cut out of the PCL scaffolds. PCL scaffolds were glued to the outside of the disc model as depicted in Figure 5-2 using the silicone kit (silicon elastomer kit, Sylgard 184). For the testing of the glue performance, the electrospun scaffolds were omitted and glue was deposited around the damaged area. Base and curing agent were mixed in the manufacturer recommended mass ratio of 10:1. The orientation of PCL scaffolds was chosen such that their curvature when glued to the rings, coinciding with their curvature on the mandrel during electrospinning, conformed to the outer circumference of the tube. The AF rings were left to cure at room temperature for at least 65 hours prior to testing, while the gelatin cores were stored at 4°C.

5.3.4: Mechanical Testing

Figure 5-3: Mechanical testing set-up for disc models. The samples were put between Parafilm and sandpaper on each side to ensure some friction but prevent soaking of the sandpaper.

All mechanical tests, unless stated otherwise were performed using an Instron E10000 with a set-up as displayed in Figure 5-3. The following protocol was applied for mechanical testing: the samples were pre-loaded with a stress of 0.06 MPa. Cyclic loading at a constant rate was performed over 20 cycles from 0.06 MPa to 0.5 MPa at 0.1 Hz. The stress of 0.5 MPa corresponds to the in vivo stress on human lumbar discs while standing [253]. This stress was maintained for 5 minutes to simulate creep. In the following torsional test, the stress of 0.5 MPa was maintained while 20 torsion cycles from -3° to +3° at a frequency of 0.1 Hz were performed.

The hydrogel NP analogues were assessed qualitatively after each test. The disc model composite with the synthetic NP insert was tested using the normal testing procedure described above to induce relevant strains. The appearance and water leakage was then assessed visually. If there were no significant tears in the hydrogel structure the hydrogel was considered sufficiently resilient.

For disc models with moulded silicone, lower loads had to be applied to prevent collapsing of the rings due to the structure's lower strength. Cyclic linear loading was performed over 20 cycles from 0.06 MPa to 0.25 MPa at 0.1 Hz. The stress of 0.25 MPa was maintained for 5 minutes to simulate creep. The following torsional test consisted of torsion at three different loads. The samples were subjected to 20 N (0.035 MPa, simulating a minimal force that at the same time keeps the specimen from slipping), 0.125 MPa and 0.25 MPa. 20 cycles from -3° to +3° at 0.1 Hz were performed for each load.

The modulus and torsional stiffness were investigated. The modulus of the construct was calculated by linear regression of the stress-strain curve. The 20th loading and unloading cycle was fitted from 60 to 100 percent of the maximum stress. The two values for loading and unloading were averaged. To calculate the torsional stiffness, the 20th cycle of the angle-torque curves was separated into the four phases for loading and unloading for each side. Linear regression for each phase and averaging over the four values yielded the analysed parameters.

5.3.5: Reproducibility Test

Reproducibility was an important consideration especially with the synthetic analogues manufacture in house. To ensure reproducibility, the modulus of the disc models was assessed after the synthetic NP was recast as new into the AF synthetic shell. The mechanical testing procedure described above was used. In the case of plasma-bonded silicone, two such tests were performed: simple recasting and recasting with testing after 65 hours. In the case of moulded silicone, only one round of recasting with testing after 38 hours was performed. For the various NP materials, the tests were also repeated to identify water leakage and breakage visually.

5.3.6: Digital Image Correlation

Figure 5-4: Setup of the INSTRON E10000 machine and the setup of the VIC 3D image correlation system.

Two cameras were mounted on a tripod in front of the INSTRON machine. They were placed symmetrically at a distance of approximately 27 cm to the samples. To ensure a three-dimensional recording of the area of interest, the cameras were located on two different sides of the sample as shown in Figure 5-4.

2 GigE cameras with Sony ICX814 sensors and 105mm Rodagon lens with a 120 mm extension tube were used, which shot up to 10 fps at a resolution of 9.2 megapixels. The cameras were connected to the DAQ-T4D trigger device. In order to get a good illumination of the surface, a NC-1815-675 softbox by Sumikon was utilized.

Once the specimen was preloaded, the recording system was manually triggered after a programmed 10 second stationary period. Every half second an image of the current state was recorded.

5.3.6.1: Digital image correlation software

The images were transferred to the VIC 3D image correlation software, whereby the first picture was set as zero-strain (reference) state. The following images were than analysed sequential for the change in pattern using the software to produce a measurement of normal engineering surface strains in the x direction (xx) and in the y direction (yy). In this setup the xx strain corresponds to the plane perpendicular to the vertebral axis while the yy direction is along the disc vertebral axis.

5.3.6.2: Speckle pattern

For the intact and injured discs, a speckle pattern was applied using an airbrush with a nozzle size of 0.2 mm. White opaque colour was sprayed onto the surface at a distance of approximately 30 cm and pressure of 2 bars, as the underlying material is transparent and therefore not suitable for motion capture. To apply the speckle pattern, dark blue colour was sprayed onto the painted surface also at a distance of 30 cm and pressure of 2 bars. For the repaired samples, dark blue paint was sprayed directly onto the patch. The samples with the speckle patterns can be seen in Figure 5-5.

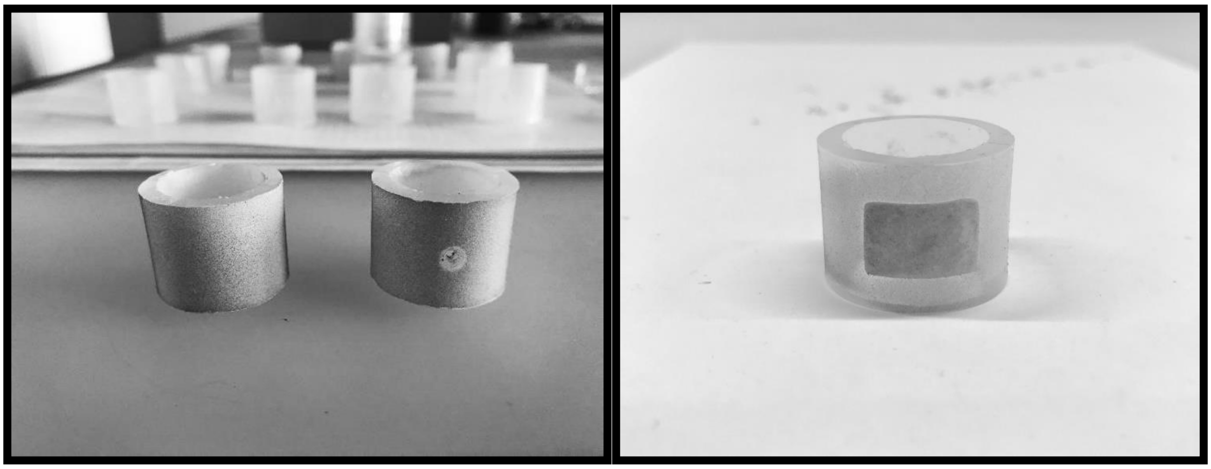

Figure 5-5: Left: non-holed samples with speckle pattern applied. Right: holed samples with speckle pattern applied on the repair scaffold.

5.4: Results

5.4.1: Synthetic Nucleus Pulposus

Material	Mechanical properties	Water leaking
Agarose 2 wt.%	Good	Yes
Gelatine 10 wt.%	Weak	No
Agarose 2 wt.% + gelatine 2 wt.%	Weak	Not tested
Agarose 2 wt.% + gelatine 8 wt.%	Weak	Yes
Gelatine 5 wt.% + GA 0.5 wt.%	Weak	No
Gelatine 10 wt.% + GA 0.5 wt.%	Weak	No
Gelatine 10 wt.% + GA 4 wt.%	Weak	No
Agarose 2 wt.% + GA 2 wt.%	Good	Yes
Gelatine 25 wt.%	Good	No

Table 5-4: Hydrogels used to simulate the NP and their performance. The mechanical properties are reported in the scope of mechanical failure at or below strains observed in vivo (Weak – significant tearing, Good - intact up to expected strains).

Table 5-4 displays the investigated hydrogels and their qualitative properties with respect to mechanical testing and water retention. The two main parameters that were assessed were tearing and water retention. Ultimately, the 25 % wt. gelatin was the only composition that allowed for reasonable mechanics and retained water on repeated loading. Glutaraldehyde increased neither mechanical properties nor water retention significantly.

5.4.2: Synthetic Annulus Fibrosus

5.4.2.1: Joined precast silicone and cast silicone

Figure 5-6 (top) shows a ring of plasma bonded silicone and the results of the reproducibility test for corresponding rings filled with 25 % wt. gelatin. The plasma bonding done with the procedure described in the methods section was not successful at producing a good bond that would not degrade with repeated loading. The rings that were cast using the described silicone moulding procedure (Figure 5-6, bottom) had reproducible mechanical properties.

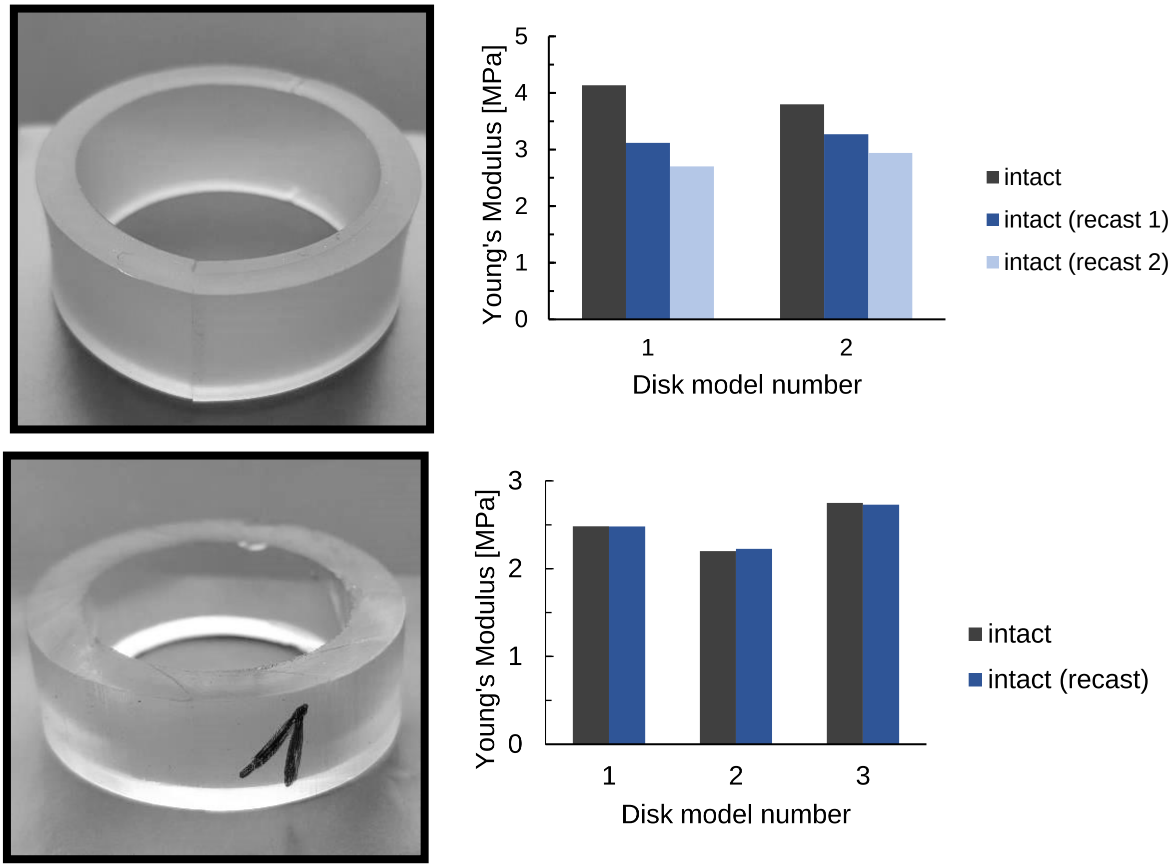

Figure 5-6: Plasma-bonded silicone ring with joint line in front (top left) and Young's modulus of two corresponding disc models over three cycles of recasting gelatin (top right). Moulded silicone ring with base: curing agent = 5:1 (bottom left) and Young's modulus of three corresponding disc models over two cycles of recasting gelatin (bottom right).

5.4.3: Complete Disc Model for Evaluation of PCL Patches

Figure 5-7 shows the assessed mechanical parameters of synthetic disc models made up of cast silicone and gelatin hydrogel core in the intact state compared to discs models in the following states: intact recast, punctured, repaired by unaligned PCL fibres, repaired by aligned PCL fibres.

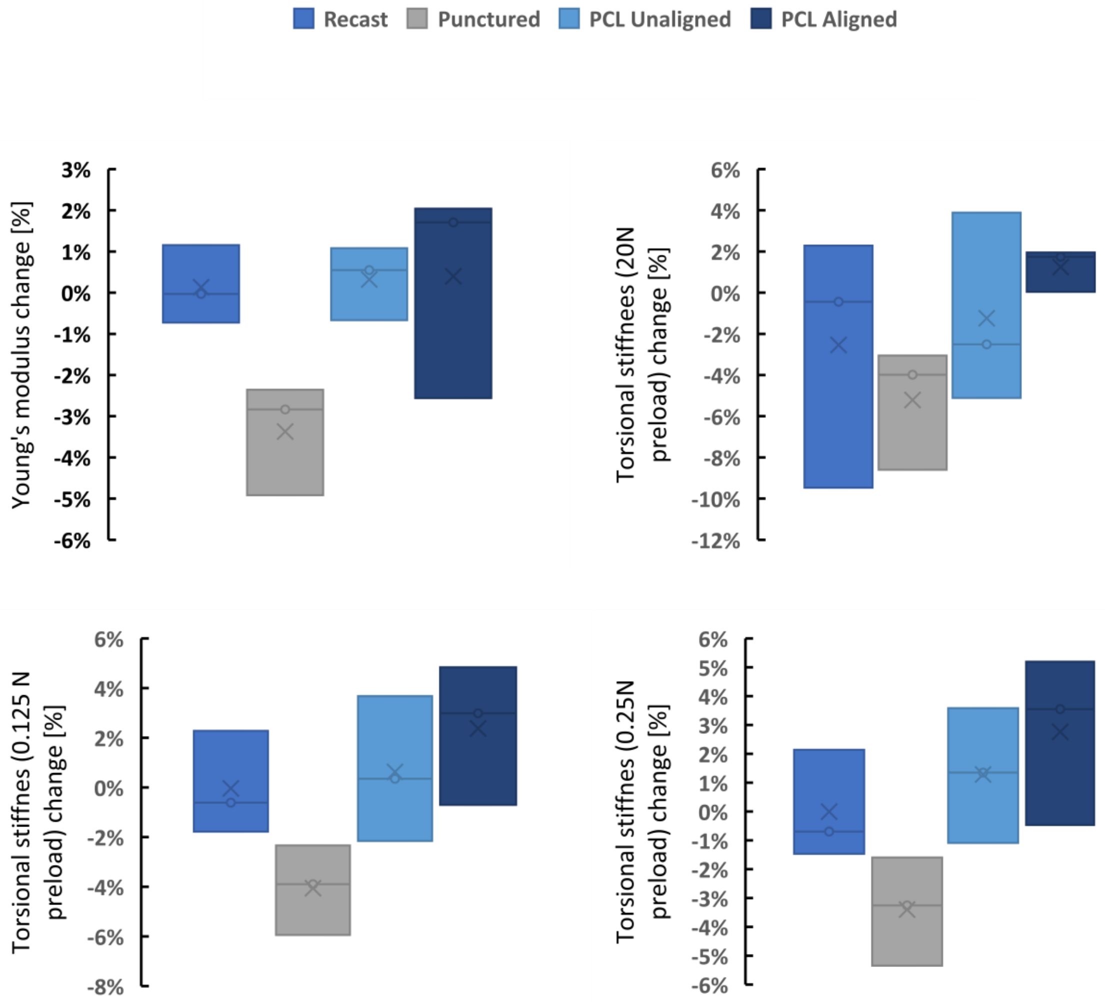

Figure 5-7: Comparison of mechanical parameters plotted as a box plot. Model discs in the intact state are compared to model disc in the following sates: recast and intact, punctured, repaired by patches with unaligned PCL fibers, repaired by patches with aligned PCL fibers. n=3

5.4.4: Silicone tubing with and without endcaps

While cast silicone AF analogue showed good reproducibility and desirable mechanical properties, to evaluate the performance of the endcaps, purchased silicone tubing was used to further eliminate variability and accelerate the testing process by eliminating the casting preparation.

The rigid caps on the top and bottom are meant to simulate the curvature of the native endplates and increase the strain on the synthetic nucleus pulposus by reducing the distance between the rigid endplates, while keeping this distance the same at the synthetic annulus fibrosus location. The results for the mechanical testing of silicone tubes as annulus fibrosus analogue coupled with gelatin nucleus pulposus analogue showed that only torsional stiffness was significantly affected and different between the punctured and repaired states. And this difference was only present in capped samples as seen in Figure 5-8.

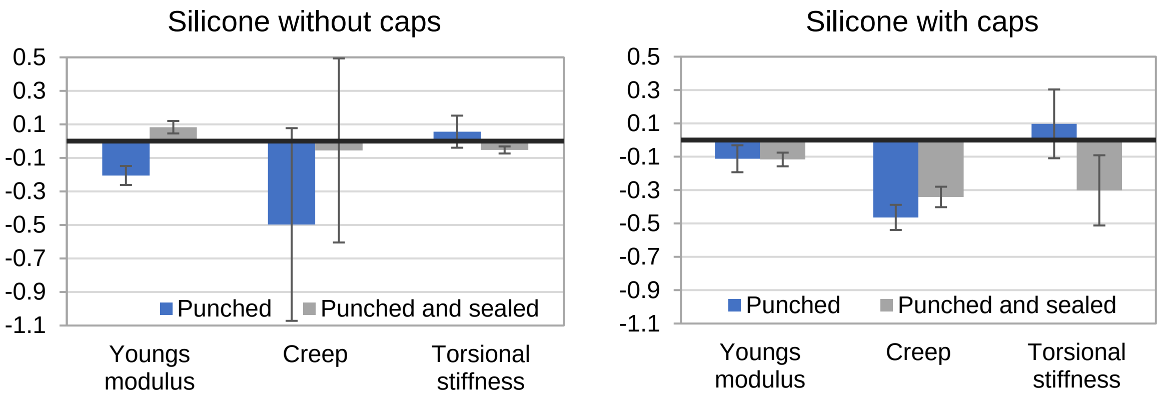

Figure 5-8: Relative change in properties of punched and punched and sealed disc models to intact disc models. Left: purchased silicon tubes without caps. Right: purchased silicone with caps on top and bottom.

5.4.5: Effect of silicone glue

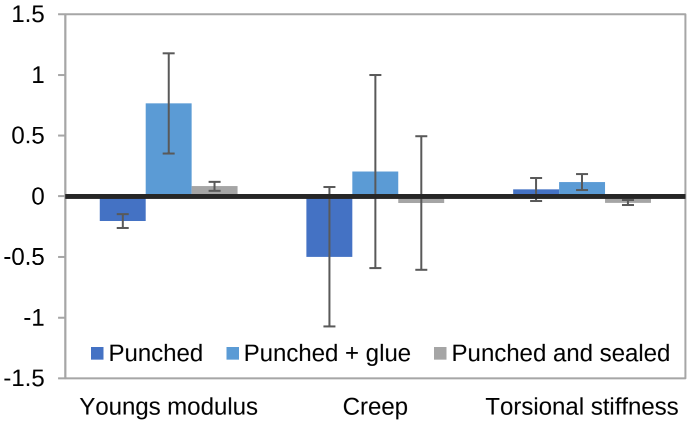

Figure 5-9: Comparison of punctured disc model, punctured disc model with glue attached and punctured and sealed disc model to intact disc model (n = 5).

The effect of silicone (silicone) glue that was used to attach the membrane to the silicone annulus fibrosus analogue was investigated, to isolate any effect of the adhesive from the effect of the membrane. Similarly, to the evaluation of the endcaps, purchased silicone tubing was used here. It was found that the glue has a very strong effect on the Young's modulus of the damaged samples as seen in

Figure 5-9.

5.4.6: Digital image correlation measurements for surface strain

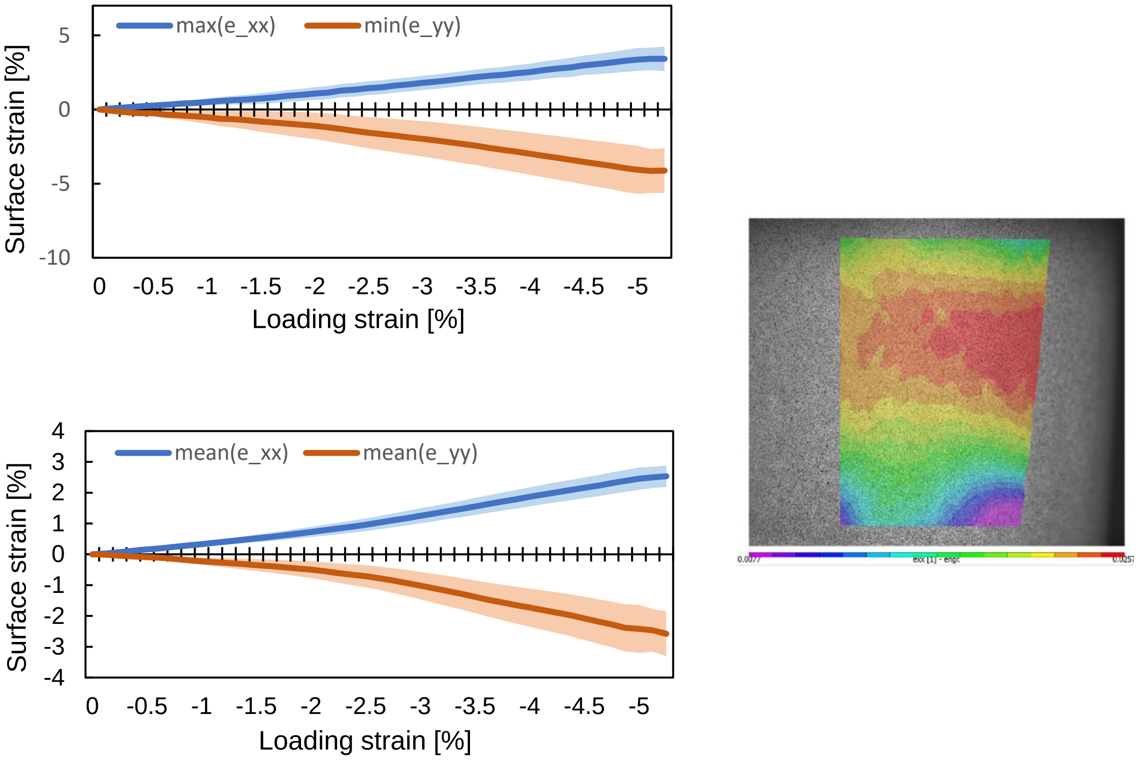

Figure 5-10: Engineering surface strain measurements of undamaged synthetic samples. n=15

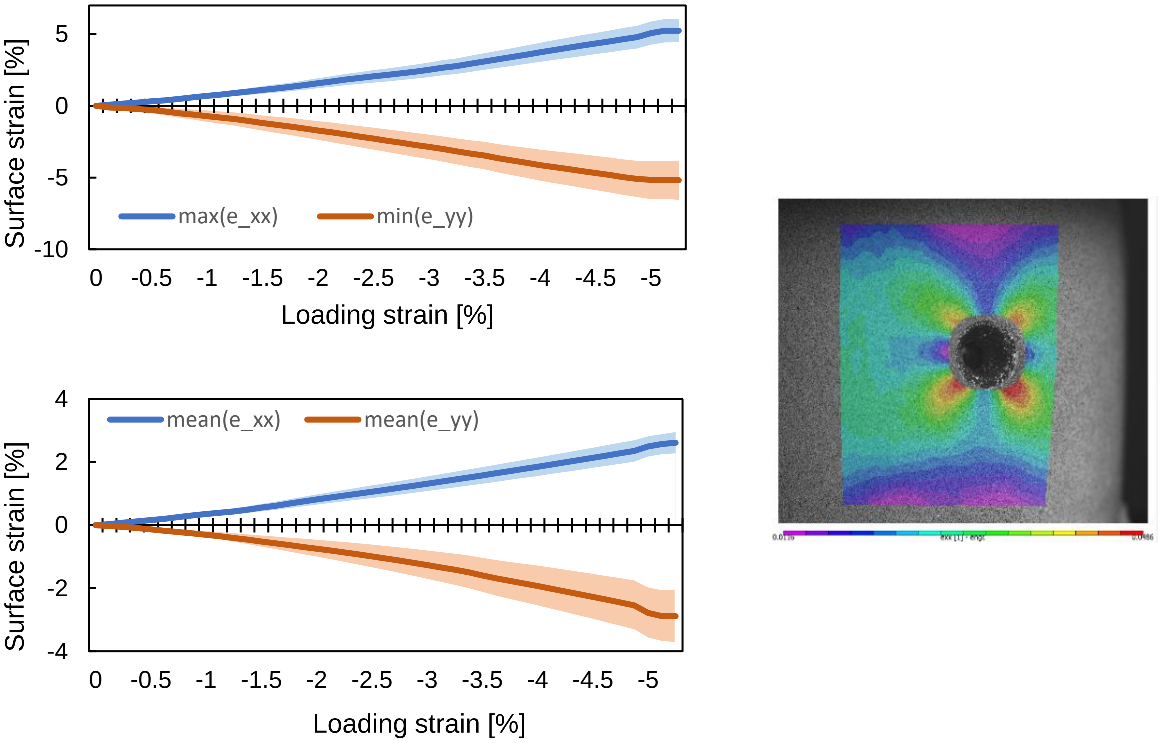

Figure 5-11: Engineering surface strain measurements of damaged synthetic samples. n=15

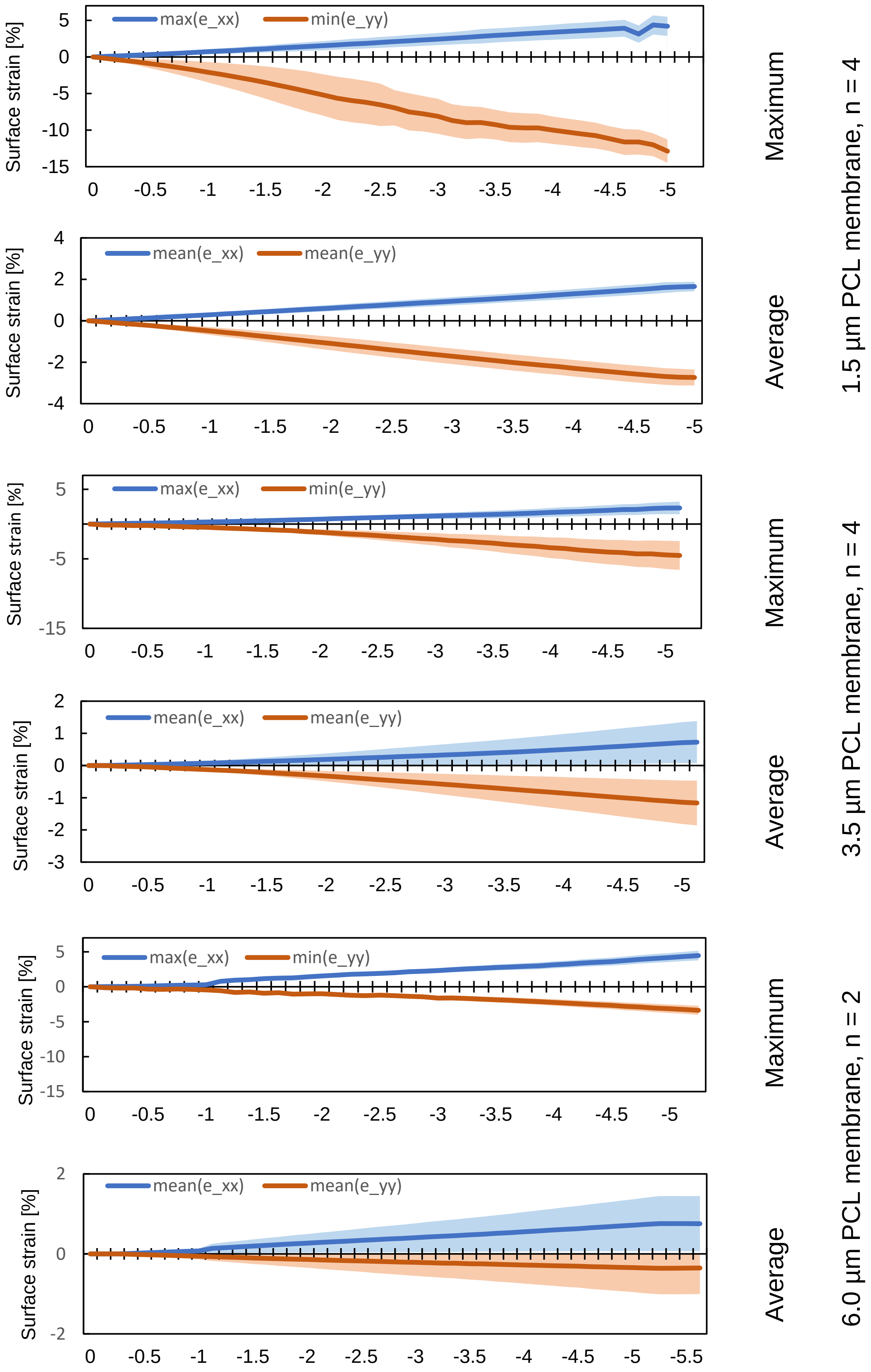

Figure 5-12: Engineering surface strain measurements of synthetic samples repaired with PCL membranes with different fibre diameters plotted against compressive strain measured by the mechanical testing equipment.

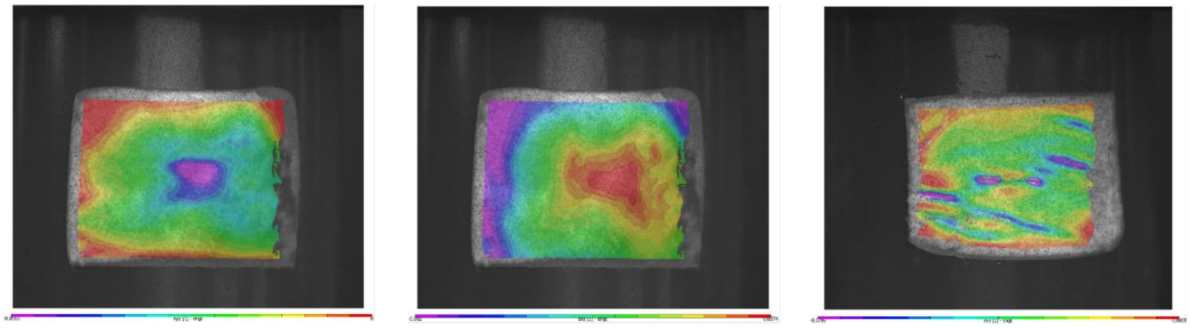

6 µm PCL membrane 3.5 µm PCL membrane 1.5 µm PCL membrane

Figure 5-13: Visual strain maps of the loaded samples with three types of membranes applied to the punctured site.

Digital image correlation measurements on the synthetic disc models are summarized as maximum and minimum surface strain in the xx and yy direction respectively, as well as mean surface strain in the same directions, plotted against the strain as measured by the mechanical testing equipment in the y direction. In Figure 5-10 the results for the intact samples showed an expected negative strain in the y direction during a compression test and positive strain in the x direction. In Figure 5-11 the samples punctured with a biopsy punch are described. The samples showed higher maximum and minimum strains due to stress concentrations at the damage site, while the mean values were similar to the intact samples.

The measurement of the strain on the patches was more difficult as the surface was uneven due to the fibrous nature of the membranes. The increasing fibre diameter presented increasing difficulty, with the 6 µm fibers being visible directly in the camera view. It is partially for that reason that the standard deviation of the mean strain increased with increasing fiber diameter. Furthermore, the samples made of thinner fibers showed significant buckling in compression. This is visually documented in Figure 5-13, where the folds are clearly visible. The surface buckling also contributed to the difficulties in obtaining a reliable surface strain measurement.

5.5: Discussion

5.5.1: Synthetic disc model

5.5.1.1: Synthetic nucleus pulposus

From Table 5-1 where the different materials used to simulate nucleus pulposus are summarized, 25 % wt. gelatin is the only material that approached desirable properties. While it is likely possible to use more advanced materials, such as composites, to replicate the behaviour of the NP more closely, the complexity and cost of such an approach would defeat the aim of an efficient methodology that would allow bulk testing of the repair strategies. In literature, there is large body of work attempting to create a NP surrogate directly for tissue engineering and regenerative medicine applications [254–258]. However, As the focus of the design strategy for these approaches is purely performance based rather than production efficiency, these strategies are often too complicated to provide a significant advantage to using ex vivo samples.

By visual evaluation, it was noted that the gelatin core of punctured disc models started leaking out during the mechanical test. Both aligned and unaligned PCL scaffolds were able to prevent this leakage, which indicates potential for mechanical stabilization of disc herniation.

5.5.1.2: Synthetic annulus fibrosus

Although the samples produced with plasma-bonded silicone appeared to be solid from visual inspection, mechanical testing showed continuous weakening, recorded as a decrease in Young’s modulus (Figure 5-6). The cause likely is the weakening of the plasma-bonded seam. This conclusion is supported by the data obtained for moulded silicone, for which no such effect was observed. Following the failure of plasma-bonded silicone, the use of moulded silicone was envisaged. Rings cast with a low amount of curing agent and a thickness of 3 mm buckled during mechanical testing, a higher amount of curing agent and a thickness of 4 mm instead of 3 mm were used for the final tests. Evaluation of PCL scaffolds was thus carried out with 4 mm thick, moulded silicone rings. While moulded silicone synthetic AF could withstand the required forces, the required thickness of the construct increased significantly, and the moulding process was time consuming and resource intensive. It was therefore decided to investigate commercial tubing materials as possible source of synthetic AF analogues.

The purchased silicone tubing was the only material that showed a decrease in Young’s modulus upon puncturing while the cast silicone tubes showed no effect. This is likely due to the cast silicone tubes being very thick, which minimalizes the effect of the puncture on the mechanical response in the tested range. Therefore, all further experiments were performed with the purchased silicone tubes.

Looking at Figure 5-7, the standard deviation between samples is quite high compared to the difference between disc states. The reason for this is the employment of a maximum stress of only 0.25 MPa instead of the envisaged 0.5 MPa due to the weakness of the structure. It is expected that the use of higher stresses would lead to an increased difference between intact and punctured states. However, the developed model resulted in highly reproducible results. No difference ($p < 0.6$) between intact and recast state was found. The mean Young’s modulus and torsional stiffness decrease in all cases from the intact to the punctured state ($p < 0.08$). The hole in the silicone ring decreases the model's ability to resist linear and rotational deformation. Both PCL patches successfully increased the resistance again ($p < 0.08$), which confirms their potential for mechanical stabilization of NP leaking. The only exception is torsion at 20 N for unaligned PCL. A reason for this could be the interface between the testing equipment and the silicone rings. A load of 20 N might have not been enough to fully engage with the rotational moment, such that the slippage sometimes occurred during loading. No statistical difference ($p < 0.4$) between patches of aligned and unaligned fibres was found for any of the assessed parameters and loading conditions. Possibly the fibre alignment was not sufficient. However, there seems to be a slight trend toward increased torsional stiffness for aligned fibres under all three loads. Higher stresses with their effect on the scaffolds and a larger sample size might also disclose dissimilarities between different alignments.

5.5.1.3: Silicone tubes with and without caps

The caps were designed such that they should potentially increase the effect of puncturing and sealing on the mechanical properties of the synthetic disc models. Nevertheless, this could not be seen in the results. The torsional stiffness increased for both silicone with and without caps, probably because the hole collapsed under the applied load and therefore increased the stability under torsion. In the case of the repaired samples, the torsional stiffness decreased again, since the PCL scaffold prevented the hole from collapsing.

5.5.1.4: Effect of silicone glue

The application of the glue alone had a large impact on the Young’s modulus. Therefore, the adhesive plays an important role for the change in the mechanical properties. The average properties for the punched disc model with only glue are even better than those with punched and sealed disc model, which is likely due to the glue alone being stiffer than the glue inside the soft PCL matrix. Here again, the deviation between the single experiments is rather big, no significant results were obtained. This is the result of glue application process being highly operator influenced.

5.5.2: Comparison of the synthetic model to the ex vivo bovine tail IVDs

The synthetic model must be comparable to the ex vivo model in both its overall mechanical response in the intact state as well as change in the response due to the puncture injury which is commonly described in literature.

The ratio of stiff outer AF shell and relatively soft NP in the synthetic constructs was chosen in match the native bovine IVD compressive stiffness and fell in the range of Young's modulus of 3-10 MPa. This value is well in line with what is observed in literature [259,260]. While the overall designed compressive modulus was achieved, the response to puncture differed between various constructs as documented above. In vivo, the changes in Young's modulus and torsional stiffness vary depending on the mode of injury. In case of this study the effect of puncture injury using a biopsy punch to the central AF was investigated. As noted previously only the commercial silicone tubing with gelatin core was able to show a significant decrease in modulus and torsional stiffness with puncture, which would agree with the behaviour observed in literature. Li et al. noted a lower dynamic compressive modulus in injured discs in an ex vivo organ culture [261].

5.5.3: Surface strains of synthetic annulus fibrosus repair

Several challenges had to be overcome to obtain a high-quality image correlation measurement on the synthetic disk model. These challenges introduced some limitations on the use of the method to characterize the surface strains of the synthetic disc model.

1. The synthetic NP made up 25% gelatin had to be completely homogeneous to avoid diffraction of light through the impurities, which otherwise would produce shadows and false registration.
2. By compressing the samples to analyse the strain distribution, an out-of-plane motion of the tube occurs which is transferred to the PCL scaffold. This moves

the pattern out of focus, so the image correlation registers high errors or ignores the date due to the threshold settings. Therefore, only small compressive strains can be measured precisely.

3. The translucent surface of the tubes which act as synthetic AF means that the surface needs to be made opaque with a coat of white paint. This introduces another material layer on top of the underlying structure. If applied thin enough it should not influence the local surface strain values.

Several modified setups have been described in literature that would allow to overcome some these challenges in the future. A rotating setup for the stereo cameras can mitigate the issues with curvature of the IVD[262]. The use of 2D laser scanning equipment has also been reported, however the resolution suffers significantly in this approach[181,263]. The laser method is useful to validate the deformations of the organ scale, however the resolution is likely not high enough to investigate small regions of interest such as millimetre scale injuries.

5.5.3.1: Surface strain of intact synthetic samples

Figure 5-10 illustrates the maximum strains in x- and in y-directions. It shows nearly the same strain in both directions, which would imply a Poisson ratio of 1. The measured value is not within reasonable range for a solid [264]. As previously discussed in the results section, different sources of error may affect these results. The measurement in the x and y plane has different accuracy due to the focus plain of the cameras being incident to the circumference of the sample, having good tracking of strain in y-direction which is parallel to the focus plain but poor tracking of x-direction that curves away from focus plane and causes blurring.

5.5.3.2: Surface strain of holed synthetic samples

A similar issue arises for the value of Poisson ratio in case of damaged samples. It is expected for a classical solid to observe the strain in xx-direction to be lower than in yy-direction. Discontinuities in the geometry causes the specimen to experience a local increase in the level of stress, which can be denoted as high strain in the data. This is because the force applied cannot be evenly distributed over the area of the sample. There is stress concentration at the edges of the puncture location, leading to higher strains than in the intact samples. This behaviour however is likely not representative of the in vivo conditions as native AF does not have sharp solid edges when it is injured.

5.5.3.3: Surface strain of sealed synthetic samples

The strain values for the patched samples in y-direction is higher than in xx-direction, which can be an effect of the glue application. More glue is applied next to the hole than on the top and bottom. This causes the patch to be more resistant in xx-direction to stretching than in yy-direction. Of course, here once again the limitation of the precise measurement in the xx-direction applies. Comparing the values to literature, Stokes[265] found similar values to this study of surface strain of 3 -10% in compression. Heurer et al. also found strains of up to 2.5 % in the y-direction[181,266], which are in range of the strains observed here.

Patches with a thickness of 1.5 µm and 3.5 µm showed buckling effects during the compression test. Buckling can occur when a structure is subjected to compressive stress, even if it is below the failure stress of the material. An increase in loading causes the scaffold to become unstable and leads to significant and unpredictable deformations. That is why some high strain regions for the yy-direction, as depicted in Figure 5-13, can be seen. Buckling depends mainly on Poisson’s ratio, Young’s modulus, load applied and thickness of the material. Although the patch with fibre thickness of 1.5 µm has a higher Young’s modulus and the applied load is the same for all scaffolds, the buckling effect is higher due to its lower overall thickness of the patch. The patch with fibre thickness of 6 µm introduced additional challenges. The fibres are thicker, and the microstructure approaches the dimension resolvable by the camera’s optics. Hence, the software was not able to match the pattern from the cameras well as it relies on a consistent homogeneous background.

The mean strains in xx-direction are higher than in yy-direction, which can be an effect of the fibres on the surface moving as a reaction to the compression. Fibres which are vertically aligned begin to buckle at a certain point due to the compression of the sample. This buckling leads to a movement in xx-direction of the pattern which is spray-painted on the fibres. The VIC 3D program registers this deformation as a high strain.

Overall, the 3D digital image software allowed to identify potential considerations for the design of the patches. For example, the necessity to consider the relationship between the geometry of the patch and its stiffness, to avoid excessive buckling. The potential for stress concentrations at the damage site was identified. And the limitations of using the digital image correlation on electrospun scaffolds defined. The major limitation of this work was however the difficulty to conclusively propagate these findings to ex vivo or in vivo environments. This stemmed from the underlying limitations of the synthetic IVD models that were tested.

5.6: Conclusion

In this study the authors tried to identify an approach to create a synthetic model of an IVD that would perform mechanically similar to an ex vivo IVD model and would replicate some crucial aspects of the IVD herniation. This investigation led to the conclusion that, while such a construct could be possible, the attempt to reproduce the IVD with easily accessible and cheap materials that would outperform the use of an ex vivo model, in terms of cost and time investment, was unsuccessful.

Notably, the complex mechanical behaviours of the IVD were not replicated sufficiently to be deemed of scientific relevance. The herniation of the synthetic construct did not reliably replicate what is observed ex vivo. The only reliable values that could be investigated were the surface strain results. It was established that the electrospun scaffolds possess resilience in the strain range relevant for the in vivo applications. The scaffolds utilizing different fibre diameter affected the stress concentration at the injury site and possessed different limitations such as buckling under load of stiffer and thinner scaffolds. However, as the injury was not well represented due to the limitation of the underlying synthetic disc model, these results are of limited value, and the need for an ex vivo organ culture model was highlighted.

Chapter 6: Mechanical and biological characterization of a composite annulus fibrosus repair strategy in an endplate delamination model

Dmitriy Alexeev[1], Shangbin Cui[2,3], Sibylle Grad[1,2], Zhen Li[2], Stephen J. Ferguson[1]

[1] ETH Zürich, Institute for Biomechanics, Zürich, Switzerland

[2] AO Research Institute Davos, Davos, Switzerland

[3] The first affiliated hospital of Sun Yat-sen University, Guangzhou, China

Published as:

Alexeev, D., Cui, S., Grad, S., Li, Z. & Ferguson, S. J. Mechanical and biological characterization of a composite annulus fibrosus repair strategy in an endplate delamination model. *JOR SPINE* 1–16 (2020) doi:10.1002/jsp2.1107.

DOI: https://doi.org/10.1002/jsp2.1107

6.1: Abstract

This study compares the mechanical response of the commonly used annulus fibrosus (AF) puncture injury model of the intervertebral disc (IVD) and a newly proposed AF failure at the endplate junction (delamination) on ex vivo bovine IVDs. Biocompatibility and mechanics of a newly developed repair strategy comprising of electrospun polycaprolactone (PCL) scaffold and fibrin-genipin (FibGen) adhesive was tested on the delamination model. The study found no significant difference in the mechanical response to compressive loading between the two models. Primary goals of the repair strategy to create a tight seal on the damage area and restore mechanical properties, while showing minimal cytotoxicity, were broadly achieved. Post repair, the IVDs showed a significant restoration of mechanical properties compared to the injured samples for the delamination model. The FibGen glue showed a limited toxicity in the AF and produced a resilient and mechanically stable seal on the damaged area.

6.2: Introduction

Intervertebral disc (IVD) herniation is a very common and painful condition, where the outer layers of the IVD known as the annulus fibrosus (AF) are ruptured, which results in leakage of the inner nucleus pulposus (NP) material and consequently deterioration of the mechanical function of the organ. This damage is often sustained during intensive physical activity or due to tissue degeneration as a result of a pathology or aging. Almost 80% of the population experience lower back pain, of which approximately 40 % is a result of IVD degeneration[34,267]. Herniation of the IVD can occur through the endplate in the cranial-caudal direction, or laterally through AF failure. The injury of the AF and NP herniation are often followed by further degeneration due to immune responses, provoked inflammation and an array of circulating cytokines[268–270]. Severe back pain symptoms arise as a result of these processes as well as NP material directly impinging on the nerve root, and vascular and nerve invasion of the injury site[7,9,271]. To evaluate effective treatment methods, the injury model and the repair strategy need to be first considered individually and subsequently tested in conjunction.

To establish an ex vivo injury model which is most representative of the naturally occurring case, several types of AF ruptures that can lead to circumferential NP extrusion were considered. Two general rupture types were identified in the literature, including failure at the endplate junction and failure through rupture of the AF in central region. It has been shown that 65 % of discs rupture at the endplate, where the most common mode is through rim fracture[6]. These findings were supported by other studies documenting a frequent presence of cartilage tissue in herniated material[272,273], as well as a weak interface at the endplate in extension loads[274]. Failure through AF rupture in the central region is commonly investigated in the literature. Multiple studies have characterized the pathomechanism of the injury[261,269,275,276] as well as proposed repair strategies. The repair strategies can be divided into the strategies focused primarily on mechanical repair and sealing, largely reliant on synthetic materials, and hybrid strategies that aim not only to provide mechanical support but to also promote remodelling of the damage site through loading synthetic or tissue engineered matrices with live cells. Approaches adapted from existing strategies such as sutures[80] have shown promising results in preventing re-herniation in the short term. The use of hydrogels made up of collagen[277–280] and fibrin-genipin[281] as fillers for AF defects have shown to limit biomechanical deterioration. The fillers have also been enhanced with a retention scaffold on the IVD surface[282–284] to further reinforce the injury site. The second class of strategies applies tissue-engineering principles to replace the injured AF with cell-laden scaffolds[89,285–287] or cell sheets[288]. While the cell strategies show promising biomechanical results in small animals, as well as cell survival and proliferation, the main aim of accelerating regeneration of the injury by the addition of live cells has had limited evidence of efficacy. The more common failures at the endplate junction have not been investigated outside the clinical description. In this study, based on previously documented radiographs and MRI scans of the injuries at the endplate junction, a model most closely resembling that found clinically was established.

To repair the ruptured disc, a system that is biologically and biomechanically compatible must be chosen. Considering the inherent properties of the AF, mechanical design criteria that will allow for restoration of the original mechanical properties can be defined. The material of choice should be capable of withstanding large strains up to 40 %, based on the surface strains observed in IVDs[181,238]. Additionally, a tight seal on the injured area is required to prevent nerve and soft tissue ingrowth into the injury, as well as prevent further degeneration leading to NP extrusion which can both cause severe pain[7–9]. Furthermore, the repair construct should exhibit a modulus which is lower than that observed in the outer layers of the AF. Based on the review by Long et al.[289] a range of mechanical properties suitable for the repair were identified.

Electrospun (ES) poly(ε-caprolactone) (PCL) was chosen to fulfil the role of principal mechanical support. PCL is commonly used as a substrate providing mechanical support and guiding cellular activity in tissue engineering (TE) and regenerative medicine[290]. The ES networks can be produced with wide variety of fibre diameters and morphologies depending on the production process, and thus they can closely mimic the scale of structures and fibrous morphology of the extra cellular matrix[147–149]. The mechanical properties of these scaffolds can be tuned through alteration of spinning parameters to achieve various morphologies, fibre diameters and alignments. Previous research has shown that PCL can achieve mechanical properties in the required range of 1 – 40 MPa[222]; furthermore, the anisotropy requirements have been shown to be fulfilled through fibre alignment[84]. The required strain range of up to ± 40 % strain is also within the capabilities of the scaffolds. To attach the electrospun scaffolds on the surface of the intervertebral disc, fibrin-genipin hydrogel (FibGen) glue was chosen as it allows good fixation through chemical bonding with the IVD surface and mechanical interlock with the electrospun scaffolds. FibGen has been previously shown to have strong and tuneable fixation for collagen rich soft tissues[239,291], and mechanical properties in the range of native AF tissue[292].

We hypothesized that the new endplate delamination model would provide a medically relevant damage scenario, which would be significantly different from those previously used[261,269,275,276]. Furthermore, we hypothesized that the repair strategy devised would allow for the restoration of the mechanical response of the damaged IVD, create a tight seal on the damage area and would be cytocompatible. To investigate these hypotheses, a bovine tail IVD model was chosen, as it is well established and provides organs of similar size to human IVDs, with comparable mechanical properties[242,293].

6.3: Methods

6.3.1: Study design

To investigate the effect of the injury on the IVD, two types of injuries were induced (puncture and delamination). The IVDs were extracted from bovine tails and separated into 3 groups (intact, delaminated and punctured) with 4 samples in each group. The intact group was kept undamaged as a control, the punctured group used the traditional central AF injury model, while the delaminated group applied the new damage model near the endplate. The samples were tested on a schedule described in Table 6-1.

For the investigation of the repair strategy, samples were also separated into 3 groups (intact, injured, repaired) with 8 samples in each group. Only the delamination model was used as the injury and is therefore referred to as just the injured group. The samples were tested on the schedule described in Table 6-2.

Table 6-1: Study design for the investigation of the effect of injury type on the mechanical response of the IVDs.

Day	Test	Force range [MPa]	Frequency [Hz]	Loading time [min]	Groups
1	Compressive mechanical test Injury	0.02 – 0.38	0.2	15	Intact
2	Compressive mechanical test	0.02 – 0.38	0.2	15	Intact, Punctured, Delaminated
3 - 6	Dynamic loading	0.02 – 0.20	0.1	120	Intact, Punctured, Delaminated
7	Compressive mechanical test	0.02 – 0.38	0.2	15	Intact, Punctured, Delaminated

Table 6-2: Study design for the investigation of the efficacy of the repair strategy.

Day	Test	Force range [MPa]	Frequency [Hz]	Loading time [min]	Groups
1	Compressive mechanical test	0.02 – 0.38	0.2	15	Intact
	Injury				
2	Compressive mechanical test	0.02 – 0.38	0.2	15	Intact, Injured
3 - 6	Dynamic loading	0.02 – 0.20	0.1	120	Intact, Injured
7	Compressive mechanical test	0.02 – 0.38	0.2	15	Intact, Injured
	Repair				
8	Compressive mechanical test	0.02 – 0.38	0.2	15	Intact, Injured, Repaired
9 - 13	Dynamic loading	0.02 – 0.20	0.1	120	Intact, Injured, Repaired
14	Compressive mechanical test	0.02 – 0.38	0.2	15	Intact, Injured, Repaired

6.3.2: Intervertebral disc preparation

IVDs comprising cartilaginous endplates were harvested from bovine tails (10-12 months old), obtained from a local abattoir within 2 hours of death, and washed in phosphate buffered saline (PBS) containing 10% penicillin-streptomycin (Gibco, Zug, Switzerland) for 10 minutes, followed by a second wash in PBS with 1% penicillin-streptomycin. Three bovine tails were dissected for the injury model comparison, while five bovine tails were dissected for the repair strategy efficacy investigation. 6 discs were collected from each tail. Average diameter was 18.36 mm ± 2.28 SD, average height was 10.90 mm ± 1.34 SD. The IVDs were assessed visually for signs of degeneration or abnormal growth. Discs were cultured overnight in Dulbecco's modified Eagle's medium (DMEM 4.5 g/L glucose) with 2% foetal bovine serum (FBS, Gibco), 1% insulin transferrin selenium and 0.2% Primocin (Invivogen, Nunnigen, Switzerland).

6.3.3: IVD injury

6.3.3.1: Puncture model

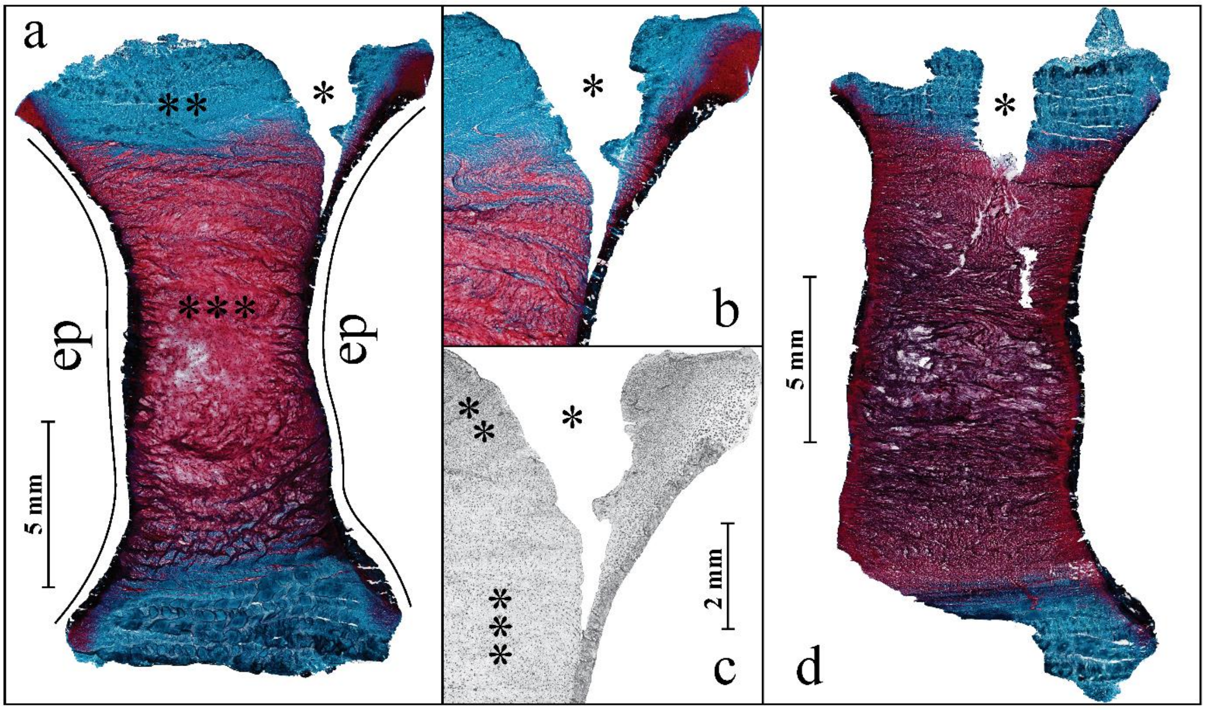

*Figure 6-1: The overview of a histological section stained with Safranin-O/Fast Green stain of the delamination injury after a total of 14 days in culture (a), here proteoglycans are stained red, and collagen is stained blue, live and dead cells are stained black. A closer look at the injury site with the same stain (b), and LDH stain of the injury site with live cells stained black (c). The gradient of cell density from the highly cellularized outer AF to the NP is clearly visible in the LDH stain. An overview of the punctured disc after 7 days in culture (d). The disturbance in the NP is in present here unlike in the delamination injury. * Injury site, **AF, ***NP, EP is the endplate location.*

The IVDs were injured using a biopsy punch (diameter 4 mm, length 7 mm, Kai Medical, Gifu, Japan) in the central region of the AF, penetrating to the NP region (Figure 1d). The methodology was adapted from Li et al.[261].

6.3.3.2: Delamination model

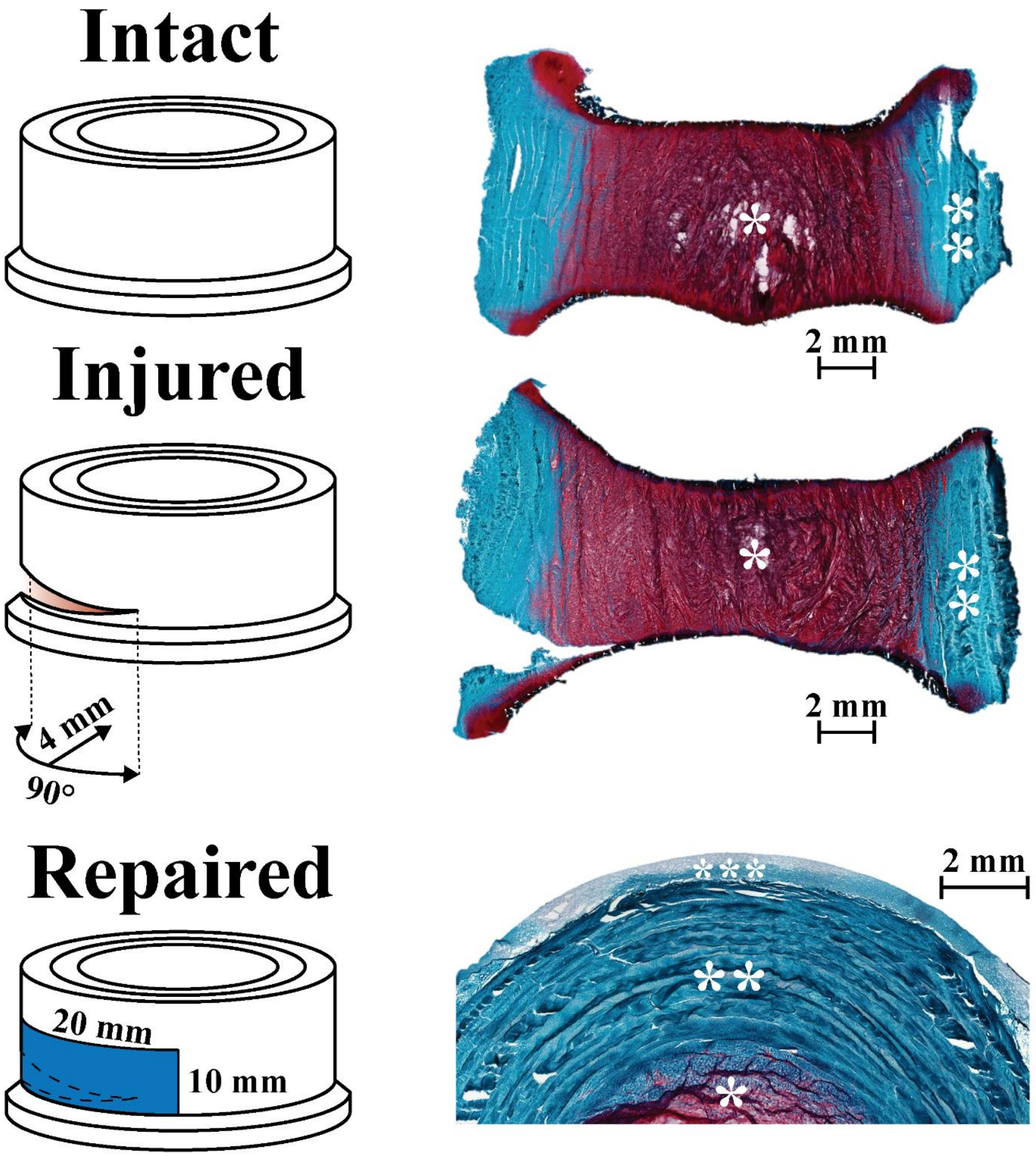

*Figure 6-2: Overview of experimental design starting with intact healthy disc, the injury was induced with scalpel blade to produce an injury 4mm deep and 90 degree section as close as possible to the endplate, finally the IVD was repaired using the electrospun PCL scaffold and FibGen glue. Histology images with Safranin-O/Fast Green staining obtained after 14 days in culture and 7 days after repair was applied show the three states in which the IVDs were tested. Note the close adhesion of the repair construct to the IVD surface. * NP, ** AF, *** repair scaffold*

The IVDs were injured using a N. 10 scalpel blade. An incision was made approximately 4mm deep, which corresponded to the length of the curved part of the blade, as close as possible to the endplate seen on a sagittal section in Figure 6-1 and 2. The incision was made in a 90-degree section.

6.3.4: Production of the repair (electrospun scaffold and FibGen adhesive) and its application

6.3.4.1: PCL scaffold electrospinning

PCL (Mn 80’000 g/mol, Sigma Aldrich Chemistry, 440744) scaffolds were produced using 12 wt. % polymer in 1:7.3 chloroform ($CHCl3$, Sigma Aldrich, ReagentPlus, 132950) to methanol ($CH3OH$, Fisher Chemicals, HPLC grade, CAS: 67-56-1) volume ratio solvent. IME Technologies EC-CLI electrospinning equipment was used with a translation nozzle stage and an 8 cm diameter rotating drum collector with a 19 cm spinning distance rotating at 10 rpm. The environmental parameters were controlled at 24 °C and 40 % relative humidity. A needle with inner diameter of 0.8 mm and outer diameter of 1 mm was used. The source voltage was set to 24 kV and collector voltage to -2 kV. The flowrate of the polymer solution was 26 µl/min. The mats that were produced were cut into smaller pieces of 20 by 10 mm for application. The scaffolds were sterilized using a cold ethylene oxide (EO) gas procedure and finally kept under vacuum for 5 days before use to remove EO residue.

6.3.4.2: Thrombin-genipin and Fibrinogen-PBS hydrogel adhesive (FibGen)

Stock solution of genipin (Sigma-Aldrich, G4796), in DMSO (dimethyl sulfoxide, Fisher chemical, D/4121/PB08) at a concentration of 50 mg/ml was prepared and stored at -20 °C. Before use, 60 µl genipin-DMSO solution were added to 140 µl of 100 U/ml solution of thrombin (from bovine plasma, Sigma-Aldrich, T7513) in PBS solution. The mixture was then stored at +4 °C. 70 mg of fibrinogen (from bovine plasma, Sigma-

Aldrich, F8630) were dissolved in 350 µl of PBS + 1 % Anti/Anti. The solution was kept in a water bath at +37 C and vortexed every 5 min to produce a homogeneous mixture. Consequently, maximum local concentrations of the FibGen hydrogel glue constituents following in situ mixing were: fibrinogen at 140 mg/mL, thrombin at 28 U/mL, genipin at 6 mg/mL and DMSO at 11 % volume.

6.3.4.3: IVD repair procedure (Figure 6-3)

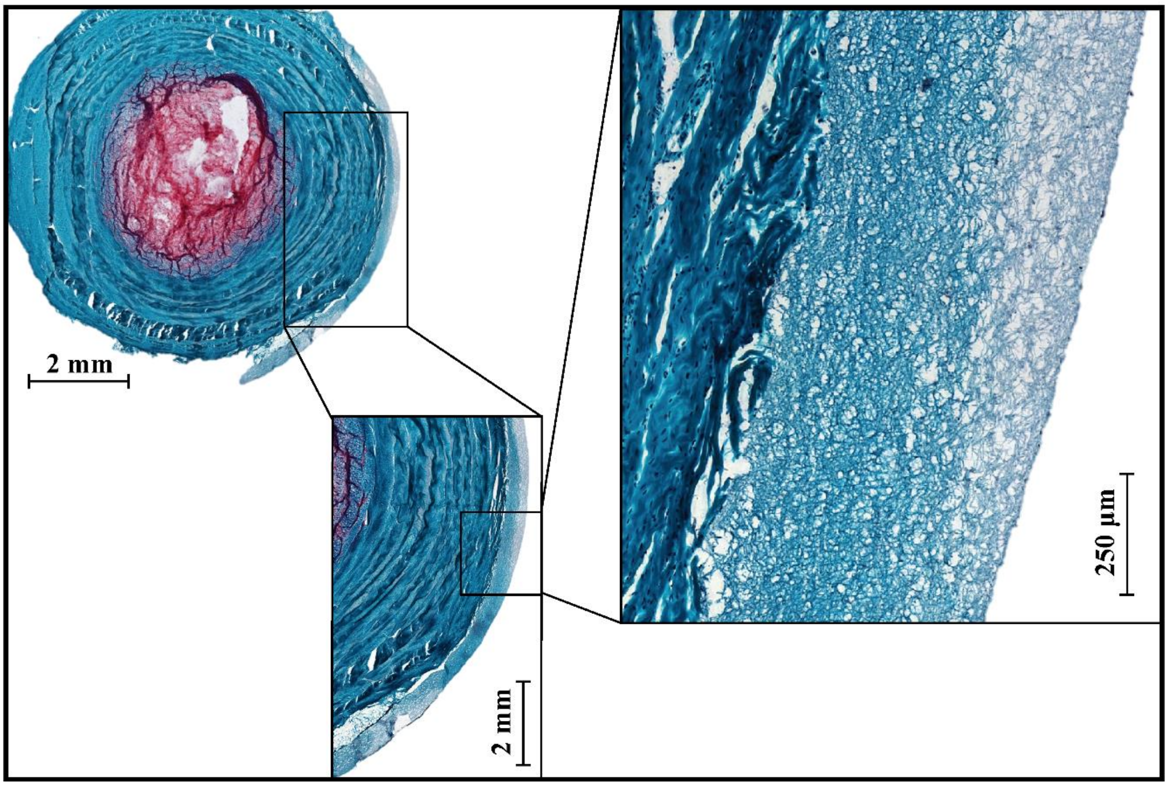

Figure 6-3: Overview of the repair scaffold and the interface with the outer layers of AF on Safranin-O/Fast Green stained horizontal section 7 days after repair procedure. Histology highlights the close adhesion and bonding of the scaffold to the outer layers of AF.

For the repair procedure, FibGen glue in two parts and the scaffold were prepared separately. Prior to application, the scaffold was soaked in thrombin-genipin solution, followed by application of fibrinogen-PBS on the IVD surface. The scaffold was then applied and the repaired IVDs were securely wrapped in sterilized paraffin film to create a tight seal for 20 min after which the repaired samples were kept in a 6 well plate with gauze soaked in PBS + 1% penicillin-streptomycin (Gibco, Zug, Switzerland) for at least 1 hour at 37 °C. The samples were then placed back in culture medium in the incubator.

6.3.5: Mechanical and physical disc characterization

Two types of mechanical loading scenarios were implemented. A lower stress 2-hour bioreactor loading protocol to simulate daily activity and a high stress 15-minute compression mechanical testing, which was used to evaluate the mechanical performance of the IVDs. The bioreactor loading and compression testing schedule is briefly described in Table 6-1 for the comparison of different injury models and in Table 6-2 for the investigation into the repair strategy. Dimensional measurements were taken before and after each mechanical loading for both protocols. The discs were kept under free swelling conditions between all bioreactor loadings and mechanical tests. The discs were kept in custom-made chambers during dynamic loading and mechanical compression testing, and in 6-well plates during free swelling.

6.3.5.1: Dimensional measurements

The cross-section measurements used to calculate stresses were taken directly after dissection using precision callipers. Cross-section area was calculated assuming an oval cross-section shape. Height measurements were taken daily before and after mechanical loading procedures using force limited callipers at 5 – 10 N. The height was calculated from the average of 3 measurements.

6.3.5.2: Bioreactor loading

Discs were cultured in a bioreactor system with physiological loading regime. The bioreactor was maintained in an incubator at 37 C, 85 % humidity and 5 % CO2. The dynamic loading was performed at 0.02 – 0.2 MPa and frequency of 0.1 Hz for 2 hours per day based on previously developed protocols [261,294–296].

6.3.5.3: Compression mechanical testing

Compressive mechanical tests were done at 0.02 – 0.38 MPa and frequency of 0.2 Hz for 15 minutes with custom made chambers mounted on MTS Acumen 3 Test System (MTS, Eden Prairie, MS). The maximum and minimum strains were recorded for each loading cycle, as well the minimum and maximum modulus which was calculated as the first 20 % of strain and the last 20% of strain of the loading curve. In literature, the minimum modulus is sometimes referred to as the toe modulus while the maximum modulus is referred to as linear modulus. The minimum strain in this study is sometimes referred to in literature as transition strain.

6.3.6: PCR

AF tissue samples at the injury site and opposite to the injury site (70 - 100 mg/sample) were collected from the IVDs. The samples used for gene expression analysis were snap frozen in liquid nitrogen, homogenized with 1 mL TRI reagent and 5 μl Polyacryl Carrier (both Molecular Research Centre, Cincinnati, OH, USA) per sample, using a Tissue-Lyser (Retsch & Co., Haan, Germany) and centrifuged (Eppendorf, Basel, Switzerland) at 4 °C for 10 min at 12000 g. RNA isolation was carried out according to the protocol from the manufacturer. Reverse transcription was performed using SuperScript® VILO™ cDNA Synthesis Kit (Invitrogen) and 500 ng of total RNA according to the manufacturer's protocol. StepOnePlus™ System (Applied Biosystems) was used to conduct quantitative real-time polymerase chain reaction (qRT-PCR). Gene expression of bovine collagen type I (Col1) and type II (Col2), aggrecan core protein (ACAN), matrix metalloproteinase 1, 3 and 13 (MMP1, MMP3, MMP13), a disintegrin and metalloproteinase with thrombospondin motifs 1 and 4 (ADMTS1, ADAMTS 4), and Interleukin 6 and 8 (IL6, IL8) in disc cells was analyzed using custom designed primers and TaqMan probes (Microsynth, Switzerland) previously described in Lang et al. [296].

6.3.7: Histology

After removal of the bony endplate from both sides with a drill, the IVDs were frozen in cryo-embedding compound (Sismex, Horgen, CH). Transverse and sagittal sections (10 μm) were cut with a microtome (Microm, Germany).

6.3.7.1: Safranin-O/Fast Green staining

The extracellular matrix (ECM) in the injury and repair sites, as well as the native tissue was qualitatively evaluated by Safranin-O/Fast Green staining. Sections were fixed in 70% methanol before staining. Sections were stained with 0.1% Safranin-O and 0.02% Fast Green to reveal proteoglycan and collagen deposition respectively, and counterstained with Weigert's Haematoxylin to reveal cell distribution.

6.3.7.2: Lactate dehydrogenase (LDH) and DAPI staining

The cell viability at the injury and repair sites, as well as the native tissue was quantitatively evaluated by staining. The cryosections were stained using lactate dehydrogenase (LDH) solution as described previously [261]. Staining was performed with LDH in 40% polypep solution (Sigma- Aldrich, Buchs, Switzerland). DAPI staining was performed using ProLong Gold antifade reagent with DAPI (Life Technologies, Eugene, OR). Six IVDs per group were analyzed, where regions of 4000 by 6000 μm were imaged at the NP, AF at the injury site and AF opposite the injury site. The cells stained with DAPI were segmented by ImageJ v.1.52p software in the whole imaged region of interest, the LDH stain intensity corresponding to each nuclei was measured to identify live cells. The total number of cells was in the range of 10000 for AF and 5000 for NP regions. The results were validated by manual count of four randomly selected small areas in each region. The cell distribution as a function of distance from the external boundary of the AF at the injury site and the intact site of each IVD were analyzed using an in-house Python script.

6.3.8: Glycosaminoglycan and nitric oxide medium assays

The total glycosaminoglycan (GAG) content of the culture media, collected at each media change, was determined by the dimethylmethylene blue dye method, using bovine chondroitin sulphate as the standard [297], to assess the release of matrix molecules from the sample into the media. Absorbance was measured with a Victor3 Perkin Elmer (Waltham, MA, USA) 1420 multilabel counter. Levels of nitric oxide (NO) production in the conditioned medium of IVDs were determined as the concentration of its stable oxidation product, nitrite (NO^{2-}), using the Griess Reagent Kit (Promega, Madison, USA) [298]. The results were calculated based on the medium volume in each well or bioreactor chamber and then divided by the volume of each IVD measured after extraction on day 0.

6.3.9: Data post-processing and statistics

Statistical analysis was performed using GraphPad Prism 8.2 software (GraphPad Software, Inc., La Jolla, CA, USA), unless stated otherwise. The viability of the cells in LDH measurements was analyzed using independent two-sample t-test at each location, with Holm-Sidak multiple comparison correction, due to the large dataset (3 transverse sections from 1 sample and 3 sagittal sections from another sample, $n = 6$). PCR data was first pre-processed to eliminate outliers using ROUT method at $Q = 1\%$, the normality of the dataset was then assessed and was found to be non-parametric in most samples due to low sample number: $n = 4$. Kruskal-Wallis test was then used to assess the significance of the results with multiple comparisons. The overall GAG and NO content were assessed through a Wilcoxon matched pair test, while individual time points were analyzed using an independent two-tailed two-sample t-test, with intact samples as control (n = 8). The mechanical data was analyzed with the SPM1D package for Python [299] using a two-tailed independent two-sample t-test based on random field theory, with intact samples as control (n = 8). $p < 0.05$ was considered statistically significant (* $p < 0.05$, ** $p < 0.005$, *** $p < 0.0005$).

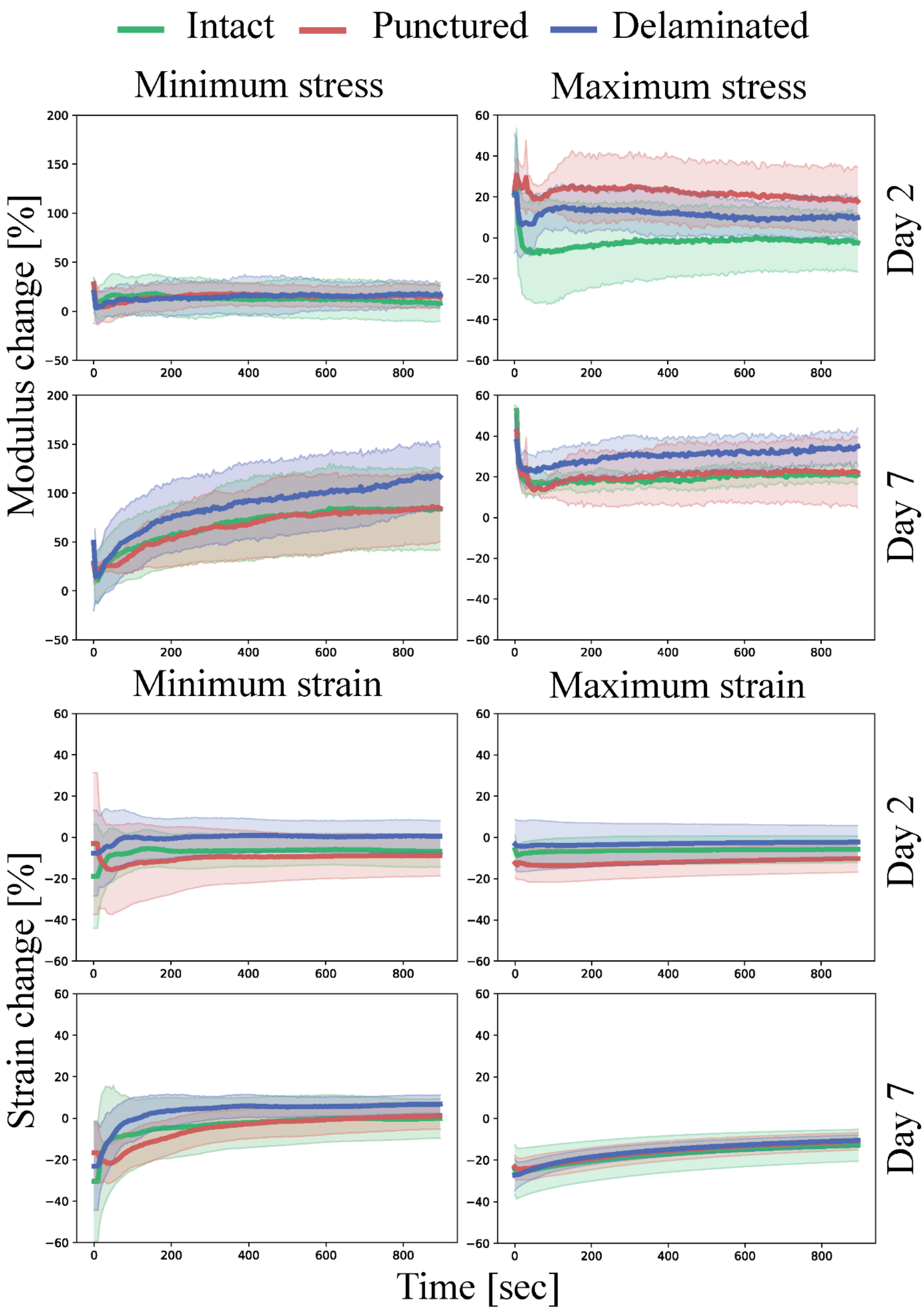

Figure 6-4: Minimum stress, maximum stress, minimum strain and maximum strain plotted against time with shaded areas representing standard deviation measured during cyclic (0.2 Hz) compressive loading of the samples with different injury types (punctured and delaminated) normalized to the values obtained from intact samples on day 0. n = 4

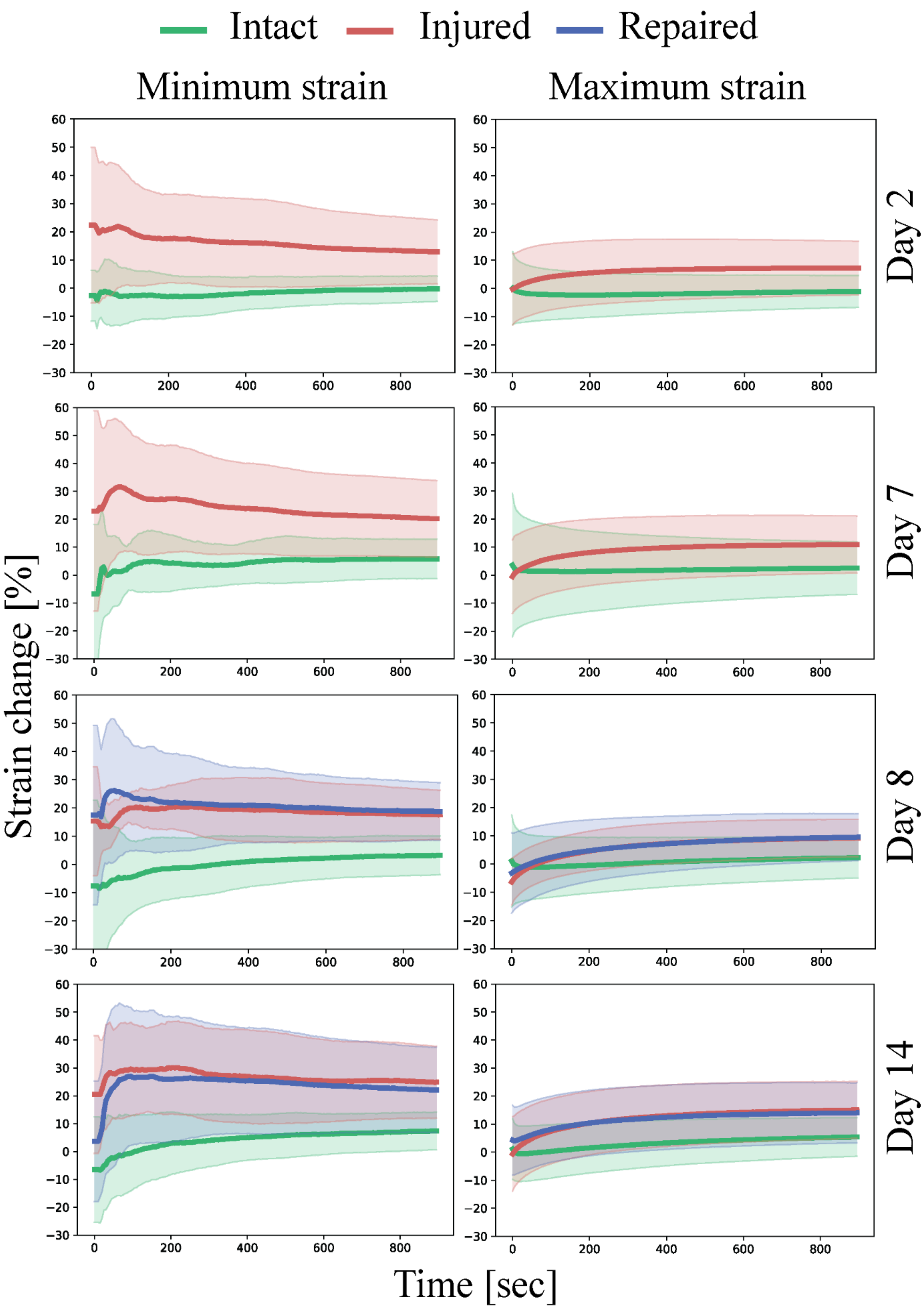

Figure 6-5: Minimum strain and maximum strain plotted against time with shaded areas representing standard deviation measured during cyclic (0.2 Hz) compressive loading of the samples in intact, injured and repaired states normalized to the values obtained from intact samples on day 0. n = 8

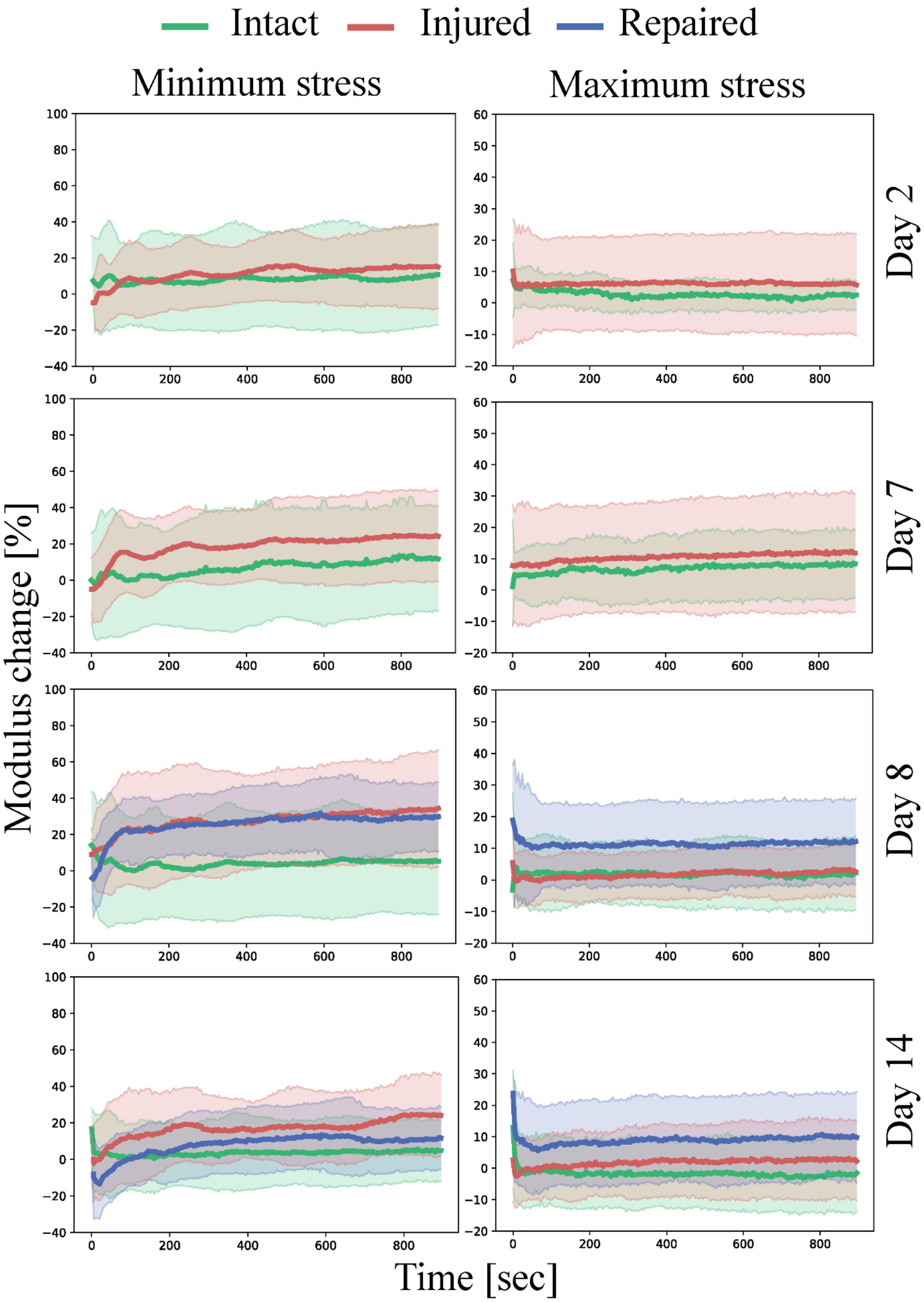

Figure 6-6: Minimum stress and maximum stress plotted against time with shaded areas representing standard deviation measured during cyclic (0.2 Hz) compressive loading of the samples in intact, injured and repaired states normalized to the values obtained from intact samples on day 0. n = 8

6.4: Results

6.4.1: Mechanical evaluation of the injury models and repair strategy

Similar to previous studies [300], the IVDs show a hyper-elastic and viscoelastic response where the initial loading curve exhibits low modulus in the beginning while the last part of the curve has a significantly higher modulus, as well significant hysteresis and time dependent behaviour. For each cycle four parameters were measured (maximum strain, minimum strain, maximum modulus and minimum modulus). These parameters are plotted as function of time and sample state in Figure 6-4 for the comparison of the two damage models investigated and in Figure 6-5 and Figure 6-6 for the investigation into repair strategy efficacy. The commonly reported disc height loss due to loading is not reported, as it is functionally the same as the maximum strain reached on each cycle, while also being less reliable due to manual nature of the measurement. The height measured before the samples were loaded (after recovery) did not show any significant differences between groups.

6.4.1.1: Mechanical comparison of the central AF puncture and endplate delamination injury models

No values were found to be statistically significant between injured, punctured and delaminated, groups for any of the mechanical parameters measured. The visual comparison between the models is documented in a horizontal section in Figure 6-1.

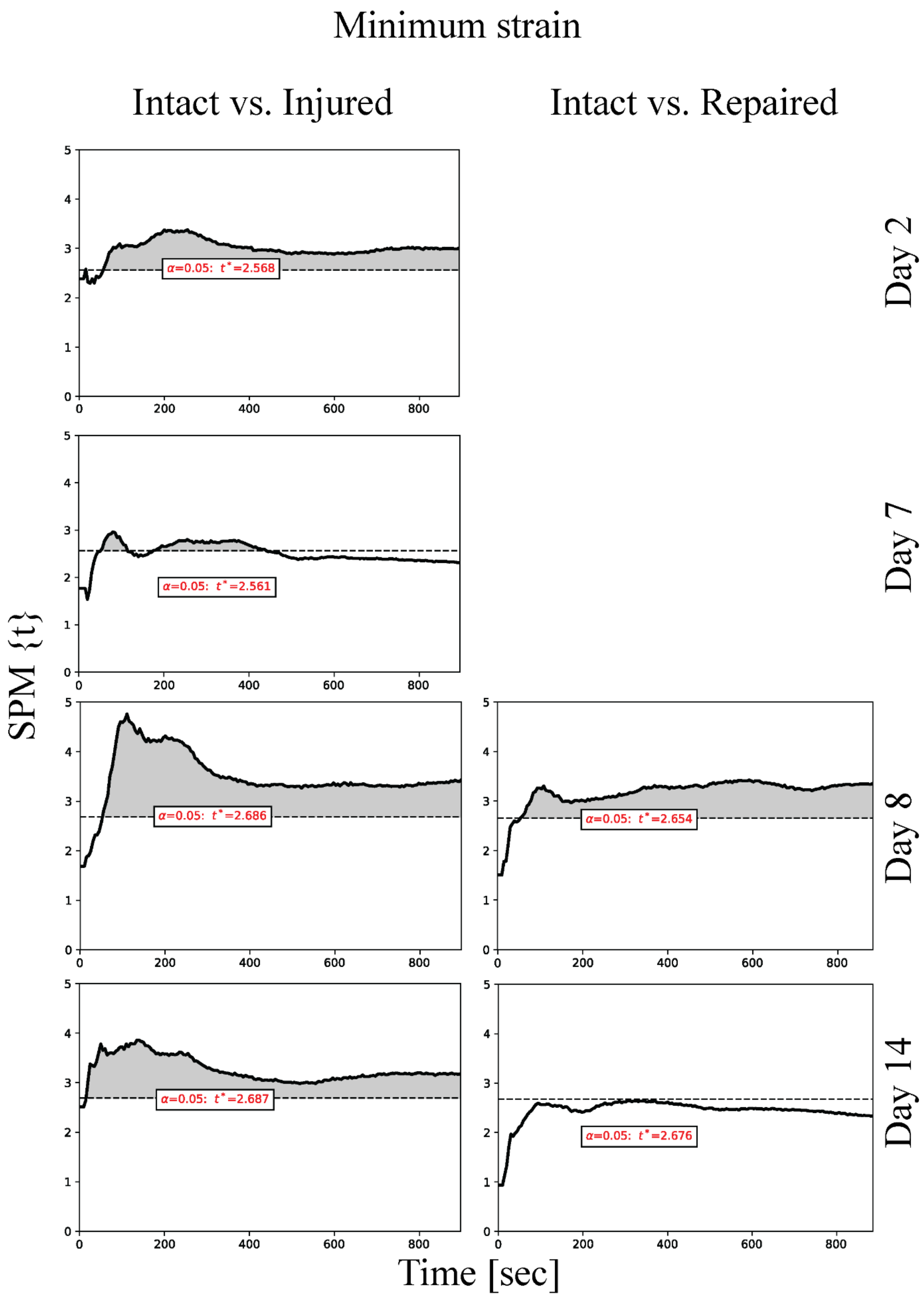

Figure 6-7: Independent two-sample t-test 1D analysis of the minimum strain measured during cyclic (0.2 Hz) compressive loading of the samples in intact, injured and repaired states processed using SPM1D software. The t values are plotted as function of time, with significance level ($p < 0.05$) denoted as a horizontal dotted line. n = 8

6.4.1.2: Mechanical evaluation of the repair strategy on the endplate delamination injury model

The glue penetrated into the scaffold and adhered well to the AF, as evidenced by blue colour of the scaffold and tight adhesion of the scaffold to the AF surface after multiple days of loading as seen in Figure 6-3. The adhesion of the FibGen to the AF was also successful, as all scaffolds (n=8) stayed attached to the AF surface after 5 days of diurnal and 2 days of high stress compressive loading. No tissue ingrowth or cellularization was observed in the scaffold or the hydrogel.

All modulus values were not statistically different for the intact, injured (delaminated) and repaired groups. The maximum strain reached during the cycle was also not statistically different for all groups. However, the minimum strain reached at every cycle, which is the strain at minimum stress of 0.02 MPa, was significantly higher for injured samples vs. intact throughout the whole experiment at all time-points as can be seen in Figure 6-7. The repaired sample also exhibited significantly higher minimum strain vs. intact the day after the repair procedure (day 8). After 14 days the minimum strain was not significantly different from the intact samples, which suggests restoration of mechanical properties.

6.4.2: Biological effect of endplate delamination injury and repair strategy

6.4.2.1: Cell viability

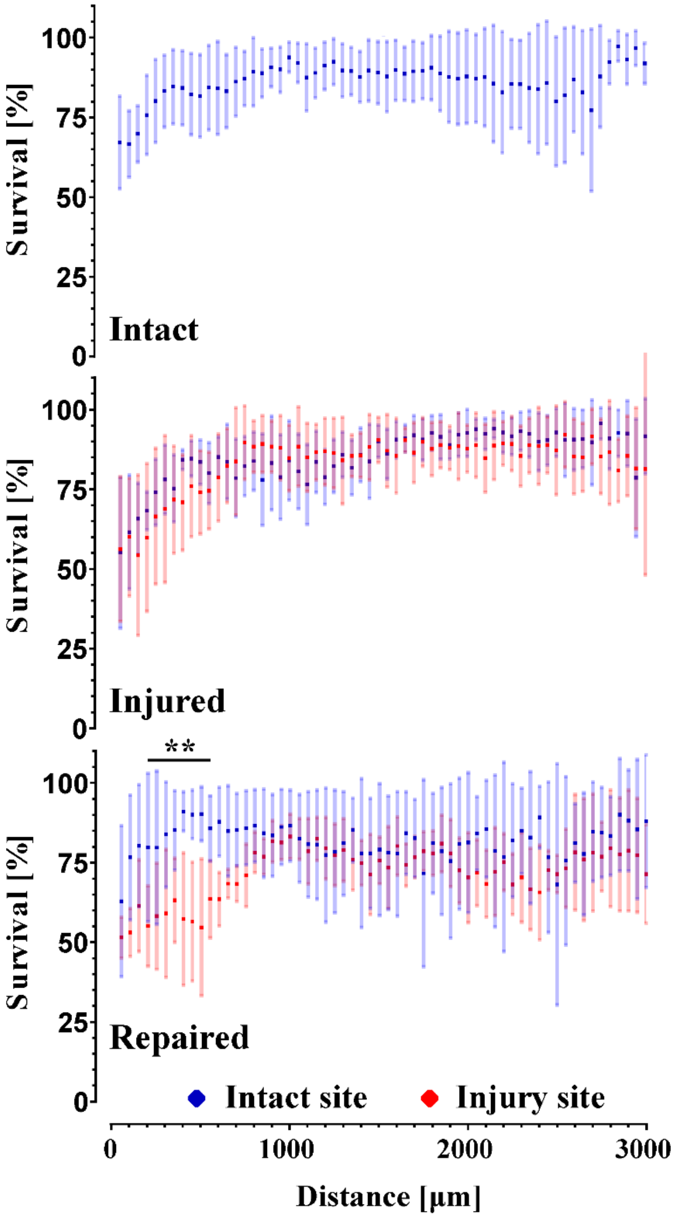

Figure 6-8: Graph of cell viability plotted as a function of distance from the surface of the IVD (in blue from the intact site , in red from the injured or repaired site) with error bars representing standard deviation. n = 6

Cell viability, which is affected by the ex vivo environment, injury as well as genipin toxicity, was assessed using LDH and DAPI stain on cryosections. The results presented as viability of the cells as function of distance from the edge of AF in bins of 50 µm are shown in Figure 6-8. It was found that the viability fraction did not differ significantly between the intact sides of all samples. The side that was damaged on the injured samples was not significantly different from the opposite intact site on the same samples, it was also not significantly different from the samples kept intact. However, the damaged side in repaired samples showed significantly lower viability from 100 to 600 µm away from the AF edge compared to the opposing undamaged side. It was also significantly different from the injured samples, as the repaired samples showed significantly lower viability from 450 to 750 µm. These findings suggest that the injury does not have a significant effect on cell viability, however the application of the FibGen glue and the scaffold leads to significantly lower cell viability up to 600 to 750 µm from the application site. Cell viability in the NP was above 90 % in all samples.

6.4.2.2: Gene expression

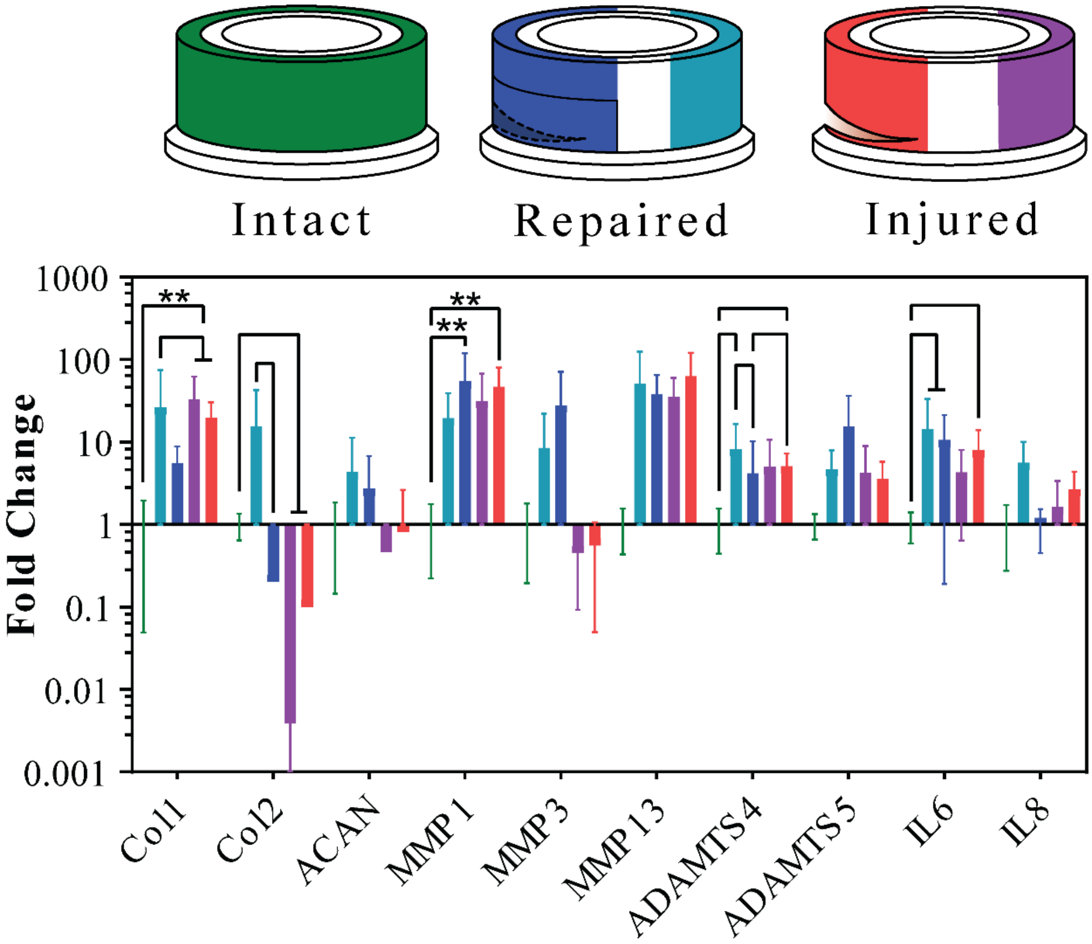

Figure 6-9: Results of the RNA quantification extracted from intact samples AF; injured samples AF near the injury site and AF from the opposite side of the injury site; repaired samples AF near the repair site and AF from the opposite side of the repair site. Error bars showing standard deviation, n = 4.

Gene expression of anabolic genes collagen type I [Col1] and type II [Col2] and aggrecan [ACAN], catabolic genes matrix metalloproteinase 1, 3 and 13 [MMP1, MMP3, MMP13], as well as ADAM metallopeptidase with thrombospondin type 1 motif4 and motif5 [ADAMTS4, ADAMTS5] and inflammatory genes interleukin 6 [IL6] and 8 [IL8] was determined from AF at the injury or repair site and intact (control) side, as shown in Figure 6-9. Anabolic genes showed a significant upregulation of Col1 in injured samples. A significant downregulation of Col2 was observed for injured samples at all AF sites, as well as downregulation at the repair site compared to the opposite for repaired samples. The catabolic gene MMP1 showed upregulation at injury and repair sites relative to the intact control. Furthermore, ADAMTS4 gene was upregulated in repaired control and injury site relative to the intact control. The repair site was downregulated relative to the injury and repair control. Finally, the inflammatory IL6 gene was upregulated in the whole AF of repaired sample and at the injury site relative to the intact control.

6.4.2.3: Nitric oxide and GAG medium assay

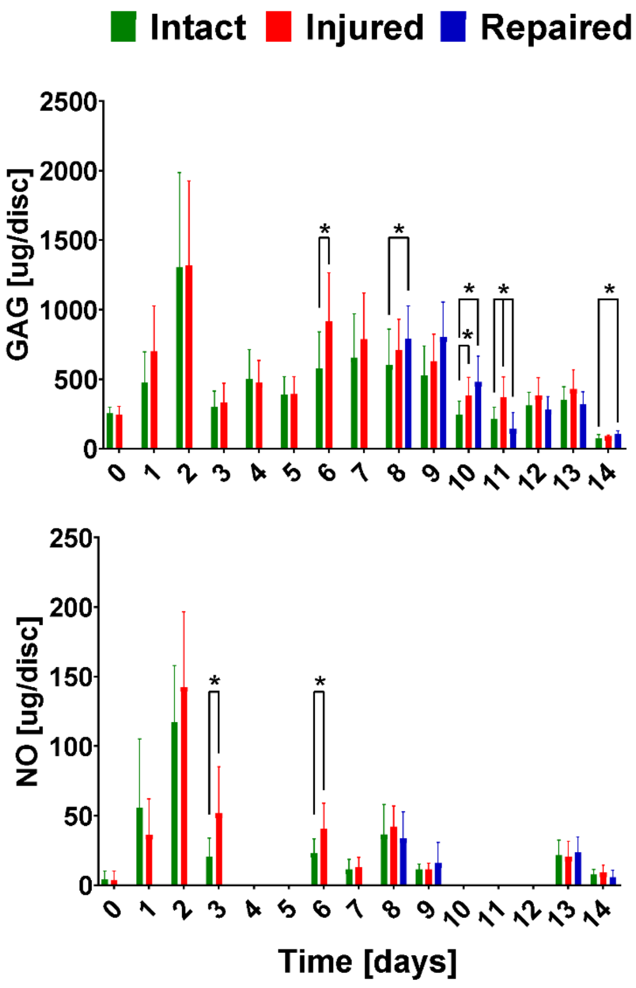

Figure 6-10: Graph of GAG and NO content per disc volume plotted as a function of time. HS underlines the measurements done after the IVDs were subjected to high stress mechanical testing. Error bars showing standard deviation. n = 8

The GAG and NO content of the medium was measured daily from samples taken before and directly after the loading cycles. The total amounts were calculated by combining the results from directly after the loading and the amount released into the medium during the overnight incubation. The NO and GAG amounts per disc as a function of time can be found in Figure 6-10. The overall GAG in the medium measured in µg per mm^3 of an IVD was significantly higher ($p < 0.05$) for injured samples (0.186 ± 0.103) compared to the intact (0.135 ± 0.080), there was no statistical difference between intact and repaired (0.136 ± 0.097) samples. At individual time points analyzed through t-tests, the repaired sample initially showed higher GAG content in medium than intact samples (days 8-10), however thereafter this observation was reversed, where the GAG content was significantly lower for repaired samples. The absolute NO values were low at all time points. The injured samples showed significantly higher levels after diurnal loading on days 3 and 6 compared to intact samples.

6.5: Discussion

6.5.1: Mechanical comparison of the central AF puncture and endplate delamination injury models

The injury mechanisms of the intervertebral disc have been investigated from both the mechanical and biological perspective in a variety of scenarios. However, the relevance of the injury models to clinical observations is rarely considered. In this study we attempted to replicate the case of endplate delamination, most commonly observed in peripheral AF failure based on the clinical description by Rajasekaran et al. [6] and Veres et al. [274]. To achieve this, a circumferential scalpel incision was successfully implemented as an analogue to fracture of AF at the endplate interface. When comparing Figure 6-1 (a, b and c) to the clinical description in literature, the morphological replication was successful, with injury at the interface of the AF and the endplate, and significant damage both in the AF and NP region.

The two injury models were expected to have different responses to the compressive loading as the geometry of the defect and its location was very different. Mechanical resistance in the IVD arises from the ability of the AF to resist tensile stresses imposed by the incompressible NP when compressive forces are applied to the spine [301,302]. Physical containment of the NP and mechanical performance of the AF are the two parameters dictating the stress strain response. The models investigated in this study are different in both those aspects. In the puncture model, the NP and AF are severely disturbed by the puncture as observed in Figure 6-1d and were able to immediately protrude from the injury site, while in case of the delamination injury, the NP was largely undisturbed, as seen in Figure 6-1 a and b. This outcome is clearly the result of the geometry of the injury. This means that in the delamination injury. the changes in mechanical properties are a direct result of alterations in the tissue mechanics in the

IVD, rather than a reduction in the amount tissue. This difference in geometry should also lead to a different effect on the mechanical performance of the AF. The delamination injury compromises a substantially larger number of AF fibres, compared to the puncture. In addition, it is important to note that the delamination injury scales with the IVD size unlike the puncture. In summary, the puncture injury would facilitate early NP herniation, while the delamination injury results in a much higher proportion of damage to AF. Severed tissue and NP herniation leads to an immediate initial impact on the mechanical properties. While a large delamination defect in the AF would likely not have an immediate effect, as no tissue is removed, the increased load on the NP and remaining AF would lead to increased degradation and mechanical damage to those tissues. The larger AF injury would likely also show greater differences from the intact state overall.

The two different damage models investigated in this study did not show a significant difference in mechanical response between the models or from the control that was kept intact. This is likely due to inter-sample variability (n=4) in conjunction with the small impact of the injuries on compressive mechanical behaviour. As ex vivo samples had to be kept alive for an extended period to evaluate the biological changes during ex vivo culture, and to provide mechanical response most similar to in vivo organs, the samples could not be embedded in a rigid mould at the vertebra. Such a procedure would limit nutrient access through the endplate and lead to degeneration. Therefore, only compressive loading was available for mechanical testing and diurnal loading protocols. More extensive differences between puncture and delamination model could have been observed through compressive loading with an angular component, as the failures at the annular-endplate occur more often when the load is applied with increasing flexion angle which causes tensile stresses, as documented by Veres et al.[274]. However, the results suggested that the delamination model has a potential to show increased maximum modulus and increased minimum strains after 7 days in the bioreactor. These observations are likely due to the collapse of the IVD during loading and at or near endplate-to-endplate contact in compression, which leads to an increased modulus relative to both the intact and punctured groups. The increase in minimum strain reflects the inability of the IVD to recover height quickly after load is released, likely due to increased hydraulic permeability as noted by Grunert et al.[279]. The delamination model was therefore chosen for the second phase of the study where the repair strategy would be investigated, as it showed potential for significantly different mechanical properties.

6.5.2: Mechanical and biological evaluation of the endplate delamination injury and repair strategy

The repair strategy designed around addressing the failures at the annular-endplate junction focused on three main goals: tight seal and adhesion to the injury site, restoration of the mechanical properties and cytocompatibility. The chosen approach comprised two components: electrospun PCL and FibGen hydrogel adhesive.

The overall design was based on a bioinspired composite like structure where the matrix component is a FibGen hydrogel reinforced with PCL electrospun scaffold. The FibGen hydrogel also acts as an adhesive component to the AF. The technique used for the application of the scaffolds relied on the interpenetration of the FibGen hydrogel and the PCL matrix, which was successfully achieved through soaking the scaffold in the thrombin-genipin component prior to application onto the AF surface covered in fibrinogen. The adhesion process took approximately 30 minutes under ambient conditions, which meant that the membrane needed to be mechanically fixed for this period. This was achieved through fixation with paraffin film wrapped tightly around the IVD for said period. This step is similar to the pressure the surrounding tissue would exert on the repair site in an in vivo scenario. It is considered acceptable to immobilize the patient for the required 30 minutes to avoid shifting the patch. Furthermore, in vivo the IVD would be under constant pressure, which would mean that there would be minimal changes in volume and shape to facilitate good adhesion. Overall the application process was sufficient, however if further optimization for in vivo implementation to reduce adhesion time is required it can be achieved through altering the FibGen formulation[292].

The mechanical response throughout this stage of the study was focused on testing the repair strategy, as shown in Figure 6-5 and 6, and therefore comprised three groups: control, injured group and repaired group, which was injured and then repaired illustrated in Figure 6-2. The focus was placed on establishing an injury model mechanically significantly different from the intact samples, and to achieve restoration of the mechanical properties through the repair procedure. Similarly, to the comparison of the injury models, the mechanical evaluation was limited to compressive loading due to biological considerations, preventing fixation at the vertebra. However, unlike the injury model investigation, significant differences were found for the minimum strain between the intact and injured samples. This measurement corresponds to the ability of the disc to recover height under load. This ability was significantly reduced for the injured samples at all time points. On the other hand, it was restored to the intact values for the repaired samples on day 14, which corresponds to 7 days after repair. This suggests that the full crosslinking process proceeds for more than 24 hours after the application. In particular, this finding could be a result of genipin crosslinking collagen in the AF matrix, which would lead to a stiffer and more elasticity in AF. The diffusion process required for the genipin to penetrate into the AF would slow down the reaction, unlike in the FibGen hydrogel where the components are liquid and the layer is thin compared to AF, as seen in Figure 6-3. The stiffening of the AF on genipin exposure is further supported by Fessel et al. [303], where increased stiffness was observed in collagen networks on application of genipin.

One limitation of comparing the biomechanics results in the current study to many other repair strategies that have been previously attempted in literature is the type of injury that is repaired. All studies that are cited here use various types of puncture injuries in the central AF. For small animal models a needle puncture is used or AF tissue removal for larger defects, for large animal models a biopsy punch is used or once again AF tissue is removed directly. As discussed in the comparison of the injury models, the commonly studied puncture injury likely has a different mechanical effect than the delamination injury. With that in mind, the minimum strain in this study can be considered analogous to the height loss of the IVDs post loading, which is commonly reported in literature. Many studies have recorded disc height loss after AF injury, and disc height is considered a benchmark for both degeneration and success of the repair strategy clinically [304]. The results in this study are in agreement with multiple studies that have shown successful repair of the injuries to the central AF in vivo [278,283,286–288]. Both in terms of significant height loss in injured IVDs and disc height restoration and improvement due to repair. These studies were done on small animal models, where the size of the defect is smaller and biomechanical requirements on the repair construct are much lower than in large animals. Pennicooke et al. [280] and Long et al. [284] who have attempted repair strategies on large animal models in vivo were unbale to show a significant improvement in disc height on repair.

The overall IVD modulus measurements in this study however did not show significant differences between groups. This finding is in agreement with study by Likhitpanichkul et al. [21], where no significant change in stiffness was also observed on a whole organ model of an IVD, although the injury and repair had different geometry than the present study.

The impact the injury and repair have on the cell viability was measured through LDH-based live/ dead staining. The injury was found to have no effect on cell viability after 14 days. However, there was a significant decrease in cell viability on all exposed surfaces of the organ relative to the bulk in all samples, which could mask any effect the injury would have on the tissue directly adjacent to the surface. The decrease in viability on the IVD surface is consistent with findings of Li et al. [261]. Genipin has a significantly negative effect on cell survival up to 750 µm from the application site. This finding is in agreement with many studies performed ex vivo [282,303,305], where genipin of similar concentration to the present study in combination or without DMSO showed a strong cytotoxic effect. The cytotoxicity findings were supported by studies done in vitro [291,292]. On the other hand, it is in contradiction with some previously published work which showed no effect on cell viability in ex vivo organ cultures [281] and in vivo [306], although the exact recipes for the FibGen hydrogel vary between the studies, as well as the geometry of the injury and the repair. The reasons for this disagreement most likely come from large variety of formulations and culture conditions used, as well as insufficient documentation of the exact absolute amount of both DMSO and genipin each cell is exposed to.

Although the toxic effect of genipin is never desirable, a compromise should be considered to provide a good mechanical support and seal on the damaged area in the absence of alternative adhesives with compatible mechanical properties. The specific mechanism by which genipin affects cells is not clear in this case, whether this is due to cytotoxicity or the environmental changes that genipin induces through crosslinking the collagen matrix. The first case is in contradiction with findings of

Likhitpanichkul et al. [281], where cell infiltration and no cytotoxicity was shown after 6 days in a bioreactor. If, however free genipin molecules are an issue, in vivo environment would provide more continuous motion and fluid exchange, which could potentially further reduce the effect of the genipin. This assumption is supported by in vivo study by Long et al. which showed no long term cytotoxic or inflammatory effect from genipin in ovine IVDs [306]. In the latter more likely case, the reinforcing effect would stand in direct contradiction with cell survival. To reduce the exposure of the bulk of AF to the genipin, FibGen could be allowed to gel briefly on the scaffold prior to application, hence reducing the amount of freely available genipin. The adhesive FibGen hydrogel can be substituted for a more biologically friendly material. Riboflavin crosslinked collagen hydrogels avoid the use of potentially toxic genipin as crosslinker and have been shown to promote cell infiltration and effectively seal AF defects in small animal models in vivo and restore some aspects of biomechanics [279,286,287]. Whether this approach can translate to large animal models is questionable as the biomechanical environment is far more sever. Further doubt is cast in work by Pennicooke et al., where the efficacy of such hydrogels in ovine in vivo model was investigated and found that while histologically the quality of the NP was improve, the biomechanics and disc height loss was not significantly different from the injured IVDs [280]. This is likely due to insufficient stiffness of the collagen hydrogels required for large animal models. FibGen shows compressive elastic modulus on the scale of 100-200 kPa [240], while high density collagen gels are an order of magnitude softer at approximately 3 kPa [307]. In addition, the need for UV light for crosslinking would not allow for the use of opaque electrospun membranes for resilience. Cyanoacrylate glues are widely used clinically, however the brittle nature of these glues coupled with potential toxicity concerns [308] would not give them an advantage over the use of FibGen. As such the compromise of using potentially toxic genipin as crosslinker has to be considered. An improved procedure minimizing tissue exposure to genipin and DMSO can provide the best possible outcome.

No cell infiltration into the scaffold was observed after 7 days in culture. The location of the repair as well as its geometry are likely the reasons for no observed infiltration in this study. In Figure 6-8 it can be seen that there is proportionally more live cells in inner regions of AF as opposed to the surface. Therefore, the application of the scaffold on the very outer surface of the AF in this study limits the cells access to the scaffold. Furthermore, FibGen is embedded in the electrospun fibre network with the porosity in the range of 1 µm, which is at the lower limit of porosity large enough to allow for cell infiltration. Even in the presence of cells, cell infiltration would be dependent on degradation and removal of FibGen to access the pores for proliferation. The migration of cells to the surface of the AF and degradation of FibGen would take longer than 7 days assessed in this study. A study by Likhitpanichkul et al. [21] observed cell infiltration into FibGen hydrogel after 6 days in a bioreactor on a large animal model with a central AF defect. However, unlike in this study, FibGen hydrogel as a large mass was implanted into a defect in the central AF bordering NP. In addition, the hydrogel did not contain a secondary network. Access to the large cell population present in the inner AF, was likely the main cause for the observed difference in cell proliferation.

As discussed, genipin can have a negative effect on cell survival overall. To improve the promote AF injury healing and remodelling live cells can be added to the FibGen hydrogel. Several studies have shown promising results with ECM generation and proliferation of cells embedded in both FibGen and crosslinked collagen hydrogels [89,285–287] applied to AF defects. The repair approach has shown a restoration of mechanical properties in this study, to further enhance the efficacy of the repair, especially in the long term, adding live cells to the to the repair construct can be considered. There is conflicting evidence regarding cell survival in genipin rich environment, as discussed previously. The proposed repair strategy would need to be tuned to ensure good cell survival, proliferation and functioning by potentially increasing the pore size of the electrospun membrane and adjusting FibGen composition and application process. Likhitpanichkul et al. have shown cell infiltration into FibGen hydrogel when applied to AF defect [281], it is therefore likely that such an approach is possible. On the other hand, it is unclear whether cell loading would be beneficial in this injury model as the repair is applied to the outside layers of AF only, and there is no tissue that is removed or herniated. Once the injury is tightly sealed and the IVD is once again loaded, the separated AF layers are put in contact again, therefore no hydrogel filler is necessary, and repair can proceed through the existing cells in the AF.

Cellular response to the injury and repair that was assessed through mRNA expression at the AF injury site and in the AF opposite the injury site; in addition, GAG and NO levels in the medium were measured. The upregulation of Col1 in injured samples, is consistent with trend observed by Frauchiger et al., although the results there were not significant [282]. The downregulation of Col2 in injured samples is also consistent Pirvu et al. [89], it was also documented as part of degenerative process without inducing an injury by Lang et al. [296]. Very large and significant upregulation of MMP1, ADAMTS4 and a trend of upregulation of MMP13 in the AF of the repaired and injured samples at the injury site was not consistent with previous studies, where downregulation of catabolic genes was observed with diurnal loading [89,282]. As most markers (anabolic and catabolic) were up regulated in the AF, this may be related to a response to the injury of repair and remodelling of extracellular matrix in the AF.

The GAG content measured in the medium showed a higher value in injured samples compared to intact ones at most time points. This is likely due to increased surface area and ECM breakdown/ remodelling in the injury group. The repaired samples showed a significantly lower amount of GAG content in the medium than the injured samples 3 days after repair. This further supports the idea that the full reaction and sealing of the defect happens slowly after the initial setting and adhesion of the hydrogel. The levels of NO found in the media, which were higher for injured samples than other groups are in agreement with previous work done by Likhitpanichkul et al. [281]

6.5.3: Limitations of the study

The chosen ex vivo bovine IVD from the tail model used in this study has limitations in terms of transfer to in vivo human clinical applications. Further in vivo experiments on large animal model are required to optimize the application procedure and confirm its viability. The mechanical properties and size are similar between the human and bovine IVDs [242]. However, biologically the tissue compositions as well as cell types vary significantly between the two models [243]. In particular, discs extracted from the tails of calves in this study are likely most representative of IVDs from healthy young humans.

The delamination model does not address the NP herniation and potential further tissue degeneration of the AF and NP. This limitation arises due to the nature of the injury being surgical rather than induced through degeneration of loading to failure. Therefore, it is representative of early stages of AF tare at the endplate. The repair in the presented form would need to be applied soon after the injury occurs and would likely not be suitable for severely degenerated discs, as it requires relatively healthy AF of adhere to for mechanical stability. In the future it would be possible to explore injuries induced through flexural tensile loading of the disc, which is most likely to lead to delamination of the AF at the endplate [274,309,310]. To assess the degenerative effects of the injury a much longer ex vivo study is required likely involving alterations in the IVD culture to induce degenerative changes mechanically or chemically [296].

6.6: Conclusion

AF rupture is a common condition that can lead to severe pain and reduction in mobility. A new injury model similar to failure of the AF at the endplate junction was investigated and was found to be mechanically not significantly different from previously described rupture of the AF in compressive loading. A repair strategy utilizing electrospun PCL scaffold and FibGen adhesive was investigated through a long-term ex vivo biomechanical testing protocol. The repair strategy showed a promising restoration of mechanical properties to the levels found in intact IVDs, while FibGen adhesive showed limited cytotoxicity in the AF. In addition, the adhesion of the scaffold to the injury site had a good seal and remained intact throughout the procedure. Individual components of the repair were not tested separately, hence their specific contributions to the restoration are not reported. Furthermore, the degradation rates of the components may be significantly different and require further tuning. The application technique used in this study may not be suitable for in vivo procedure and may require further optimization. As such, to conclusively define the efficacy and biocompatibility of the proposed approach an in vivo study would be required in the future.

Chapter 7: Synthesis

7.1: Summary & conclusion

Lower back pain (LBP) is a major cause of disability and concern for healthcare systems worldwide. The proportion of the population whose major cause of disability is reported as lower back pain has increased significantly in the last decades[311], likely as a result of increasing changes in lifestyle, particularly in high-income and western countries. The prevalence of LBP was 7.3 % globally in 2015, which translates to 540 million people[311]. The causes of LBP are poorly understood due to a their varied nature[312]. The intervertebral disc (IVD) plays a crucial role in determining the health of the spine because it is a crucial biomechanical component of the spinal column as well as its physical proximity to the major nerve bundles. Although the exact proportion of the IVD injury as a cause of LBP is unknown, it is identified as a condition often present in patients with LBP[313]. There are multiple modes of failure of the IVD which are the result of mechanical injury, biological degradation or more commonly both. Disc bulging or protrusion were found were found in 42 to 43 % of cases, with extrusion present in 7 %. This occurrence was only overshadowed by general disc degeneration present in 57% of cases[314]. While the prevalence of the injury increases significantly with age, there is still a significant number of cases before 25 years of age[311]. The work presented in this thesis focuses on failure of the annulus fibrosus (AF), the outer layers of the IVD, which leads to the protrusion and bulging of the IVD, and therefore constitutes a serious financial and quality of life burden on both the society as a whole and afflicted individuals.

In this thesis the main aim was to develop a mechanically biocompatible implant for AF repair. The design of the repair focused on an approach that would allow a minimally invasive procedure, where the repair construct could be applied and immediately provide mechanical stability, close the defect in the AF and allow the synthesis of the extracellular matrix (ECM) to restore the original function of the injured tissue in the long term.

To achieve these objectives a composite approach of an electrospun network and hydrogel adhesive was chosen. The use of electrospun polymers results in a non-woven fibrous material with a morphology and scale similar to that of the native ECM, while maintaining design freedom to select the material, surface treatment and tune morphology to suit the application. These aspects were crucial to successful formulation of the repair strategy as the final construct needed to meet the biological and mechanical compatibility requirements outlined above.

Early in the project, poly(ε-caprolactone) (PCL) was chosen to be electrospun for the application, because it is FDA approved for use in surgical implants [315], is easily electrospun and a large body of literature available on electrospinning PCL.

In the first part of the project the design objective space of the scaffold was explored. Several gaps in knowledge were identified and addressed concerning electrospun PCL scaffolds. The microscale behaviour relevant for the cellular environment was investigated using a novel testing technique for single electrospun fibres. In addition, long term mechanical and material competence of electrospun PCL scaffolds exposed to an in vitro simulated physiological environment over a period of 6 month was assessed. These studies also allowed to define the strategy for design optimization for the intended application.

Following the characterization of the electrospun PCL scaffold and development of an in depth understanding of the electrospinning process overall, as well as the specifics pertaining to PCL electrospinning, work on defining the requirements and the final design of the repair was initiated.

7.1.1: Investigation into the mechanical properties of the electrospun poly(ε-caprolactone) scaffolds

The first achievement of this thesis is to establish a testing methodology for single electrospun fibres, that allows to carry out mechanical testing under biomechanically relevant loading conditions, which are characterized by large strains and cyclic loading. The newly developed method had two main advantages over pre-existing methods. Firstly, once the fibres were collected into the designed holders, they were easy to manipulate and observe before during and after testing, which allowed for a robust and reproducible methodology. Secondly the mechanical loading setup allowed for precise force and strain measurement with multiple loading cycles and large strains, using the FemtoTools MEMS-based nanoindenters[316]. In biomedical applications the electrospun scaffolds used in tissue engineering and regenerative medicine are often subjected to large repeated strains, which means that the repetitive loading protocol of this testing method provide tensile mechanical values for electrospun single fibres that are most relevant for biomedical applications. The method was applied to test single electrospun PCL fibres in a wide range of diameters from 0.4 to 7.0 µm. Overall, the findings on the relationship between fibre diameter and modulus of the fibres in this study agreed with previously published work on other electrospun polymer materials[168,172]. The overall behaviour of the fibres on the first loading cycle was also in line with what has been recorded previously. The results from this study showed that electrospun PCL has a significant plastic character on the first loading cycle, however following multiple consecutive loading cycles a trend towards a viscoelastic steady state could be observed. In addition, the fibres showed a high resilience up to 35 %

strain. These findings were important in the scope of the intended application of AF repair, as such an application would require a material with a high resilience and preferably elastic response in a high strain environment. Furthermore, these experiments with close observation of the single fibres both optically and using scanning electron microscopy (SEM) highlighted the importance of a high-quality electrospinning process to allow the production of fibres and scaffolds with adequate and consistent elastic properties. If many defects are present in the underlying fibres, such as diameter variations and surface defects, the mechanical response can be unreliable. The ability to observe the resulting fibres was paramount in understanding the electrospinning parameters that lead to high quality fibres in a broad range of fibre diameters.

The methods for performing cyclic mechanical test on single electrospun fibres were implemented in a work on poly(l-lactide) electrospun fibres by Morel et al.[191]. The method allowed to test fibres at strains that are inaccessible using other methods, such as AFM. The researchers in this study observed a similar relationship between the fibre diameter and Young's modulus for poly(l-lactide), that was found in this work for PCL.

In the second study, based on the electrospinning parameters defined in the first study, three potential scaffolds that could be used in the AF repair were identified. These scaffolds possessed fibres of diameters relevant for the intended application of AF repair and were to be used in all following studies in this project. A significant novel contribution of this thesis was to characterise the mechanical performance of electrospun PCL scaffolds in in vitro like conditions over a period of up to 6 months. A gap in the literature was identified, concerning the long-term mechanical characterisation and degradation under in vitro conditions of electrospun PCL membranes of varied fibre diameters between 1.5 and 6.0 µm. Firstly, there were no studies addressing electrospun membranes made up of large fibre diameters above 3.0 µm. Secondly, the mechanical characterisation was often limited to a single loading cycle, which is insufficient for biomechanical applications. In addition, a project wide need to test the reproducibility of the electrospinning method and its ability to produce membranes with homogeneous and high-quality fibres needed to be tested. As was identified in the first study, the quality of the fibres would severely affect their overall performance. There are inconsistent observations in literature concerning the outcome of in vitro exposure of PCL membranes, however the overall consensus tends towards no mass loss due to degradation and an initial increase of modulus due to increasing crystallinity. As highlighted in previous work, PCL degrades in 2 to 3 years in vivo [317], it is therefore not surprising that in vitro after 6 months the changes were not significant. Overall, the study provided valuable data on the mechanical changes that electrospun PCL membranes undergo in vitro, in a loading scenario that is relevant for the application requirements, as spontaneous disc healing is anticipated to progress within 6 months with scaffold support. It was especially important to confirm that the resilience of the membranes is in line with the requirements of the AF, which are in the range of 40 % strain at 1-2 Hz [238,241], before proceeding with the final design. The membranes with fibre diameters of 1.6 and 3.31 µm showed no breakage at all timepoints up to 150 % strain and recovery conservatively up to 20 % with preconditioning. These values were promising, as it meant that most strains can be accommodated in the recoverable region, and even in the event of extreme strains up to 40%, the damaged area will remain sealed. After tuning the electrospinning parameters for bulk production, the membranes produced had reproducible properties morphologically and mechanically. These results allowed to progress the project to the next stage where the membranes were used as a basis for the design of the overall repair strategy.

7.1.2: Design and proof of concept of the repair strategy for the failure of the annulus fibrosus

Once a sufficient understanding of the mechanics at both the microscopic and macroscopic level relevant to the application of AF repair was reached, methods for bulk reproducible production of the membranes were optimized and the competence of the membranes for the task were confirmed, the design of the overall repair construct and application process could proceed. In the third study, an attempt was made to define an efficient method of testing the repair procedure on an in vitro IVD model. To achieve this, several concepts for a IDV surrogate were investigated made up of readily available materials to replicate the major load bearing tissues in an IVD such as AF, NP and endplates. The approach of creating a practical synthetic model is necessarily faced with severe limitations as the mechanical response of the native IVDs is complex [300] and dependant on many environmental parameters. Aspects of the mechanical properties of an ex vivo bovine IVD [289], taken as a gold standard, could be replicated. It was possible to achieve similar torsional and compressive modulus, while maintaining similar dimensions of the synthetic tissues to the ex vivo counterpart. However, the number of limitations and deviations from the ex vivo and in vivo conditions led to the conclusion that an ex vivo model is more practical. In a sub-study, the surface strains of scaffolds applied on the synthetic IVDs were investigated, which lead to further understanding of the relationship of membrane stiffness, dimensions and buckling behaviour under compressive loading of the model, which needed to be taken into account in the final design. The approach of using 3D optical image correlation method based on conventional cameras, had severe limitations in terms of its applicability on very rough and surfaces with large overall curvature. Previous research has reported improved surface measurement accuracy of the IVD using a rotating mount for the stereo cameras[262], as well as using 2D laser albeit at severely reduced resolution[181,263].

A clinically relevant delamination of the AF at the endplate injury model was established and characterized on an ex vivo model in a bioreactor environment. This was the first study done to characterize this kind of damage to the AF, which authors believe to be more clinically relevant[6] than the well-established puncture to the central AF. The model showed promising mechanical differences form the uninjured IVDs and was morphologically like the injuries observed clinically. The new delamination model however lacked ovulation of the NP, which has been demonstrated on the central puncture model[282,283].

As a culmination of the work done in this thesis, utilizing all the knowledge gained in the previous studies, a novel repair strategy was devised and evaluate to repair AF injury which comprised an electrospun PCL membrane and a hydrogel glue. The repair strategy was tested on ex vivo bovine IVDs which were deemed the most suitable model based on the previous work. Building on the knowledge from the previous studies electrospun PCL membranes with a fibre diameter of 3 µm were chosen as possessing relevant modulus values, as well as not showing significant buckling during loading of the IVD, while having porosity that could potentially allow cell infiltration. The fibrinogen-genipin hydrogel glue was chosen based on promising results in literature that pointed to high adhesion strength, fast gelation and potentially low cytotoxicity [239,291]. Two injury models were proposed. A puncture to the central AF region commonly described in literature [261,275,276], and a unique circumferential AF delamination at the endplate [6]. AF delamination at the endplate showed a promising trend in terms mechanical difference in compression relative to the intact IVDs. This model was then utilized as an injury model to test the repair strategy. The focus of the repair procedure design was placed on practical feasibility and simplicity of the application, as to ensure maximum probability of the in vivo successes not only biomechanically, but also in terms of the surgical procedure. The electrospun networks are robust and easy to handle, the networks can be folded and unfolded for minimally invasive surgery procedures. The FibGen glue can be easily applied in multitude of ways, which already exist for other two component glues used surgically [318,319]. Alternative strategies exist that utilise cell loaded scaffolds, tissue engineered constructs or hydrogels. These approaches often lack robustness compared to the proposed repair but have the advantage of being potentially more advanced in their biocompatibility aspects. The study showed an improvement in IVD height in the unloaded state when the repair was applied compared to the injured samples. The novel use of SPM1D statistics package allowed to analyse and compare all loading cycles during the mechanical testing of the samples. This method provided a robust assessment of the mechanical response, without relying on achieving steady state behaviour. The FibGen glue showed limited cytotoxicity. Unlike the electrospun scaffold, FibGen was not mechanically characterized by itself in house prior to its use on the ex vivo model, because its performance can only be assed as an interstitial glue in conjunction with the membrane. The benefits of using FibGen and application procedure need to be better optimized to provide a conclusive recommendation on its use.

In conclusion the repair strategy showed a promising mechanical performance and limited cytotoxicity in an ex vivo bovine IVD model. The groundwork that was done in the first three studies resulted in mechanically sound strategy, that performed very well in adhesion and mechanical resilience. These results hold promise, but also open many additional questions before the repair can be applied in vivo.

7.2: Limitations of this work

In order to interpret the results presented in this thesis and utilise them in the further work, limitations of the methods and analysis need to be considered. In general, there are two main considerations. The presented techniques for mechanical evaluation of electrospun scaffolds have limitations in how the results can be interpreted overall and applied in an in vivo scenario. While the repair strategy leaves open questions in its long-term in vivo performance.

7.2.1: Material and environmental parameters of electrospinning

There are several literature studies presented in this thesis where electrospun scaffolds made up of PCL are characterized. While the authors attempt to provide information on all of the parameters of the material selection, storage and processing, there are always additional considerations that cannot be controlled or recorded, and their effect can be poorly understood. For the electrospinning process, there exists a convention in literature for reporting process parameters, that is not necessarily complete. For example, atmospheric pressure is not reported, although that could affect solvent evaporation. The field strength during electrospinning is not measured, but rather inferred from the voltages. This is however largely dependent on source and collector geometry. Therefore, all parameters that work in conjunction to produce a desired electrospun membrane that are reported in the studies are strictly equipment specific and would need to be significantly tuned to be replicated on a different setup. The virgin PCL that was used in the studies varies slightly from batch to batch from the manufacturer and degrades over time in storage. While these differences and changes are small, the cumulative effect is not quantified in these studies, and it could potentially have a significant effect on the material characterization results presented in the thesis.

7.2.2: Cyclic loading of electrospun single fibres and membranes

The mechanical characterization of the electrospun PCL scaffolds and single fibres in this thesis was strictly in the scope of the application. The choice of loading strains, rates and the number of cycles was done with the application in mind, and largely influenced by the ability to compare the obtained values with the native tissues. The electrospun networks show a complex mechanical behaviour resulting from an interplay of microstructure and material properties [83]. Therefore, the mechanics of the scaffolds are not characterized in a comprehensive way that would allow to conclusively infer the underlying mechanisms that lead to the observed mechanical response. The observations are also not readily extrapolated to different loading scenarios, where the testing parameters lie outside of the conditions investigated in this thesis.

The mechanical testing of the membranes and single fibres was performed under ambient conditions. This, of course, not the case in vivo. Therefore, it is difficult to interpolate these results to the in vivo scenario where the polymer exhibits a different response at body temperature, interstices are filled with liquid, the ionic content of the liquid is varied, and there is potentially a significant degree of reactive cellular activity. In addition, in case of the repair strategy utilized in this study, the membranes were embedded in a relatively stiff FibGen hydrogel, which meant that the microstructural deformation of the membranes under load was likely significantly altered, compared to the observations in the first two studies. However, the attempts to investigate the response of the membranes to deformation under similar conditions in a more controlled and easily replicated synthetic in vitro model were not able to satisfactorily replicate IVD response, as described in the third study.

7.2.3: The repair strategy

Overall, this work is limited by its choice of basic design and material. Using an electrospun PCL membrane with a hydrogel glue to repair AF injuries is only one of many possible approaches both in terms of overall strategy as well a specific morphology of the repair. In addition, PCL is also only one of the possible polymers that can be successfully electrospun for the application. Other studies have utilized PCL/poly(ethylene oxide) composites [195], silk [282], collagen[320], PGA/PLA [250], and many others [321]. Each material comes with its specific advantages and disadvantages. It is therefore not possible to conclude from this thesis that the proposed repair is the best possible approach.

The ex vivo experiments performed in the last study are of significant value as limitations of testing the repair under ambient conditions are improved upon. However, it is still not fully representative of the in vivo environment in large animals, or for that matter in humans. The injury that is induced ex vivo, is biomechanically and biologically inconsistent with the in vivo counterpart. While it shares morphological characteristics and potentially induces a similar mechanical damage, it is only vaguely representative of a degenerated or ruptured disc observed clinically. These limitations are extensively discussed in the study itself. To contextualize the ex vivo models and these limitations the biomechanics of a ruptured human IVD need to be quantified. Intact healthy discs are well studied [289], however to date the authors are unaware of any literature where the mechanical properties of an naturally ruptured human IVD are described outside of height loss[322].

7.3: Outlook

The limitations of the studies presented in this thesis largely inform the outlook and further work that needs to be done to both better understand the design principles of the proposed repair and guarantee success of the proposed strategy in a clinical scenario.

The basic elements of the repair can be further iterated to improve their performance. There are alternatives to FibGen glue that can be used, which can potentially have lower toxicity. Alternate application methods could be developed to reduce exposure of the tissues to the free genipin and DMSO. PCL can be replaced with polymer that has a higher elastic range. The electrospun networks can be made anisotropic to mimic the mechanical properties of the AF more closely. These incremental advances are important, and cumulatively will likely lead to much improved outcomes. One of the open questions that remains unanswered, and casts doubt on the whole approach rather than its overall performance, is the degradation of PCL and FibGen. In the PCL degradation study, no timeline for when the electrospun membrane might degrade could be established. Other studies performed in vivo have suggested periods of up to 18 month until the material loses mechanical function[209]. FibGen itself will likely degrade much faster with significant impact on the geometry observed between 3 and 8 weeks[281]. These values need to be confirmed in the case specific scenario and aligned to ensure consistent implant performance. The true degradation rate must also be balanced against the potential for tissue regeneration. Overall, a long-term ex vivo investigation into the mechanical performance of the repair strategy would be beneficial before moving onto in vivo testing. These tests could last up to 3 weeks in a bioreactor environment and allow a more comprehensive timeline of the implant’s performance with multiple timepoints.

Following this optimization step, in vivo experiments can be performed on large animals. To define the procedures for the in vivo test, the application process needs to be refined with surgical procedures in mind. The use of a soft membrane in combination with a glue is ideally suited for minimally invasive surgery. Several procedures with similar strategies have been described in literature already[323,324]. Ensuring that the glue composition and tooling is adequate for the in vivo application would be important for progressing into clinical applications.

Bibliography

1. van Tulder, M., Malmivaara, A., Esmail, R. & Koes, B. Exercise Therapy for Low Back Pain: A Systematic Review Within the Framework of the Cochrane Collaboration Back Review Group. *Spine (Phila. Pa. 1976).* **25**, 2784–2796 (2000).
2. Koes, B. W., van Tulder, M. W. & Thomas, S. Diagnosis and treatment of low back pain. *BMJ* **332**, 1430–1434 (2006).
3. Jeffries, L. J., Milanese, S. F. & Grimmer-Somers, K. A. Epidemiology of adolescent spinal pain: A systematic overview of the research literature. *Spine (Phila. Pa. 1976).* **32**, 2630–2637 (2007).
4. Van Tulder, M. *et al.* Chapter 3: European guidelines for the management of acute nonspecific low back pain in primary care. *Eur. Spine J.* **15**, 169–191 (2006).
5. Walker, M. T., Spitzer, E. M., Veeramani, M. & Russell, E. J. *Pain-Generating Degenerative Pathologies of the Spine*. *Essentials of Pain Medicine* (Elsevier Inc., 2019). doi:10.1016/B978-1-4377-2242-0/00018-3.
6. Rajasekaran, S., Bajaj, N., Tubaki, V., Kanna, R. M. & Shetty, A. P. ISSLS prize winner: The anatomy of failure in lumbar disc herniation: An in vivo, multimodal, prospective study of 181 subjects. *Spine (Phila. Pa. 1976).* **38**, 1491–1500 (2013).
7. Aoki, Y. *et al.* Nerve fiber ingrowth into scar tissue formed following nucleus pulposus extrusion in the rabbit anular-puncture disc degeneration model: Effects of depth of puncture. *Spine (Phila. Pa. 1976).* **31**, 774–780 (2006).
8. Melrose, J., Roberts, S., Smith, S., Menage, J. & Ghosh, P. Increased nerve and blood vessel ingrowth associated with proteoglycan depletion in an ovine anular lesion model of experimental disc degeneration. *Spine (Phila. Pa. 1976).* **27**, 1278–1285 (2002).
9. Freemont, A. *et al.* Nerve ingrowth into diseased intervertebral disc in chronic back pain. *Lancet* **350**, 178–181 (1997).
10. Ghosh, P. *The Biology of the Intervertebral Disc*. (CRC Press, 1988).
11. Bogduk, N. *Clinical anatomy of the lumbar spine and sacrum*. (Elsevier Health

Sciences, 2005).

12. Humzah, M. D. & Soames, R. W. Human Intervertebral Disc: Structure and Function. **356**, 337–356 (1988).
13. Adams, M. A. & Roughley, P. J. What is intervertebral disc degeneration, and what causes it? *Spine (Phila. Pa. 1976).* **31**, 2151–2161 (2006).
14. Antoniou, J. *et al.* The Human Lumbar Intervertebral Disc. *Society* **98**, 996–1003 (1996).
15. Buckwalter, J. A. Aging and Degeneration of the Human Intervertebral Disc. *Spine (Phila. Pa. 1976).* **20**, 1307–1314 (1995).
16. Iatridis, J. C., Weidenbaum, M., Setton, L. A. & Mow, V. C. Is the Nucleus Pulposus a Solid or a Fluid? Mechanical Behaviors of the Nucleus Pulposus of the Human Intervertebral Disc. *Spine (Phila. Pa. 1976).* **21**, 1174–1184 (1996).
17. McDevitt, C. A. Proteoglycans of the intervertebral disc. *Biol. Intervertebral Disc. Boca Raton, Fla* (1988).
18. Adams, P., Eyre, D. R. & Muir, H. Biochemical aspects of development and ageing of human lumbar intervertebral discs. *Rheumatology* **16**, 22–29 (1977).
19. Mikawa, Y., Hamagami, H., Shikata, J. & Yamamuro, T. Elastin in the human intervertebral disk - A histological and biochemical study comparing it with elastin in the human yellow ligament. *Arch. Orthop. Trauma. Surg.* **105**, 343–349 (1986).
20. Yu, J., Fairbank, J. C. T., Roberts, S. & Urban, J. P. G. The elastic fiber network of the anulus fibrosus of the normal and scoliotic human intervertebral disc. *Spine (Phila. Pa. 1976).* **30**, 1815–1820 (2005).
21. Eyre, D. Collagens of the disc. *Biol.* (1988).
22. Inoue, H. & Takeda, T. Three-dimensional observation of collagen framework of lumbar intervertebral discs. *Acta Orthop.* **46**, 949–956 (1975).
23. Cassidy, J. J., Hiltner, A. & Baer, E. Hierarchical structure of the intervertebral disc. *Connect. Tissue Res.* **23**, 75–88 (1989).
24. Marchand, F. & Ahmed, A. M. Investigation of the laminate structure of lumbar disc anulus fibrosus. *Spine (Phila. Pa. 1976).* **15**, 402–410 (1990).
25. Horton, W. G. FURTHER OBSERVATIONS ON THE ELASTIC MECHANISM OF THE INTERVERTEBRAL DISC. *J. Bone Joint Surg. Br.* **40-B**, 552–557 (1958).

26. Hsu, E. W. & Setton, L. A. Diffusion tensor microscopy of the intervertebral disc anulus fibrosus. *Magn. Reson. Med.* **41**, 992–999 (1999).

27. Pooni, J. S., Hukins, D. W. L., Harris, P. F., Hilton, R. C. & Davies, K. E. Comparison of the structure of human intervertebral discs in the cervical, thoracic and lumbar regions of the spine. *Surg. Radiol. Anat.* **8**, 175–182 (1986).

28. Adam, C., Rouch, P. & Skalli, W. Inter-lamellar shear resistance confers compressive stiffness in the intervertebral disc: An image-based modelling study on the bovine caudal disc. *J. Biomech.* **48**, 4303–4308 (2015).

29. Melrose, J., Smith, S. M., Appleyard, R. C. & Little, C. B. Aggrecan, versican and type VI collagen are components of annular translamellar crossbridges in the intervertebral disc. *Eur. Spine J.* **17**, 314–324 (2008).

30. Pezowicz, C. A., Robertson, P. A. & Broom, N. D. The structural basis of interlamellar cohesion in the intervertebral disc wall. *J. Anat.* **208**, 317–330 (2006).

31. Schollum, M. L., Robertson, P. A. & Broom, N. D. ISSLS prize winner: microstructure and mechanical disruption of the lumbar disc annulus: part I: a microscopic investigation of the translamellar bridging network. *Spine (Phila. Pa. 1976).* **33**, 2702–2710 (2008).

32. Yu, J. *et al.* Microfibrils, elastin fibres and collagen fibres in the human intervertebral disc and bovine tail disc. *J. Anat.* **210**, 460–471 (2007).

33. Wade, K. R., Robertson, P. A. & Broom, N. D. On the extent and nature of nucleus-annulus integration. *Spine (Phila. Pa. 1976).* **37**, 1826–1833 (2012).

34. Andersson, G. B. J. Epidemiological features of chronic low-back pain. *Lancet* **354**, 581–585 (1999).

35. Urban, J. P. G. & Roberts, S. Degeneration of the intervertebral disc. *Arthritis Res. Ther.* **5**, 120–130 (2003).

36. O'Halloran, D. M. & Pandit, A. S. Tissue-engineering approach to regenerating the intervertebral disc. *Tissue Eng.* **13**, 1927–1954 (2007).

37. ANDERSSON, G. B. J. Epidemiologic Aspects on Low-Back Pain in Industry. *Spine (Phila. Pa. 1976).* **6**, (1981).

38. Borenstein, D. G. Epidemiology, etiology, diagnostic evaluation, and treatment of low back pain. *Curr. Opin. Rheumatol.* **13**, (2001).

39. Ala-Kokko, L. Genetic risk factors for lumbar disc disease. *Ann. Med.* **34**, 42–47

(2002).

40. Simmons, E. D., Guntupalli, M., Kowalski, J. M., Braun, F. & Seidel, T. Familial Predisposition for Degenerative Disc Disease. *Spine (Phila. Pa. 1976).* **21**, 1527–1529 (1996).

41. Lotz, J. C. & Chin, J. R. Intervertebral Disc Cell Death Is Dependent on the Magnitude and Duration of Spinal Loading. *Spine (Phila. Pa. 1976).* **25**, 1477–1483 (2000).

42. Lotz, J. C., Colliou, O. K., Chin, J. R., Duncan, N. A. & Liebenberg, E. 1998 Volvo Award Winner in Biomechanical Studies. *Spine (Phila. Pa. 1976).* **23**, 2493–2506 (1998).

43. Paul, C. P. L. *et al.* Static axial overloading primes lumbar caprine intervertebral discs for posterior herniation. *PLoS One* **12**, 1–23 (2017).

44. Boos, N. *et al.* Classification of age-related changes in lumbar intervertebral discs: 2002 Volvo award in basic science. *Spine (Phila. Pa. 1976).* **27**, 2631–2644 (2002).

45. Adler, J. H., Schoenbaum, M. & Silberberg, R. Early Onset of Disk Degeneration and Spondylosis in Sand Rats (Psammomys Obesus). *Vet. Pathol.* **20**, 13–22 (1983).

46. Yang, S. H. *et al.* Influence of age-related degeneration on regenerative potential of human nucleus pulposus cells. *J. Orthop. Res.* **28**, 379–383 (2010).

47. Patel, H. N. *et al.* Fibro-porous poliglecaprone/polycaprolactone conduits: synergistic effect of composition and *in vitro* degradation on mechanical properties. *Polym. Int.* **64**, 547–555 (2015).

48. Cs-Szabo, G. *et al.* Changes in mrna and protein levels of proteoglycans of the anulus fibrosus and nucleus pulposus during intervertebral disc degeneration. *Spine (Phila. Pa. 1976).* **27**, 2212–2219 (2002).

49. Kalb, S., Martirosyan, N. L., Kalani, M. Y. S., Broc, G. G. & Theodore, N. Genetics of the degenerated intervertebral disc. *World Neurosurg.* **77**, 491–501 (2012).

50. Brayda-Bruno, M. *et al.* Advances in the diagnosis of degenerated lumbar discs and their possible clinical application. *Eur. Spine J.* **23**, 315–323 (2014).

51. Colombier, P., Clouet, J., Hamel, O., Lescaudron, L. & Guicheux, J. The lumbar intervertebral disc: From embryonic development to degeneration. *Jt. Bone*

Spine **81**, 125–129 (2014).

52. Adams, M. A. Mechanical properties of aging soft tissues. 2015. *Intervertebral disc tissues* 7–35.
53. Mayer, J. E. *et al.* Genetic polymorphisms associated with intervertebral disc degeneration. *Spine J.* **13**, 299–317 (2013).
54. DeLuca, P. F., Mason, D. E., Weiand, R., Howard, R. & Bassett, G. S. Excision of Herniated Nucleus Pulposus in Children and Adolescents. *J. Pediatr. Orthop.* **14**, (1994).
55. Kurth, A. A., Rau, S., Wang, C. & Schmitt, E. Treatment of lumbar disc herniation in the second decade of life. *Eur. Spine J.* **5**, 220–224 (1996).
56. Arts, M. P. *et al.* Comparison of treatments for lumbar disc herniation. *Medicine (Baltimore).* **98**, e14410 (2019).
57. Shillito, J. Pediatric lumbar disc surgery: 20 patients under 15 years of age. *Surg. Neurol.* **46**, 14–17 (1996).
58. Kumar, R., Kumar, V., Das, N. K., Behari, S. & Mahapatra, A. K. Adolescent lumbar disc disease: Findings and outcome. *Child's Nerv. Syst.* **23**, 1295–1299 (2007).
59. Ozgen, S., Konya, D., Toktas, O. Z., Dagcinar, A. & Ozek, M. M. Lumbar disc herniation in adolescence. *Pediatr. Neurosurg.* **43**, 77–81 (2007).
60. Bulos, S. Herniated Intervertebral Lumbar Disc in the Teenager. *J. bone Jt. surgery. Br. Vol.* **55**, 273–8 (1973).
61. Song, K. J., Choi, B. W., Jeon, T. S., Lee, K. B. & Chang, H. Adjacent segment degenerative disease: Is it due to disease progression or a fusion-associated phenomenon? Comparison between segments adjacent to the fused and non-fused segments. *Eur. Spine J.* **20**, 1940–1945 (2011).
62. Wu, J.-C. *et al.* The Incidence of Adjacent Segment Disease Requiring Surgery After Anterior Cervical Diskectomy and Fusion: Estimation Using an 11-Year Comprehensive Nationwide Database in Taiwan. *Neurosurgery* **70**, 594–601 (2012).
63. Tang, S. & Rebholz, B. J. Does anterior lumbar interbody fusion promote adjacent degeneration in degenerative disc disease? A finite element study. *J. Orthop. Sci.* **16**, 221–228 (2011).
64. Zigler, J. *et al.* Results of the prospective, randomized, multicenter food and drug

administration investigational device exemption study of the ProDisc®-L total disc replacement versus circumferential fusion for the treatment of 1-level degenerative disc disease. *Spine (Phila. Pa. 1976).* **32**, 1155–1162 (2007).

65. Delamarter, R. *et al.* Prospective, randomized, multicenter food and drug administration investigational device exemption study of the ProDisc-L total disc replacement compared with circumferential arthrodesis for the treatment of two-level lumbar degenerative disc disease: Res. *J. Bone Jt. Surg. - Ser. A* **93**, 705–715 (2011).
66. Harrop, J. S. *et al.* Lumbar adjacent segment degeneration and disease after arthrodesis and total disc arthroplasty. *Spine (Phila. Pa. 1976).* **33**, 1701–1707 (2008).
67. Morishita, Y. *et al.* Kinematic evaluation of the adjacent segments after lumbar instrumented surgery: A comparison between rigid fusion and dynamic non-fusion stabilization. *Eur. Spine J.* **20**, 1480–1485 (2011).
68. Schaeren, S., Broger, I. & Jeanneret, B. Minimum four-year follow-up of spinal stenosis with degenerative spondylolisthesis treated with decompression and dynamic stabilization. *Spine (Phila. Pa. 1976).* **33**, 636–642 (2008).
69. Schnake, K. J., Schaeren, S. & Jeanneret, B. Dynamic Stabilization in Addition to Decompression for Lumbar Spinal Stenosis with Degenerative Spondylolisthesis. *Spine (Phila. Pa. 1976).* **31**, 442–449 (2006).
70. Henriksson, H. B. *et al.* Transplantation of human mesenchymal stems cells into intervertebral discs in a xenogeneic porcine model. *Spine (Phila. Pa. 1976).* **34**, 141–148 (2009).
71. Drazin, D. *et al.* Treatment of Recurrent Disc Herniation: A Systematic Review. *Cureus* **8**, (2016).
72. Ozgur, B. M., Aryan, H. E., Pimenta, L. & Taylor, W. R. Extreme Lateral Interbody Fusion (XLIF): a novel surgical technique for anterior lumbar interbody fusion. *Spine J.* **6**, 435–443 (2006).
73. Sakai, D. *et al.* Exhaustion of nucleus pulposus progenitor cells with ageing and degeneration of the intervertebral disc. *Nat. Commun.* **3**, (2012).
74. Sakai, D. *et al.* Migration of bone marrow-derived cells for endogenous repair in a new tail-looping disc degeneration model in the mouse: A pilot study. *Spine J.* **15**, 1356–1365 (2015).

75. Tzaan, W.-C. & Chen, H.-C. Investigating the Possibility of Intervertebral Disc Regeneration Induced by Granulocyte Colony Stimulating Factor-Stimulated Stem Cells in Rats. *Adv. Orthop.* **2011**, 1–5 (2011).

76. Guerin, H. A. L. & Elliott, D. M. Degeneration affects the fiber reorientation of human annulus fibrosus under tensile load. *J. Biomech.* **39**, 1410–1418 (2006).

77. Elliott, D. M. & Setton, L. A. Anisotropic and inhomogeneous tensile behavior of the human anulus fibrosus: Experimental measurement and material model predictions. *J. Biomech. Eng.* **123**, 256–263 (2001).

78. Wagner, D. R. & Lotz, J. C. Theoretical model and experimental results for the nonlinear elastic behavior of human annulus fibrosus. *J. Orthop. Res.* **22**, 901–909 (2004).

79. Wu, H. C. & Yao, R. F. Mechanical behavior of the human annulus fibrosus. *J. Biomech.* **9**, (1976).

80. Bailey, A., Araghi, A., Blumenthal, S. & Huffmon, G. V. Prospective, multicenter, randomized, controlled study of anular repair in lumbar discectomy. *Spine (Phila. Pa. 1976).* **38**, 1161–1169 (2013).

81. Ledic, D. *et al.* Effect of Anular Closure on Disk Height Maintenance and Reoperated Recurrent Herniation Following Lumbar Diskectomy: Two-Year Data. *J Neurol Surg A Cent Eur Neurosurg* **76**, 211–218 (2015).

82. Guterl, C. C. *et al.* Challenges and strategies in the repair of ruptured annulus fibrosus. *Eur. Cell. Mater.* **25**, 1–21 (2013).

83. Zündel, M., Mazza, E. & Ehret, A. E. A 2.5D approach to the mechanics of electrospun fibre mats. *Soft Matter* **13**, 6407–6421 (2017).

84. Nerurkar, N. L. *et al.* Nanofibrous biologic laminates replicate the form and function of the annulus fibrosus. *Nat. Mater.* (2009) doi:10.1038/nmat2558.

85. Martin, J. T. *et al.* Translation of an engineered nanofibrous disc-like angle-ply structure for intervertebral disc replacement in a small animal model. *Acta Biomater.* **10**, 2473–2481 (2014).

86. Li, W. J., Mauck, R. L., Cooper, J. A., Yuan, X. & Tuan, R. S. Engineering controllable anisotropy in electrospun biodegradable nanofibrous scaffolds for musculoskeletal tissue engineering. *J. Biomech.* **40**, 1686–1693 (2007).

87. Liu, C. *et al.* The effect of the fibre orientation of electrospun scaffolds on the matrix production of rabbit annulus fibrosus-derived stem cells. *Bone Res.* **3**,

(2015).

88. Koepsell, L. *et al.* Tissue engineering of annulus fibrosus using electrospun fibrous scaffolds with aligned polycaprolactone fibers. 564–575 (2011) doi:10.1002/jbm.a.33216.

89. Pirvu, T. *et al.* A combined biomaterial and cellular approach for annulus fibrosus rupture repair. *Biomaterials* **42**, 11–19 (2015).

90. Wismer, N. *et al.* Biodegradable electrospun scaffolds for annulus fibrosus tissue engineering: Effect of scaffold structure and composition on annulus fibrosus cells in vitro. *Tissue Eng. - Part A* **20**, 672–682 (2014).

91. Vadalà, G. *et al.* Bioactive electrospun scaffold for annulus fibrosus repair and regeneration. *Eur. Spine J.* **21**, 20–26 (2012).

92. Behonick, D. J. & Werb, Z. A bit of give and take: The relationship between the extracellular matrix and the developing chondrocyte. *Mech. Dev.* **120**, 1327–1336 (2003).

93. Franceschi, R. T. & Iyer, B. S. Relationship between collagen synthesis and expression of the osteoblast phenotype in MC3T3-E1 cells. *J. Bone Miner. Res.* **7**, 235–246 (1992).

94. Lan, C. W., Wang, F. F. & Wang, Y. J. Osteogenic enrichment of bone-marrow stromal cells with the use of flow chamber and type I collagen-coated surface. *J. Biomed. Mater. Res. - Part A* **66**, 38–46 (2003).

95. Li, W. J., Laurencin, C. T., Caterson, E. J., Tuan, R. S. & Ko, F. K. Electrospun nanofibrous structure: A novel scaffold for tissue engineering. *J. Biomed. Mater. Res.* **60**, 613–621 (2002).

96. Mo, X. M., Xu, C. Y., Kotaki, M. & Ramakrishna, S. Electrospun P(LLA-CL) nanofiber: A biomimetic extracellular matrix for smooth muscle cell and endothelial cell proliferation. *Biomaterials* **25**, 1883–1890 (2004).

97. Liu, X. & Ma, P. X. Polymeric Scaffolds for Bone Tissue Engineering. *Ann. Biomed. Eng.* **32**, 477–486 (2004).

98. Subbiah, T., Bhat, G. S., Tock, R. W., Parameswaran, S. & Ramkumar, S. S. Electrospinning of nanofibers. *J. Appl. Polym. Sci.* **96**, 557–569 (2005).

99. Huang, Z. M., Zhang, Y. Z., Kotaki, M. & Ramakrishna, S. A review on polymer nanofibers by electrospinning and their applications in nanocomposites. *Compos. Sci. Technol.* **63**, 2223–2253 (2003).

100. Fridrikh, S. V., Yu, J. H., Brenner, M. P. & Rutledge, G. C. Controlling the Fiber Diameter during Electrospinning. *Phys. Rev. Lett.* **90**, 144502 (2003).

101. Bergshoef, M. M. & Vancso, G. J. Transparent nanocomposites with ultrathin, electrospun nylon-4,6 fiber reinforcement. *Adv. Mater.* **11**, 1362–1365 (1999).

102. Li, W. J., Danielson, K. G., Alexander, P. G. & Tuan, R. S. Biological response of chondrocytes cultured in three-dimensional nanofibrous poly(ε-caprolactone) scaffolds. *J. Biomed. Mater. Res. - Part A* **67**, 1105–1114 (2003).

103. Li, D. & Xia, Y. Electrospinning of nanofibers: Reinventing the wheel? *Adv. Mater.* **16**, 1151–1170 (2004).

104. Sharma, B. & Elisseeff, J. H. Engineering structurally organized cartilage and bone tissues. *Ann. Biomed. Eng.* **32**, 148–159 (2004).

105. Hutmacher, D. W. Scaffolds in tissue engineering bone and cartilage. *Biomater. Silver Jubil. Compend.* **21**, 175–189 (2000).

106. Tuan, R. S., Boland, G. & Tuli, R. Adult mesenchymal stem cells and cell-based tissue engineering. *Arthritis Res. Ther.* **5**, 32–45 (2003).

107. Li, W. J., Tuli, R., Huang, X., Laquerriere, P. & Tuan, R. S. Multilineage differentiation of human mesenchymal stem cells in a three-dimensional nanofibrous scaffold. *Biomaterials* **26**, 5158–5166 (2005).

108. Li, W. J. *et al.* A three-dimensional nanofibrous scaffold for cartilage tissue engineering using human mesenchymal stem cells. *Biomaterials* **26**, 599–609 (2005).

109. Yoshimoto, H., Shin, Y. M., Terai, H. & Vacanti, J. P. A biodegradable nanofiber scaffold by electrospinning and its potential for bone tissue engineering. *Biomaterials* **24**, 2077–2082 (2003).

110. Shin, M., Yoshimoto, H. & Vacanti, J. P. In Vivo Bone Tissue Engineering Using Mesenchymal Stem Cells on a Novel Electrospun Nanofibrous Scaffold. *Tissue Eng.* **10**, 33–41 (2004).

111. Dalton, P. D., Klee, D. & Möller, M. Electrospinning with dual collection rings. *Polymer (Guildf).* **46**, 611–614 (2005).

112. Kim, B., Park, H., Lee, S. H. & Sigmund, W. M. Poly(acrylic acid) nanofibers by electrospinning. *Mater. Lett.* **59**, 829–832 (2005).

113. Lim, S. K., Lee, S. K., Hwang, S. H. & Kim, H. Photocatalytic deposition of silver nanoparticles onto organic/inorganic composite nanofibers. *Macromol. Mater.*

Eng. **291**, 1265–1270 (2006).

114. Peng, Y. *et al.* Preparation of polysulfone membranes via vapor-induced phase separation and simulation of direct-contact membrane distillation by measuring hydrophobic layer thickness. *Desalination* **316**, 53–66 (2013).
115. Yongquan, D., Ming, W., Lin, C. & Mingjun, L. Preparation, characterization of P(VDF-HFP)/[bmim]BF 4 ionic liquids hybrid membranes and their pervaporation performance for ethyl acetate recovery from water. *Desalination* **295**, 53–60 (2012).
116. Reneker, D. & Fong, H. Polymeric Nanofibers: Introduction. in *ACS Symposium Series* 1–6 (2006). doi:10.1021/bk-2006-0918.ch001.
117. Chen, L., Bromberg, L., Hatton, T. A. & Rutledge, G. C. Catalytic hydrolysis of p-nitrophenyl acetate by electrospun polyacrylamidoxime nanofibers. *Polymer (Guildf).* **48**, 4675–4682 (2007).
118. Katepalli, H., Bikshapathi, M., Sharma, C. S., Verma, N. & Sharma, A. Synthesis of hierarchical fabrics by electrospinning of PAN nanofibers on activated carbon microfibers for environmental remediation applications. *Chem. Eng. J.* **171**, 1194–1200 (2011).
119. Kijeńska, E., Prabhakaran, M. P., Swieszkowski, W., Kurzydlowski, K. J. & Ramakrishna, S. Electrospun bio-composite P(LLA-CL)/collagen I/collagen III scaffolds for nerve tissue engineering. *J. Biomed. Mater. Res. - Part B Appl. Biomater.* **100 B**, 1093–1102 (2012).
120. Auffan, M. *et al.* Electrospinning. in *Encyclopedia of Nanotechnology* 769–775 (Springer Netherlands, 2012). doi:10.1007/978-90-481-9751-4_357.
121. Shin, Y. M., Hohman, M. M., Brenner, M. P. & Rutledge, G. C. Electrospinning: A whipping fluid jet generates submicron polymer fibers. *Appl. Phys. Lett.* **78**, 1149–1151 (2001).
122. Shin, Y. M., Hohman, M. M., Brenner, M. P. & Rutledge, G. C. Experimental characterization of electrospinning: The electrically forced jet and instabilities. *Polymer (Guildf).* **42**, 09955–09967 (2001).
123. Geng, X., Kwon, O. H. & Jang, J. Electrospinning of chitosan dissolved in concentrated acetic acid solution. *Biomaterials* **26**, 5427–5432 (2005).
124. Megelski, S., Stephens, J. S., Bruce Chase, D. & Rabolt, J. F. Micro- and nanostructured surface morphology on electrospun polymer fibers.

Macromolecules **35**, 8456–8466 (2002).

125. Zeleny, J. The Role of Surface Instability in Electrical. **219**, 1314–1345 (1935).
126. Sill, T. J. & von Recum, H. A. Electrospinning: Applications in drug delivery and tissue engineering. *Biomaterials* **29**, 1989–2006 (2008).
127. Studer, H., Larrea, X., Riedwyl, H. & Büchler, P. Biomechanical model of human cornea based on stromal microstructure. *J. Biomech.* **43**, 836–842 (2010).
128. Yuan, X. Y., Zhang, Y. Y., Dong, C. & Sheng, J. Morphology of ultrafine polysulfone fibers prepared by electrospinning. *Polym. Int.* **53**, 1704–1710 (2004).
129. Baumgarten, P. K. Electrostatic spinning of acrylic microfibers. *J. Colloid Interface Sci.* **36**, 71–79 (1971).
130. Zong, X. *et al.* Structure and process relationship of electrospun bioabsorbable nanofiber membranes. *Polymer (Guildf).* **43**, 4403–4412 (2002).
131. Zhang, C., Yuan, X., Wu, L., Han, Y. & Sheng, J. Study on morphology of electrospun poly(vinyl alcohol) mats. *Eur. Polym. J.* **41**, 423–432 (2005).
132. Jarusuwannapoom, T. *et al.* Effect of solvents on electro-spinnability of polystyrene solutions and morphological appearance of resulting electrospun polystyrene fibers. *Eur. Polym. J.* **41**, 409–421 (2005).
133. Kim, H. S., Kim, K., Jin, H. J. & Chin, I. J. Morphological characterization of electrospun nano-fibrous membranes of biodegradable poly(l-lactide) and poly(lactide-co-glycolide). *Macromol. Symp.* **224**, 145–154 (2005).
134. Deitzel, J. M., Kleinmeyer, J., Harris, D. & Beck Tan, N. C. The effect of processing variables on the morphology of electrospun. *Polymer (Guildf).* **42**, 261–272 (2001).
135. Son, W. K., Youk, J. H., Lee, T. S. & Park, W. H. The effects of solution properties and polyelectrolyte on electrospinning of ultrafine poly(ethylene oxide) fibers. *Polymer (Guildf).* **45**, 2959–2966 (2004).
136. Koski, A., Yim, K. & Shivkumar, S. Effect of molecular weight on fibrous PVA produced by electrospinning. *Mater. Lett.* **58**, 493–497 (2004).
137. Lee, J. S. *et al.* Role of molecular weight of atactic poly(vinyl alcohol) (PVA) in the structure and properties of PVA nanofabric prepared by electrospinning. *J. Appl. Polym. Sci.* **93**, 1638–1646 (2004).
138. Ding, B. *et al.* Preparation and characterization of a nanoscale poly(vinyl alcohol)

fiber aggregate produced by an electrospinning method. *J. Polym. Sci. Part B Polym. Phys.* **40**, 1261–1268 (2002).

139. Gupta, P., Elkins, C., Long, T. E. & Wilkes, G. L. Electrospinning of linear homopolymers of poly(methyl methacrylate): Exploring relationships between fiber formation, viscosity, molecular weight and concentration in a good solvent. *Polymer (Guildf).* **46**, 4799–4810 (2005).

140. Demir, M. M., Yilgor, I., Yilgor, E. & Erman, B. Electrospinning of polyurethane fibers. *Polymer (Guildf).* **43**, 3303–3309 (2002).

141. Ki, C. S. *et al.* Characterization of gelatin nanofiber prepared from gelatin-formic acid solution. *Polymer (Guildf).* **46**, 5094–5102 (2005).

142. McKee, M. G., Wilkes, G. L., Colby, R. H. & Long, T. E. Correlations of Solution Rheology with Electrospun Fiber Formation of Linear and Branched Polyesters. *Macromolecules* **37**, 1760–1767 (2004).

143. Huang, L., Nagapudi, K., Apkarian, P. R. & Chaikof, E. L. Engineered collagen - PEO nanofibers and fabrics. *J. Biomater. Sci. Polym. Ed.* **12**, 979–993 (2001).

144. Sun, B. *et al.* Advances in three-dimensional nanofibrous macrostructures via electrospinning. *Prog. Polym. Sci.* **39**, 862–890 (2014).

145. Mit-Uppatham, C., Nithitanakul, M. & Supaphol, P. Ultrafine electrospun polyamide-6 fibers: Effect of solution conditions on morphology and average fiber diameter. *Macromol. Chem. Phys.* **205**, 2327–2338 (2004).

146. Casper, C. L., Stephens, J. S., Tassi, N. G., Chase, D. B. & Rabolt, J. F. Controlling surface morphology of electrospun polystyrene fibers: Effect of humidity and molecular weight in the electrospinning process. *Macromolecules* **37**, 573–578 (2004).

147. Sell, S. A. *et al.* The use of natural polymers in tissue engineering: A focus on electrospun extracellular matrix analogues. *Polymers (Basel).* **2**, 522–553 (2010).

148. Cai, S., Xu, H., Jiang, Q. & Yang, Y. Novel 3D electrospun scaffolds with fibers oriented randomly and evenly in three dimensions to closely mimic the unique architectures of extracellular matrices in soft tissues: Fabrication and mechanism study. *Langmuir* **29**, 2311–2318 (2013).

149. Chen, Z. G., Wang, P. W., Wei, B., Mo, X. M. & Cui, F. Z. Electrospun collagen-chitosan nanofiber: A biomimetic extracellular matrix for endothelial cell and

smooth muscle cell. *Acta Biomater.* **6**, 372–382 (2010).

150. Van Lieshout, M. I., Vaz, C. M., Rutten, M. C. M., Peters, G. W. M. & Baaijens, F. P. T. Electrospinning versus knitting: Two scaffolds for tissue engineering of the aortic valve. *J. Biomater. Sci. Polym. Ed.* **17**, 77–89 (2006).
151. Balguid, A. *et al.* Tailoring Fiber Diameter in Electrospun Poly(ε-Caprolactone) Scaffolds for Optimal Cellular Infiltration in Cardiovascular Tissue Engineering. *Tissue Eng. Part A* **15**, 437–444 (2009).
152. Vaz, C. M., van Tuijl, S., Bouten, C. V. C. & Baaijens, F. P. T. Design of scaffolds for blood vessel tissue engineering using a multi-layering electrospinning technique. *Acta Biomater.* **1**, 575–582 (2005).
153. Reed, C. R. *et al.* Composite tissue engineering on polycaprolactone nanofiber scaffolds. *Ann. Plast. Surg.* **62**, 505–512 (2009).
154. Chen, M., Michaud, H. & Bhowmick, S. Controlled Vacuum Seeding as a Means of Generating Uniform Cellular Distribution in Electrospun Polycaprolactone (PCL) Scaffolds. *J. Biomech. Eng.* **131**, 074521 (2009).
155. Possin, K. L., Filoteo, J. V., Song, D. D. & Salmon, D. P. NIH Public Access. **22**, 585–595 (2010).
156. Li, X. *et al.* Nanofiber scaffolds with gradations in mineral content for mimicking the tendon-to-bone insertion site. *Nano Lett.* **9**, 2763–2768 (2009).
157. Lowery, J. L., Datta, N. & Rutledge, G. C. Effect of fiber diameter, pore size and seeding method on growth of human dermal fibroblasts in electrospun poly(ε-caprolactone) fibrous mats. *Biomaterials* **31**, 491–504 (2010).
158. Wang, S., Zhong, S., Lim, C. T. & Nie, H. Effects of fiber alignment on stem cells–fibrous scaffold interactions. *J. Mater. Chem. B* **3**, 3358–3366 (2015).
159. Saino, E. *et al.* Effect of electrospun fiber diameter and alignment on macrophage activation and secretion of proinflammatory cytokines and chemokines. *Biomacromolecules* **12**, 1900–1911 (2011).
160. Bose, S., Roy, M. & Bandyopadhyay, A. Recent advances in bone tissue engineering scaffolds. *Trends Biotechnol.* **30**, 546–554 (2012).
161. Zhong, S. P., Zhang, Y. Z. & Lim, C. T. Tissue scaffolds for skin wound healing and dermal reconstruction. *Wiley Interdiscip. Rev. Nanomedicine Nanobiotechnology* **2**, 510–525 (2010).
162. Mijovic, B. & Agic, A. Bio-inspired Electrospun Fibre Structures - Numerical

Model. *J. Fiber Bioeng. Informatics* **6**, 23–32 (2013).

163. Argento, G., Simonet, M., Oomens, C. W. J. & Baaijens, F. P. T. Multi-scale mechanical characterization of scaffolds for heart valve tissue engineering. *J. Biomech.* **45**, 2893–2898 (2012).

164. Arinstein, A., Burman, M., Gendelman, O. & Zussman, E. Effect of supramolecular structure on polymer nanofibre elasticity. *Nat. Nanotechnol.* **2**, 59–62 (2007).

165. Pham, Q. P., Sharma, U. & Mikos, A. G. Electrospun poly (ε-caprolactone) microfiber and multilayer nanofiber/microfiber scaffolds: Characterization of scaffolds and measurement of cellular infiltration. *Biomacromolecules* **7**, 2796–2805 (2006).

166. Walser, J., Stok, K. S., Caversaccio, M. D. & Ferguson, S. J. Direct electrospinning of 3D auricle-shaped scaffolds for tissue engineering applications. *Biofabrication* **8**, (2016).

167. Croisier, F. *et al.* Mechanical testing of electrospun PCL fibers. *Acta Biomater.* **8**, 218–224 (2012).

168. Lim, C. T., Tan, E. P. S. & Ng, S. Y. Effects of crystalline morphology on the tensile properties of electrospun polymer nanofibers Effects of crystalline morphology on the tensile properties of electrospun polymer nanofibers. *Appl. Phys. Lett.* **141908**, (2008).

169. Wong, S.-C., Baji, A. & Leng, S. Effect of fiber diameter on tensile properties of electrospun poly(ε-caprolactone). *Polymer (Guildf).* **49**, 4713–4722 (2008).

170. Tan, E. P. S., Ng, S. Y. & Lim, C. T. Tensile testing of a single ultrafine polymeric fiber. *Biomaterials* **26**, 1453–1456 (2005).

171. Baker, S. R., Banerjee, S., Bonin, K. & Guthold, M. Determining the mechanical properties of electrospun poly-ε-caprolactone (PCL) nanofibers using AFM and a novel fiber anchoring technique. *Mater. Sci. Eng. C* **59**, 203–212 (2016).

172. Tan, E. P. S. & Lim, C. T. Physical properties of a single polymeric nanofiber. *Appl. Phys. Lett.* **84**, 1603–1605 (2004).

173. Menczel, J. D. *Thermal analysis of polymers*. (Wiley, 2009).

174. Crescenzi, V., Manzini, G., Calzolari, G. & Borri, C. Thermodynamics of fusion of poly-β-propiolactone and poly-ε{lunate}-caprolactone. comparative analysis of the melting of aliphatic polylactone and polyester chains. *Eur. Polym. J.* **8**, 449–

463 (1972).

175. Gallagher, A. J.; Ní Annaidh, Aisling; Bruyère, K. et al. Title Dynamic Tensile Properties of Human Skin. in *IRCOBI Conference Proceedings* (2012).

176. Yang, W. *et al.* On the tear resistance of skin. *Nat. Commun.* **6**, 6649 (2015).

177. Ferraiuoli, P. *et al.* Full - field analysis of epicardial strain in an in vitro porcine heart platform. *J. Mech. Behav. Biomed. Mater.* **91**, 294–300 (2018).

178. Fukunaga, T. *et al.* In vivo behaviour of human muscle tendon during walking. *Proc. R. Soc. B Biol. Sci.* **268**, 229–233 (2001).

179. Imura, T., Yamamoto, K., Kanamori, K., Mikami, T. & Yasuda, H. Non-invasive ultrasonic measurement of the elastic properties of the human abdominal aorta. *Cardiovasc. Res.* **20**, 208–14 (1986).

180. Greenfield, J. C. & Griggs, D. M. Relation between pressure and diameter in main pulmonary artery of man. *J. Appl. Physiol.* **18**, 557–559 (1963).

181. Heuer, F., Wolfram, U., Schmidt, H. & Wilke, H. J. A method to obtain surface strains of soft tissues using a laser scanning device. *J. Biomech.* **41**, 2402–2410 (2008).

182. Averous, L., Moro, L., Dole, P. & Fringant, C. Properties of thermoplastic blends: Starch-polycaprolactone. *Polymer (Guildf).* **41**, 4157–4167 (2000).

183. Chen, B. & Sun, K. Mechanical and dynamic viscoelastic properties of hydroxyapatite reinforced poly(ε-caprolactone). *Polym. Test.* **24**, 978–982 (2005).

184. Morel, A. *et al.* Revealing non-crystalline polymer superstructures within electrospun fibers through solvent-induced phase rearrangements. *Nanoscale* **11**, 16788–16800 (2019).

185. Huang, Z. M., Zhang, Y. Z., Ramakrishna, S. & Lim, C. T. Electrospinning and mechanical characterization of gelatin nanofibers. *Polymer (Guildf).* **45**, 5361–5368 (2004).

186. Gu, S. Y., Wu, Q. L., Ren, J. & Vancso, G. J. Mechanical properties of a single electrospun fiber and its structures. *Macromol. Rapid Commun.* **26**, 716–720 (2005).

187. Cuenot, S., Demoustier-Champagne, S. & Nysten, B. Elastic modulus of polypyrrole nanotubes. *Phys. Rev. Lett.* **85**, 1690–1693 (2000).

188. Ji, Y., Li, B., Ge, S., Sokolov, J. C. & Rafailovich, M. H. Structure and

nanomechanical characterization of electrospun PS/clay nanocomposite fibers. *Langmuir* **22**, 1321–1328 (2006).

189. Lee, S. J. *et al.* The use of thermal treatments to enhance the mechanical properties of electrospun poly(ε-caprolactone) scaffolds. *Biomaterials* **29**, 1422–1430 (2008).

190. Pai, C. L., Boyce, M. C. & Rutledge, G. C. On the importance of fiber curvature to the elastic moduli of electrospun nonwoven fiber meshes. *Polymer (Guildf).* **52**, 6126–6133 (2011).

191. Morel, A. *et al.* Correlating diameter, mechanical and structural properties of poly(L-lactide) fibres from needleless electrospinning. *Acta Biomater.* **81**, 169–183 (2018).

192. D'Amore, A. *et al.* From single fiber to macro-level mechanics: A structural finite-element model for elastomeric fibrous biomaterials. *J. Mech. Behav. Biomed. Mater.* **39**, 146–161 (2014).

193. Mauri, A., Perrini, M., Ehret, A. E., De Focatiis, D. S. a. & Mazza, E. Time-dependent mechanical behavior of human amnion: Macroscopic and microscopic characterization. *Acta Biomater.* **11**, 314–323 (2015).

194. Wei, X., Xia, Z., Wong, S. C. & Baji, A. Modelling of mechanical properties of electrospun nanofibre network. *Int. J. Exp. Comput. Biomech.* **1**, 45 (2009).

195. Gullbrand, S. E. *et al.* Long-term mechanical function and integration of an implanted tissue-engineered intervertebral disc. *Sci. Transl. Med.* **10**, eaau0670 (2018).

196. Ali, S. A. M., Zhong, S. P., Doherty, P. J. & Williams, D. F. Mechanisms of polymer degradation in implantable devices. I. Poly(caprolactone). *Biomaterials* **14**, 648–656 (1993).

197. Lam, C. X. F., Hutmacher, D. W., Schantz, J.-T., Woodruff, M. A. & Teoh, S. H. Evaluation of polycaprolactone scaffold degradation for 6 months in vitro and in vivo. *J. Biomed. Mater. Res. Part A* **90A**, 906–919 (2009).

198. Sun, H., Mei, L., Song, C., Cui, X. & Wang, P. The in vivo degradation, absorption and excretion of PCL-based implant. *Biomaterials* **27**, 1735–1740 (2006).

199. Pitt, C. G. *et al.* Aliphatic Polyesters . I . The Degradation of Poly (e-caprolactone) In Vivo. *J. Appl. Polym. Sci.* **26**, 3779–3787 (1981).

200. Duling, R. R., Dupaix, R. B., Katsube, N. & Lannutti, J. Mechanical

characterization of electrospun polycaprolactone (PCL): A potential scaffold for tissue engineering. *J. Biomech. Eng.* **130**, 1–13 (2008).

201. Tiğli, R. S., Kazaroğlu, N. M., Maviş, B. & Gumusderelioglu, M. Cellular behavior on epidermal growth factor (EGF)-immobilized PCL/gelatin nanofibrous scaffolds. *J. Biomater. Sci. Polym. Ed.* **22**, 207–223 (2011).

202. Chung, A. S. *et al.* Lamellar stack formation and degradative behaviors of hydrolytically degraded poly(ε-caprolactone) and poly(glycolide-ε-caprolactone) blended fibers. *J. Biomed. Mater. Res. - Part B Appl. Biomater.* **100 B**, 274–284 (2012).

203. Baker, B. M., Nerurkar, N. L., Burdick, J. A., Elliott, D. M. & Mauck, R. L. Fabrication and modeling of dynamic multipolymer nanofibrous scaffolds. *J. Biomech. Eng.* **131**, 1–10 (2009).

204. Sant, S., Iyer, D., Gaharwar, A. K., Patel, A. & Khademhosseini, A. Effect of biodegradation and de novo matrix synthesis on the mechanical properties of valvular interstitial cell-seeded polyglycerol sebacate–polycaprolactone scaffolds. *Acta Biomater.* **9**, 5963–5973 (2013).

205. Bölgen, N., Menceloğlu, Y. Z., Acatay, K., Vargel, I. & Pişkin, E. In vitro and in vivo degradation of non-woven materials made of poly(ε-caprolactone) nanofibers prepared by electrospinning under different conditions. *J. Biomater. Sci. Polym. Ed.* **16**, 1537–1555 (2005).

206. Pektok, E. *et al.* Degradation and healing characteristics of small-diameter poly(ε-caprolactone) vascular grafts in the rat systemic arterial circulation. *Circulation* **118**, 2563–2570 (2008).

207. Sung, H. J., Meredith, C., Johnson, C. & Galis, Z. S. The effect of scaffold degradation rate on three-dimensional cell growth and angiogenesis. *Biomaterials* **25**, 5735–5742 (2004).

208. Johnson, J. *et al.* Electrospun PCL in vitro: A Microstructural basis for mechanical property changes. *J. Biomater. Sci. Polym. Ed.* **20**, 467–481 (2009).

209. de Valence, S. *et al.* Long term performance of polycaprolactone vascular grafts in a rat abdominal aorta replacement model. *Biomaterials* **33**, 38–47 (2012).

210. Helgason, B., Lindenmann, P., Studer, H., Reutlinger, C. & Ferguson, S. J. A Parameterized FE Model for Simulating the Influence of Disc Anatomy on the Mechanical Response of Human Intervertebral Discs. *Proc. 10th Int. Symp.*

Comput. Methods Biomech. Biomed. Eng. 999–1003 (2012).

211. Panjabi, M. M. *et al.* Human lumbar vertebrae. Quantitative three-dimensional anatomy. *Spine (Phila. Pa. 1976).* **17**, 299–306 (1992).

212. Abuzayed, B., Tutunculer, B., Kucukyuruk, B. & Tuzgen, S. Anatomic basis of anterior and posterior instrumentation of the spine: Morphometric study. *Surg. Radiol. Anat.* **32**, 75–85 (2010).

213. Rohlmann, A., Zander, T., Schmidt, H., Wilke, H. J. & Bergmann, G. Analysis of the influence of disc degeneration on the mechanical behaviour of a lumbar motion segment using the finite element method. *J. Biomech.* **39**, 2484–2490 (2006).

214. Meijer, G. J. M., Homminga, J., Hekman, E. E. G., Veldhuizen, A. G. & Verkerke, G. J. The effect of three-dimensional geometrical changes during adolescent growth on the biomechanics of a spinal motion segment. *J. Biomech.* **43**, 1590–1597 (2010).

215. Markert, B., Ehlers, W. & Karajan, N. A general polyconvex strain-energy function for fiber-reinforced materials. *Pamm* **5**, 245–246 (2005).

216. Cohen, J. *Statistical power analysis for the behavioral sciences*. (Hillsdale, N.J. : L. Erlbaum Associates, 1988).

217. Cipitria, a., Skelton, a., Dargaville, T. R., Dalton, P. D. & Hutmacher, D. W. Design, fabrication and characterization of PCL electrospun scaffolds—a review. *J. Mater. Chem.* **21**, 9419 (2011).

218. Gautam, S., Dinda, A. K. & Mishra, N. C. Fabrication and characterization of PCL/gelatin composite nanofibrous scaffold for tissue engineering applications by electrospinning method. *Mater. Sci. Eng. C* **33**, 1228–1235 (2013).

219. Li, W. J., Cooper, J. A., Mauck, R. L. & Tuan, R. S. Fabrication and characterization of six electrospun poly(α-hydroxy ester)-based fibrous scaffolds for tissue engineering applications. *Acta Biomater.* **2**, 377–385 (2006).

220. Baker, B. M., Nerurkar, N. L., Burdick, J. A., Elliott, D. M. & Mauck, R. L. Fabrication and modeling of dynamic multipolymer nanofibrous scaffolds. *J. Biomech. Eng.* **131**, 1–22 (2009).

221. Nelson, M. T., Johnson, J. & Lannutti, J. Media-based effects on the hydrolytic degradation and crystallization of electrospun synthetic-biologic blends. *J. Mater. Sci. Mater. Med.* **25**, 297–309 (2014).

222. Kim, G. H. Electrospun PCL nanofibers with anisotropic mechanical properties as a biomedical scaffold. *Biomed. Mater.* **3**, 025010 (2008).

223. Guo, F. *et al.* An electrospun strong PCL/PU composite vascular graft with mechanical anisotropy and cyclic stability. *J. Mater. Chem. A* **3**, 4782–4787 (2015).

224. Zhang, J. *et al.* Annealing regulates the performance of an electrospun poly(ε-caprolactone) membrane to accommodate tissue engineering. *RSC Adv.* **5**, 32604–32608 (2015).

225. Kim, H. H., Kim, M. J., Ryu, S. J., Ki, C. S. & Park, Y. H. Effect of fiber diameter on surface morphology, mechanical property, and cell behavior of electrospun poly(ε-caprolactone) mat. *Fibers Polym.* **17**, 1033–1042 (2016).

226. Vogt, L. *et al.* Poly(ε-caprolactone)/poly(glycerol sebacate) electrospun scaffolds for cardiac tissue engineering using benign solvents. *Mater. Sci. Eng. C* **103**, 109712 (2019).

227. Stromberg, D. D. & Wiederhielm, C. A. Viscoelastic description of a collagenous tissue in simple elongation. *J. Appl. Physiol.* **26**, 857–862 (1969).

228. Ribeiro, C., Sencadas, V., Costa, C. M., Gómez Ribelles, J. L. & Lanceros-Méndez, S. Tailoring the morphology and crystallinity of poly(L-lactide acid) electrospun membranes. *Sci. Technol. Adv. Mater.* **12**, (2011).

229. Dusunceli, N. & Colak, O. U. Modelling effects of degree of crystallinity on mechanical behavior of semicrystalline polymers. *Int. J. Plast.* **24**, 1224–1242 (2008).

230. Perego, G., Cella, G. D. & Bastioli, C. Effect of molecular weight and crystallinity on poly(lactic acid) mechanical properties. *J. Appl. Polym. Sci.* **59**, 37–43 (1996).

231. Sen, S., Jacobs, N. T., Boxberger, J. I. & Elliott, D. M. Human annulus fibrosus dynamic tensile modulus increases with degeneration. *Mech. Mater.* **44**, 93–98 (2012).

232. Isaacs, J. L., Vresilovic, E., Sarkar, S. & Marcolongo, M. Role of biomolecules on annulus fibrosus micromechanics: Effect of enzymatic digestion on elastic and failure properties. *J. Mech. Behav. Biomed. Mater.* **40**, 75–84 (2014).

233. O'Connell, G. D., Johannessen, W., Vresilovic, E. J. & Elliott, D. M. Human internal disc strains in axial compression measured noninvasively using magnetic resonance imaging. *Spine (Phila. Pa. 1976).* **32**, 2860–2868 (2007).

234. Ebara, S. *et al.* Tensile properties of nondegenerate human lumbar anulus fibrosus. *Spine (Phila. Pa. 1976).* **21**, 452–461 (1996).

235. Bass, E. C., Ashford, F. A., Segal, M. R. & Lotz, J. C. Biaxial testing of human annulus fibrosus and its implications for a constitutive formulation. *Ann. Biomed. Eng.* **32**, 1231–1242 (2004).

236. Acaroglu, E. R. *et al.* Degeneration and Aging Affect the Tensile Behavior of Human Lumbar Anulus Fibrosus. *Spine (Phila. Pa. 1976).* **20**, (1995).

237. Skrzypiec, D. M., Pollintine, P., Przybyla, A., Dolan, P. & Adams, M. A. The internal mechanical properties of cervical intervertebral discs as revealed by stress profilometry. *Eur. Spine J.* **16**, 1701–1709 (2007).

238. Shan, Z. *et al.* Correlation between biomechanical properties of the annulus fibrosus and magnetic resonance imaging (MRI) findings. *Eur. Spine J.* **24**, 1909–1916 (2015).

239. Long, R. G. *et al.* Mechanical restoration and failure analyses of a hydrogel and scaffold composite strategy for annulus fibrosus repair. *Acta Biomater.* **30**, 116–125 (2016).

240. Cruz, M. A. *et al.* Structural and Chemical Modification to Improve Adhesive and Material Properties of Fibrin-Genipin for Repair of Annulus Fibrosus Defects in Intervertebral Disks. *J. Biomech. Eng.* **139**, 084501 (2017).

241. Skrzypiec, D., Tarala, M., Pollintine, P., Dolan, P. & Adams, M. A. When are intervertebral discs stronger than their adjacent vertebrae? *Spine (Phila. Pa. 1976).* **32**, 2455–2461 (2007).

242. Showalter, B. L. *et al.* Comparison of animal discs used in disc research to human lumbar disc: Torsion mechanics and collagen content. *Spine (Phila. Pa. 1976).* **37**, 166–173 (2012).

243. Demers, C. N., Antoniou, J. & Mwale, F. Value and limitations of using the bovine tail as a model for the human lumbar spine. *Spine (Phila. Pa. 1976).* **29**, 2793–2799 (2004).

244. Jaumard, N. V., Richards, R. C., Stagg-Williams, S. M. & Friis, E. A. Synthetic lumbar intervertebral disk for medical education. *J. Med. Devices, Trans. ASME* **1**, 212–216 (2007).

245. Beer, J. C. & Beer, J. M. Synthetic intervertebral disc. (1995).

246. GL, M. Synthetic intervertebral disc prosthesis. 1–6 (1989).

247. Gyles, D. A., Castro, L. D., Silva, J. O. C. & Ribeiro-Costa, R. M. A review of the designs and prominent biomedical advances of natural and synthetic hydrogel formulations. *Eur. Polym. J.* **88**, 373–392 (2017).

248. Frauchiger, D. A. *et al.* A review of the application of reinforced hydrogels and silk as biomaterials for intervertebral disc repair. *Eur. Cells Mater.* **34**, 271–290 (2017).

249. Stergar, J., Gradisnik, L., Velnar, T. & Maver, U. Intervertebral disc tissue engineering: A brief review. *Bosn. J. Basic Med. Sci.* **19**, 130–137 (2019).

250. Mizuno, H. *et al.* Biomechanical and biochemical characterization of composite tissue-engineered intervertebral discs. *Biomaterials* **27**, 362–370 (2006).

251. Bowles, R. D. *et al.* Image-based tissue engineering of a total intervertebral disc implant for restoration of function to the rat lumbar spine. *NMR Biomed.* **25**, 443–451 (2012).

252. Zhuang, Y. *et al.* Construction of tissue-engineered composite intervertebral disc and preliminary morphological and biochemical evaluation. *Biochem. Biophys. Res. Commun.* **407**, 327–332 (2011).

253. Sato, K., Kikuchi, S. & Yonezawa, T. In vivo intradiscal pressure measurement in healthy individuals and in patients with ongoing back problems. *Spine (Phila. Pa. 1976).* **24**, 2468–2474 (1999).

254. Sakai, D. *et al.* Atelocollagen for culture of human nucleus pulposus cells forming nucleus pulposus-like tissue in vitro: Influence on the proliferation and proteoglycan production of HNPSV-1 cells. *Biomaterials* **27**, 346–353 (2006).

255. Bron, J. L., Koenderink, G. H., Everts, V. & Smit, T. H. Rheological characterization of the nucleus pulposus and dense collagen scaffolds intended for functional replacement. *J. Orthop. Res.* **27**, 620–626 (2009).

256. Mwale, F. *et al.* Biological evaluation of chitosan salts cross-linked to genipin as a cell scaffold for disk tissue engineering. *Tissue Eng.* **11**, 130–140 (2005).

257. Revell, P. A. *et al.* Tissue engineered intervertebral disc repair in the pig using injectable polymers. *J. Mater. Sci. Mater. Med.* **18**, 303–308 (2007).

258. Rong, Y., Sugumaran, G., Silbert, J. E. & Spector, M. Proteoglycans synthesized by canine intervertebral disc cells grown in a type I collagen-glycosaminoglycan matrix. *Tissue Eng.* **8**, 1037–1047 (2002).

259. Natarajan, R. N., Williams, J. R. & Andersson, G. B. J. Modeling changes in

intervertebral disc mechanics with degeneration. *J. Bone Jt. Surg. - Ser. A* **88**, 36–40 (2006).

260. Monaco, L. A., Dewitte-Orr, S. J. & Gregory, D. E. A comparison between porcine, ovine, and bovine intervertebral disc anatomy and single lamella annulus fibrosus tensile properties. *J. Morphol.* **277**, 244–251 (2016).
261. Li, Z. *et al.* Development of an ex vivo cavity model to study repair strategies in loaded intervertebral discs. *Eur. Spine J.* **25**, 2898–2908 (2016).
262. Spera, D., Genovese, K. & Voloshin, A. Application of stereo-digital image correlation to full-field 3-D deformation measurement of intervertebral disc. *Strain* **47**, 572–587 (2011).
263. Heuer, F., Schmidt, H. & Wilke, H. J. The relation between intervertebral disc bulging and annular fiber associated strains for simple and complex loading. *J. Biomech.* **41**, 1086–1094 (2008).
264. Mott, P. H. & Roland, C. M. Limits to Poisson's ratio in isotropic materials. *Phys. Rev. B - Condens. Matter Mater. Phys.* **80**, 1–4 (2009).
265. Stokes, I. A. F. Surface strain on human intervertebral discs. *J. Orthop. Res.* **5**, 348–355 (1987).
266. Heuer, F., Schmidt, H. & Wilke, H. J. Stepwise reduction of functional spinal structures increase disc bulge and surface strains. *J. Biomech.* **41**, 1953–1960 (2008).
267. Katz, J. Lumbar disc disorders and low-back pain: socioeconomic factors and consequences. *J. Bone Jt. Surg.* **88**, 21–24 (2006).
268. Carragee, E. J., Don, A. S. & Hurwitz, E. L. Erratum: ISSLS prize winner: Does discography cause accelerated progression of degeneration changes in the lumbar disc: A ten-year matched cohort study (Spine (2009) 34 (2338-2345). *Spine (Phila. Pa. 1976).* **35**, 1414 (2010).
269. Masuda, K. *et al.* A novel rabbit model of mild, reproducible disc degeneration by an anulus needle puncture: Correlation between the degree of disc injury and radiological and histological appearances of disc degeneration. *Spine (Phila. Pa. 1976).* **30**, 5–14 (2005).
270. Alkhatib, B. *et al.* Acute mechanical injury of the human intervertebral disc: link to degeneration and pain. *Eur. Cells Mater.* **28**, 98–111 (2014).
271. Ohtori, S., Inoue, G., Miyagi, M. & Takahashi, K. Pathomechanisms of

discogenic low back pain in humans and animal models. *Spine J.* **15**, 1347–1355 (2015).

272. Willburger, R. E., Ehiosun, U. K., Kuhnen, C., Krämer, J. & Schmid, G. Clinical symptoms in lumbar disc herniations and their correlation to the histological composition of the extruded disc material. *Spine (Phila. Pa. 1976).* **29**, 1655–1661 (2004).
273. Lama, P. *et al.* Significance of cartilage endplate within herniated disc tissue. *Eur. Spine J.* **23**, 1869–1877 (2014).
274. Veres, S. P., Robertson, P. A. & Broom, N. D. The morphology of acute disc herniation: A clinically relevant model defining the role of flexion. *Spine (Phila. Pa. 1976).* **34**, 2288–2296 (2009).
275. Michalek, A. J., Funabashi, K. L. & Iatridis, J. C. Needle puncture injury of the rat intervertebral disc affects torsional and compressive biomechanics differently. *Eur. Spine J.* **19**, 2110–2116 (2010).
276. Zhang, Y. *et al.* Histological Features of the Degenerating Intervertebral Disc in a Goat Disc-Injury Model. *Spine (Phila. Pa. 1976).* **36**, 1519–1527 (2011).
277. Borde, B., Grunert, P., Härtl, R. & Bonassar, L. J. Injectable, high-density collagen gels for annulus fibrosus repair: An in vitro rat tail model. *J. Biomed. Mater. Res. - Part A* **103**, 2571–2581 (2015).
278. Grunert, P. *et al.* Annular repair using high-density collagen gel: A rat-tail in vivo model. *Spine (Phila. Pa. 1976).* **39**, 198–206 (2014).
279. Grunert, P. *et al.* Riboflavin crosslinked high-density collagen gel for the repair of annular defects in intervertebral discs: An in vivo study. *Acta Biomater.* **26**, 215–224 (2015).
280. Pennicooke, B. *et al.* Annulus Fibrosus Repair Using High-Density Collagen Gel. *Spine (Phila. Pa. 1976).* **43**, E208–E215 (2018).
281. Likhitpanichkul, M. *et al.* Fibrin-genipin adhesive hydrogel for annulus fibrosus repair: Performance evaluation with large animal organ culture, in situ biomechanics, and in vivo degradation tests. *Eur. Cells Mater.* **28**, 25–38 (2014).
282. Frauchiger, D. A. *et al.* Genipin-enhanced fibrin hydrogel and novel silk for intervertebral disc repair in a loaded bovine organ culture model. *J. Funct. Biomater.* **9**, (2018).
283. Sloan, S. R. *et al.* Combined nucleus pulposus augmentation and annulus

fibrosus repair prevents acute intervertebral disc degeneration after discectomy. *Sci. Transl. Med.* **12**, 47–49 (2020).

284. Long, R. G. *et al.* Morphological and biomechanical effects of annulus fibrosus injury and repair in an ovine cervical model. *Jor Spine* **3**, 1–13 (2020).

285. Sato, M. *et al.* An experimental study of the regeneration of the intervertebral disc with an allograft of cultured annulus fibrosus cells using a tissue-engineering method. *Spine (Phila. Pa. 1976).* **28**, 548–553 (2003).

286. Hussain, I. *et al.* Mesenchymal Stem Cell-Seeded High-Density Collagen Gel for Annular Repair: 6-Week Results From In Vivo Sheep Models. *Neurosurgery* **85**, E350–E359 (2019).

287. Moriguchi, Y. *et al.* In vivo annular repair using high-density collagen gel seeded with annulus fibrosus cells. *Acta Biomater.* **79**, 230–238 (2018).

288. Nukaga, T., Sakai, D., Schol, J., Sato, M. & Watanabe, M. Annulus fibrosus cell sheets limit disc degeneration in a rat annulus fibrosus injury model. *Jor Spine* **2**, 1–10 (2019).

289. Long, R. G., Torre, O. M., Hom, W. W., Assael, D. J. & Iatridis, J. C. Design Requirements for Annulus Fibrosus Repair: Review of Forces, Displacements, and Material Properties of the Intervertebral Disk and a Summary of Candidate Hydrogels for Repair. *J. Biomech. Eng.* **138**, 021007 (2016).

290. Braghirolli, D. I., Steffens, D. & Pranke, P. Electrospinning for regenerative medicine: A review of the main topics. *Drug Discov. Today* **19**, 743–753 (2014).

291. Cruz, M. A. *et al.* Cell-Seeded Adhesive Biomaterial for Repair of Annulus Fibrosus Defects in Intervertebral Discs. *Tissue Eng. Part A* **24**, 187–198 (2018).

292. Guterl, C. C. *et al.* Characterization of Mechanics and Cytocompatibility of Fibrin-Genipin Annulus Fibrosus Sealant with the Addition of Cell Adhesion Molecules. *Tissue Eng. Part A* **20**, 2536–2545 (2014).

293. Beckstein, J. C., Sen, S., Schaer, T. P., Vresilovic, E. J. & Elliott, D. M. Comparison of animal discs used in disc research to human lumbar disc: Axial compression mechanics and glycosaminoglycan content. *Spine (Phila. Pa. 1976).* **33**, 166–173 (2008).

294. Juenger, S., Gantenbein, B., Alini, M., Ferguson, S. J. & Ito, K. Effect of limited nutrition on intervertebral disc cells under ‘physiological’ loading - A 21 day culture. *Eur. Cells Mater.* **16**, 26 (2008).

295. Illien-Jünger, S. *et al.* The combined effects of limited nutrition and high-frequency loading on intervertebral discs with endplates. *Spine (Phila. Pa. 1976).* **35**, 1744–1752 (2010).

296. Lang, G. *et al.* An intervertebral disc whole organ culture system to investigate proinflammatory and degenerative disc disease condition. *J. Tissue Eng. Regen. Med.* **12**, e2051–e2061 (2018).

297. Farndale, R. W., Buttle, D. J. & Barrett, A. J. Improved quantitation and discrimination of sulphated glycosaminoglycans by use of dimethylmethylene blue. *BBA - Gen. Subj.* **883**, 173–177 (1986).

298. Kang, J. D. *et al.* Herniated lumbar intervertebral discs spontaneously produce matrix metalloproteinases, nitric oxide, interleukin-6, and prostaglandin E2. *Spine (Phila. Pa. 1976).* **21**, 271–7 (1996).

299. Pataky, T. C. One-dimensional statistical parametric mapping in Python. *Comput. Methods Biomech. Biomed. Engin.* **15**, 295–301 (2012).

300. Newell, N. *et al.* Biomechanics of the human intervertebral disc: A review of testing techniques and results. *J. Mech. Behav. Biomed. Mater.* **69**, 420–434 (2017).

301. Casaroli, G. *et al.* A novel finite element model of the ovine lumbar intervertebral disc with anisotropic hyperelastic material properties. *PLoS One* **12**, 1–18 (2017).

302. Barthelemy, V. M. P. *et al.* A computational spinal motion segment model incorporating a matrix composition-based model of the intervertebral disc. *J. Mech. Behav. Biomed. Mater.* **54**, 194–204 (2016).

303. Fessel, G., Cadby, J., Wunderli, S., Van Weeren, R. & Snedeker, J. G. Dose- and time-dependent effects of genipin crosslinking on cell viability and tissue mechanics - Toward clinical application for tendon repair. *Acta Biomater.* **10**, 1897–1906 (2014).

304. Kolstad, F., Myhr, G., Kvistad, K. A., Nygaard, Ø. P. & Leivseth, G. Degeneration and height of cervical discs classified from MRI compared with precise height measurements from radiographs. *Eur. J. Radiol.* **55**, 415–420 (2005).

305. Wang, C., Lau, T. T., Loh, W. L., Su, K. & Wang, D. A. Cytocompatibility study of a natural biomaterial crosslinker-Genipin with therapeutic model cells. *J. Biomed. Mater. Res. - Part B Appl. Biomater.* **97 B**, 58–65 (2011).

306. G., Rose, L. *et al.* Morphological and biomechanical effects of annulus fibrosus injury and repair in an ovine cervical model. *JOR Spine* (2019) doi:10.1002/jsp2.1074.

307. Tirella, A., Liberto, T. & Ahluwalia, A. Riboflavin and collagen: New crosslinking methods to tailor the stiffness of hydrogels. *Mater. Lett.* **74**, 58–61 (2012).

308. Mobley, S. R., Hilinski, J. & Toriumi, D. M. Surgical tissue adhesives. *Facial Plast. Surg. Clin.* **10**, 147–154 (2002).

309. Wade, K. R., Schollum, M. L., Robertson, P. A., Thambyah, A. & Broom, N. D. A more realistic disc herniation model incorporating compression, flexion and facet-constrained shear: a mechanical and microstructural analysis. Part I: Low rate loading. *Eur. Spine J.* **26**, 2616–2628 (2017).

310. Shan, Z. *et al.* A more realistic disc herniation model incorporating compression, flexion and facet-constrained shear: a mechanical and microstructural analysis. Part II: high rate or ‘surprise’ loading. *Eur. Spine J.* **26**, 2629–2641 (2017).

311. Vos, T. *et al.* Global, regional, and national incidence, prevalence, and years lived with disability for 310 diseases and injuries, 1990–2015: a systematic analysis for the Global Burden of Disease Study 2015. *Lancet* **388**, 1545–1602 (2016).

312. Hartvigsen, J. *et al.* What low back pain is and why we need to pay attention. *Lancet* **391**, 2356–2367 (2018).

313. Hancock, M. J. *et al.* Systematic review of tests to identify the disc, SIJ or facet joint as the source of low back pain. *Eur. Spine J.* **16**, 1539–1550 (2007).

314. Brinjikji, W. *et al.* MRI findings of disc degeneration are more prevalent in adults with low back pain than in asymptomatic controls: A systematic review and meta-analysis. *Am. J. Neuroradiol.* **36**, 2394–2399 (2015).

315. Li, L. & LaBarbera, D. V. 3D high-content screening of organoids for drug discovery. *Compr. Med. Chem. III* **2**–**8**, 388–415 (2017).

316. https://www.femtotools.com/. https://www.femtotools.com/.

317. Gunatillake, P. A., Adhikari, R. & Gadegaard, N. Biodegradable synthetic polymers for tissue engineering. *Eur. Cells Mater.* **5**, 1–16 (2003).

318. Pereira, P. A. Peptide and protein application in tissue repair and regeneration. *Pept. Protein Deliv.* 291–311 (2011) doi:10.1016/B978-0-12-384935-9.10012-4.

319. Jackson, M. R. *Topical hemostatic agents for localized bleeding*. *Consultative*

Hemostasis and Thrombosis (Elsevier Inc., 2007). doi:10.1016/B978-141602401-9.10029-X.

320. Bowles, R. D., Williams, R. M., Zipfel, W. R. & Bonassar, L. J. Self-Assembly of Aligned Tissue-Engineered Annulus Fibrosus and Intervertebral Disc Composite Via Collagen Gel Contraction. *Tissue Eng. Part A* **16**, 1339–1348 (2010).
321. Bowles, R. D. & Setton, L. A. Biomaterials for intervertebral disc regeneration and repair. *Biomaterials* **129**, 54–67 (2017).
322. Shea, M., Takeuchi, T. Y., Wittenberg, R. H., White, A. A. I. I. I. & Hayes, W. C. A Comparison of the Effects of Automated Percutaneous Diskectomy and Conventional Diskectomy on Intradiscal Pressure, Disk Geometry, and Stiffness. *Clin. Spine Surg.* **7**, (1994).
323. Montgomery, M. *et al.* Flexible shape-memory scaffold for minimally invasive delivery of functional tissues. *Nat. Mater.* **16**, 1038–1046 (2017).
324. Norris, J. P., Breslin, D. S. & Staskin, D. R. Use of synthetic material in sling surgery: A minimally invasive approach. *J. Endourol.* **10**, 227–230 (1996).